

Self-organized Ion Beam Pattern Formation on Si(001)

Inaugural-Dissertation
zur Erlangung des Doktorgrades
der Mathematisch-Naturwissenschaftlichen Fakultät
der Universität zu Köln

vorgelegt von
Martin Engler
aus Bergisch Gladbach

Köln 2015

Berichterstatter: Prof. Dr. Thomas Michely
Prof. Dr. Stephan Schlemmer

Tag der mündlichen Prüfung: 14. 10. 2014

Kurzzusammenfassung

Mit in-situ Rastertunnelmikroskopie, niederenergetischer Elektronenbeugung, sowie ex-situ Rasterkraftmikroskopie, Rasterelektronenmikroskopie, Transmissionselektronenmikroskopie und Rutherford-Rückstreu-Spektrometrie wurde die selbstorganisierte Ionenstrahl-Musterbildung von Si(001) durch Beschuss mit 2 keV Kr^+ Ionen untersucht.

Bekannterweise können Metallverunreinigungen die Musterbildung verursachen. Dazu wurde untersucht, wie die Ko-Deposition von Pd, Ir, Fe, Ag und Pb die Ionenstrahl-Musterbildung beeinflussen. Bei den hier untersuchten Bedingungen ist es nötig, dass die Metalle Silizide bilden können, um Musterbildung zu verursachen. Dies allein reicht jedoch nicht aus. Die Stoßkinetik ist nicht entscheidend dafür, ob ein Metall Musterbildung verursacht, wie sich durch den Vergleich von Metallen mit ähnlicher Atommasse und Kernladungszahl zeigt. Um die Beobachtungen zu erklären, muss man berücksichtigen, dass die Oberflächenmorphologie und deren chemische Zusammensetzung eng miteinander verknüpft sind und sich gegenseitig beeinflussen. Durch diese gegenseitige Beeinflussung hängt die mittlere Metallkonzentration empfindlich von der Geschichte der Musterbildung ab und ist daher kein geeignetes Maß, um das entstehende Muster zu charakterisieren.

Bei Beschuss mit 2 keV Kr^+ Ionen unter Einfallswinkeln im Bereich zwischen 58° und 79° bilden sich bei Raumtemperatur auch ohne Verunreinigungen Muster. Die Entwicklung der Muster wurde mit in-situ Rastertunnelmikroskopie bei den Einfallswinkeln 63° und 75° untersucht. Dabei wurde jeweils die Ionenfluenz um den Faktor 1000 verändert. Für beide Winkel lassen sich zwei Fluenzbereiche unterscheiden. Während sich für niedrige Fluenzen bei beiden Einfallswinkel ähnliche Wellenmuster mit einem Wellenvektor senkrecht zum auf die Oberfläche projizierten Ionenstrahl bilden, ist bei hohen Fluenzen die Entwicklung und die entstehende Morphologie qualitativ unterschiedlich. Für 63° bilden sich Wellen senkrecht zu den ursprünglichen Wellen, während sich für 75° eine Dachschild-artige Oberflächenmorphologie ausbildet. Der Vergleich der Ergebnisse mit experimentellen Daten über Ionenstrahl-Musterbildung auf Si- und Ge-Oberflächen aus der Literatur erlaubt es universelle Phänomene zu identifizieren. Die Anwendbarkeit bestehender theoretischer Modelle auf die Musterbildung bei den hier untersuchten Bedingungen wird bewertet.

Unterhalb einer kritischen Temperatur amorphisiert Si(001) bei Ionenbeschuss, während es oberhalb dieser Temperatur kristallin bleibt. Für 2 keV Kr^+ liegt die Temperatur bei (674 ± 10) K. In einem engen Temperaturbereich über dieser Temperatur bis 720 K entwickelt sich eine Morphologie aus Gruben und Hügeln, deren Stufenkanten parallel zu

den $\langle 110 \rangle$ Richtungen sind. Durch die Ehrlich-Schwoebel-Barriere an den Stufenkanten wird während des Ionenbeschusses ein destabilisierender Diffusionsstrom induziert. Bei $\approx 0\text{ K}$ ist die Aufrauung durch diesen Strom am stärksten. Deshalb wurde bei dieser Temperatur die Fluenzabhängigkeit der Oberflächenmorphologie untersucht. Bei hohen Fluenzen ändert sich die Morphologie und es bilden sich Täler und Bergrücken, die $\approx 45^\circ$ gegen die $\langle 110 \rangle$ Richtungen verdreht sind.

Abstract

Self-organized ion beam pattern formation of Si(001) by 2 keV Kr⁺ ion bombardment was investigated in-situ with scanning tunnelling microscopy, and low energy electron diffraction and ex-situ with atomic force microscopy, scanning electron microscopy, transmission electron microscopy, and Rutherford backscattering spectrometry.

It is known that metal impurities can induce pattern formation. The effect of co-depositing Pd, Ir, Fe, Ag, and Pb on ion beam pattern formation was analyzed. For the condition analyzed here, the ability of the metal to form a silicide is necessary for inducing pattern formation. However this is not sufficient. Comparing the effects of metals with similar nuclear charge and mass, but with different ability to form silicides, shows that collision kinetics are not decisive for pattern formation. To understand the observed phenomena one has to consider that the morphology and the composition of the surface are bidirectionally coupled. Due to this coupling the metal concentration depends on the surface history and it does not determine the resulting morphology.

For ion incidence angles from 58° to 79° patterns develop on Si during 2 keV Kr⁺ ion bombardment at room temperature even without co-deposition of impurities. The evolution of the surface morphology was studied using in-situ scanning tunnelling microscopy for the ion incidence angles 63° and 75°. The fluence was varied by a factor of 1000. Two fluence regimes can be distinguished. While a similar ripple pattern evolves in the low fluence regime for both incidence angles, the evolution differs for both incidence angles in the high fluence regime. In the high fluence regime perpendicular mode ripples and a roof-tile morphology develop for 63° and 75° respectively. The observations will be compared to experimental data of ion beam patterning of Si and Ge from literature to identify universal phenomena. Comparing the results with theoretical models allows to assess their applicability to ion beam pattern formation of Si.

Si(001) amorphizes under ion bombardment below a critical temperature and is crystalline above the critical temperature. For 2 keV Kr⁺ ions the critical temperature is (674 ± 10) K. In a limited temperature range of 674 K to 720 K the surface develops a pit and mound morphology with the step edges parallel to the $\langle 110 \rangle$ directions. The pattern formation is driven by the Ehrlich-Schwoebel barrier inducing an effective uphill diffusion current. The surface roughness is maximum at $T \approx 700$ K. At this temperature the fluence dependence of the surface morphology was studied. For high fluences the pattern changes into a ridge and valley morphology where the directions of the ridges and valley is $\approx 45^\circ$ rotated to the $\langle 110 \rangle$ directions.

Contents

Kurzzusammenfassung	iii
Abstract	v
List of Figures	ix
List of Tables	xiii
1. Introduction	1
2. Scientific background	3
2.1. Ion bombardment of solids	3
2.2. Spinodal decomposition	6
2.3. Ion beam pattern formation of amorphous elemental semiconductors	7
2.4. Pattern formation on crystalline surfaces	14
2.5. Metal induced pattern formation	16
2.6. Si(001)	18
3. Methods	21
3.1. UHV system <i>Athene</i>	21
3.2. Calibration of the movable thermocouple	21
3.3. Sample preparation	22
3.4. Methods of sample analysis	25
3.5. Image analysis	29
3.6. Kinetic Monte Carlo simulations with TRIM.SP	33
4. Silicide induced patterns	35
4.1. Ag co-deposition	35
4.2. Pd co-deposition	39
4.3. Pb co-deposition	44
4.4. Ir co-deposition	46
4.5. Fe co-deposition	48
4.6. Discussion	52

5. Pattern formation without impurities	63
5.1. Angle dependence near the transition from a flat surface to ripples	63
5.2. Pattern evolution at 63° incidence angle	64
5.3. Pattern evolution at 75° incidence angle	68
5.4. Discussion	71
6. Pattern formation on crystalline Si(001)	81
6.1. Temperature dependence	81
6.2. Fluence dependence	86
6.3. Discussion	89
7. Summary	93
8. Outlook	95
A. Numerical modelling of sputter co-deposition fluxes	97
Bibliography	99
Acknowledgements	113
Publications	115
Erklärung	117
Curriculum Vitae	119

List of Figures

2.1. Collision of an ion with a stationary target atom.	3
2.2. (a)Fe-Si phase diagram, (b) sketch of plausible free energy curve	6
2.3. STM topographs at (a) $\vartheta = 55^\circ$, (b) $\vartheta = 63^\circ$, (c) $\vartheta = 75^\circ$, (d) $\vartheta = 81^\circ$	8
2.4. Dependence of surface roughness on incidence angle.	8
2.5. Sputtering yield of Si as function of the local incidence angle	9
2.6. Definition of slope angle α , (global) incidence angle ϑ , and local incidence angle θ	9
2.7. Sketch to illustrate coarsening by reflected ions.	13
2.8. Sketch of angles relevant for the discussion of the Hauffe mechanism (see text).	13
2.9. Si(001) surface.	19
3.1. Calibration of the movable thermocouple.	22
3.2. (a) Sputter co-deposition setup, (b) co-evaporation setup.	23
3.3. Sketch of force-distance curve for AFM	27
3.4. Sketch of an AFM setup	27
3.5. Rutherford backscattering spectrometry (RBS) geometry	28
3.6. Determination of slope distributions	31
3.7. separation into long and short wavelength components	32
3.8. Sobel filter	33
4.1. Ag sputter co-deposition: in-situ STM, ex-situ AFM, ex-situ SEM images	36
4.2. Ag sputter co-deposition: protrusion density	37
4.3. Ag sputter co-deposition: roughness	37
4.4. Ag sputter co-deposition: SE and ESB SEM images	38
4.5. Sketch of the Ag cluster formation	38
4.6. Pd sputter co-deposition: STM images	40
4.7. Pd sputter co-deposition: roughness, wavelength, Pd surface density	41
4.8. Pd co-evaporation: STM images	42
4.9. Slope angle distribution after Pd co-evaporation with $\Phi_{\text{Pd}}/\Phi_{\text{Kr}} = 0.8$	43
4.10. Pd co-evaporation: cross-sectional TEM	45
4.11. In-situ STM topographs after Pb sputter co-deposition	46
4.12. Ex-situ SEM image of Pd sputter co-deposition sample	46
4.13. In-situ STM topographs after Ir sputter co-deposition	47

4.14. Ex-situ AFM images of the Ir sputter co-deposition sample	47
4.15. Roughness σ and wavelength λ for Ir sputter co-deposition.	48
4.16. Roughness σ , wavelength λ , Fe concentration c_{Fe} , and Fe area density n_{Fe} of Fe sputter co-deposition experiment	49
4.17. STM topographs and autocorrelation for Fe co-evaporation experiments	50
4.18. Dependence of pattern formation on angle α between ion beam and Fe flux.	51
4.19. Metals inducing pattern formation	52
4.20. Sketch of the assumed evolution of n_{Fe} during co-evaporation	56
5.1. Transition from flat surface to ripple patterns	63
5.2. Dependence of (a) roughness σ , (b) wavelength λ , and (c) disorder $\delta\lambda/\lambda$ on incidence angle ϑ near transition from flat to ripple surface.	64
5.3. Evolution of topography at $\vartheta = 63^\circ$	65
5.4. Slope distribution at $\vartheta = 63^\circ$	65
5.5. Evolution of the roughness σ , the short wavelength roughness component σ_s , and the long wavelength roughness component σ_l as a function of ion fluence F for $\vartheta = 63^\circ$	66
5.6. Evolution of (a) roughness σ , (b) wavelength λ , (c) pattern order $\delta\lambda/\lambda$, and (d) local ion incidence angles	67
5.7. Evolution of topography at $\vartheta = 75^\circ$	69
5.8. Slope distribution $\vartheta = 75^\circ$	69
5.9. SEM image after 2 keV Kr^+ bombardment at $\vartheta = 75^\circ$ with $F = 3.0 \times 10^{22}$ ions/ m^2	70
5.10. Local incidence angle on downwind face θ_d and upwind face θ_u as function of global incidence angle ϑ	75
5.11. Roughness σ as a function of ion fluence F for ion exposure of Si(001) under various ion beam conditions.	76
5.12. Evolution of (a) roughness σ and (b) wavelength λ of ion beam induced patterns on Si and Ge (Teichmann et al. [131]) as function of fluence. . .	78
6.1. Overview of temperature dependence with old thermocouple	82
6.2. Overview of temperature dependence with new thermocouple	83
6.3. Dependence of (a) roughness and (b) structure width on sample temper- ature	84
6.4. Distribution of slope angles of series with old thermocouple (figure 6.1) .	85
6.5. Distribution of slope angles of series with new thermocouple (figure 6.2)	85
6.6. LEED patterns after annealing of ion beam amorphized Si(001)	85
6.7. Fluence dependence at $T = (704 \pm 10)$ K	87
6.8. Dependence of (a) roughness σ and (b) structure width λ on fluence at $T = (704 \pm 10)$ K.	88
6.9. Distribution of slope angles as function of the fluence at $T = (704 \pm 10)$ K.	88

List of Figures

6.10. Sketch of the pattern rotation for the case of two touching pyramids . . .	90
A.1. Sketch of sputter co-deposition	97
A.2. Differential Pd sputtering yield $dY_{Pd}/d\Omega$ and ion reflectivity $dY_R/d\Omega$. .	98
A.3. Relative Pd flux $\Phi_{Pd}/\Phi_{\text{primary Kr}}$ (a) and secondary Kr^+ flux $\Phi_{\text{reflected Kr}}/\Phi_{\text{primary Kr}}$ (b) as function of the distance to the target x	98

List of Tables

4.1. Densities n , total sputtering yields Y , partial Si sputtering yields Y_{Si} , partial metal ($M = \text{Pd, Fe, Ir, C}$) sputtering yields Y_M , total erosion rates $\rho = Y/n$, partial Si erosion rates $\rho_{\text{Si}} = Y_{\text{Si}}/n$ calculated with TRIM.SP.	53
5.1. Regimes of morphological evolution at $\vartheta = 63^\circ$	72
5.2. Regimes of morphological evolution at $\vartheta = 75^\circ$	72

1. Introduction

Self-organized ion beam pattern formation is a simple method for producing regular patterns with nano- to micrometer periodicity. The ease of pattern production enables many possible applications, e. g. anti-reflective coatings [47, 49], or nano-scale patterned magnetic films [78, 145, 146]. Navez, Sella, and Chaperot [100] reported already in 1962 the formation of ripples on glass after bombarding it with ionized air at 4 keV energy. Self-organized ion beam pattern formation has been reported in the following for many different systems: 1. metal surfaces [58, 59, 67, 92, 94, 129], 2. glass surfaces [2, 47, 69, 100, 137], 3. compound semiconductors [36, 46, 51], and 4. elemental semiconductors which amorphize under ion bombardment at room temperature [3, 20, 21, 68, 77, 86, 131, 144]. Depending on the system and ion bombardment conditions used many different surface morphologies can be achieved like ordered ripple or dot patterns, faceted roof-tile morphologies, pit and mound morphologies, cones, pillars, wall structures, sponge like structures.

Initially ion beam pattern formation was modeled taking into account the dependence of erosion on the local incidence angle [19, 102]. Bradley and Harper [14] derived the dependence of erosion on the local curvature from the Sigmund model of sputtering [126]. They combined the curvature dependence of erosion with relaxation by surface diffusion to explain the development of regular ripple patterns. Later attention was drawn to material transport at the surface as source of an instability leading to pattern formation [20, 22, 105, 106]. In systems with more than one atomic species also the evolution of the surface composition and chemical effect have to be considered [9, 10, 13, 15, 104, 123, 124]. These continuum models are suited to describe evolution of amorphous or amorphized substrates as these surfaces are locally isotropic. On crystalline substrates additional effects arise due to the anisotropic nature of crystalline surface. Surface diffusion depends on the direction with respect to the crystallographic directions [4]. Step edges introduce an additional barrier for diffusion of adatoms and vacancies [28, 43, 122], leading to an effective uphill diffusion bias [75, 125, 136].

Silicon is an ideal substrate material for studying ion beam pattern formation. It can be produced in high purity and with extremely low surface roughness. As Si amorphizes quickly under ion bombardment at room temperature, continuum modeling can be applied to the pattern evolution. Recently, it was found that early experiments yielding pattern formation for near normal incidence angles were influenced by metal impurities unintentionally deposited during ion bombardment [81, 108]. Clean experiments, which avoid the deposition of impurities, showed that for large range of incidence angles from

normal incidence to 50° – 60° to the surface normal the surface remains flat, depending on ion energy and species [81, 84, 85]. For larger incidence angles three angular ranges with qualitatively different surface morphologies have been identified: 1. a range with ripples with the wave vector parallel to the ion beam direction 2. a range with roof tile morphology at larger incidence angles, and 3. at grazing incidence grooves in direction of the ion beam [81]. This initiated further experimental [62–64, 80, 82, 109, 147] and theoretical [9, 10, 12, 13, 104, 124] effort to understand the mechanisms of pattern formation with concurrent deposition of metal impurities, as this is a promising procedure to produce well ordered patterns. The type of pattern produced with metal co-deposition can be tuned by the metal and the metal flux used [62, 80, 81]. To explain the metal induced pattern formation two different approaches have been proposed: chemically driven phase separation [62, 104], and a geometrical instability [9, 80].

Although ion beam pattern formation is known for more than five decades, the mechanisms of ion beam pattern formation are still not fully understood. This thesis contributes to the effort to better understand ion beam pattern formation. Three aspects of ion beam pattern formation on Si(001) will be addressed in this thesis.

In chapter 4 ion beam pattern formation with metal co-deposition will be discussed. The question, how important silicide formation is for pattern formation, is investigated by comparing co-deposition of the silicide forming metals Pd and Ir with co-deposition of the non-silicide forming metals Ag and Pb. The dependence of pattern formation on the metal to ion flux ratio gives further insight into the mechanisms of pattern formation with metal co-deposition.

In chapter 5 the evolution of the pattern morphology during 2 keV Kr^+ without metal co-deposition will be analyzed. The pattern evolution was studied in the ripple pattern range and the roof tile pattern range at the two incidence angles 63° and 75° respectively.

In chapter 6 the temperature dependence of the surface morphology will be analyzed. At temperatures above 670 K the surface remains crystalline during 2 keV Kr^+ ion bombardment and a pit and mound structure emerges. The evolution of the surface at 700 K will be analyzed.

2. Scientific background

2.1. Ion bombardment of solids

Ions impinging on a solid surface with a few keV kinetic energy lose their energy in a series of collisions with the target atoms. In the following the physics behind this will be reviewed briefly.

Elastic collisions

When an ion hits a solid surface it collides with the target atoms. Due to the short interaction time and the screening of the Coulomb interaction for ions with energies > 1 keV this can be described in a good approximation as a binary collision between the resting target atom and the moving ion [99]. The energy transferred $T = E - E'$ from the ion to a target atom in an elastic binary collision is a function of the scattering angle θ of the ion (see figure 2.1). In the laboratory system the energy transfer for non-relativistic velocities, i. e. for kinetic ion energies < 10 MeV, is given by

$$T = (1 - K)E \quad (2.1)$$

$$K = \frac{M_{\text{ion}}^2}{(M_{\text{ion}} + M_{\text{target}})^2} \left[\cos \theta \pm \left(\frac{M_{\text{target}}^2}{M_{\text{ion}}^2} - \sin^2 \theta \right)^{1/2} \right]^2. \quad (2.2)$$

For $M_{\text{ion}} < M_{\text{target}}$ energy and momentum conservation allow only the plus sign. For $M_{\text{ion}} > M_{\text{target}}$ both signs are allowed and $\theta_{\text{max}} = \arcsin(M_{\text{target}}/M_{\text{ion}})$ is the maximum

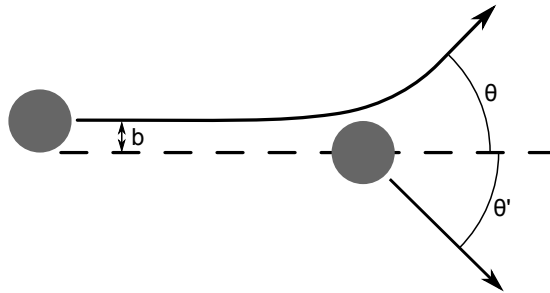


Figure 2.1.: Collision of an ion with a stationary target atom.

possible scattering angle [76, 91]. The target atom is scattered under the angle

$$\theta' = -\arctan\left(\frac{\sqrt{K} \sin \theta}{\sqrt{1 - K(1 + \sin^2 \theta)}}\right). \quad (2.3)$$

Further details, like the scattering cross-section and the dependence of the scattering angle on the impact parameter b , can only be obtained with knowledge of the interaction potential. The screening of the nuclear potential by the electrons has to be considered. Usually a screened Coulomb potential

$$V(r) = \frac{1}{4\pi\epsilon_0} \frac{Z_{\text{ion}}Z_{\text{target}}e^2}{r} \Phi\left(\frac{r}{a}\right) \quad (2.4)$$

is assumed with a screening function $\Phi(r/a)$ and the screening length a [54].

Ion stopping

Energetic ions or atoms hitting a target will interact with the target in different ways depending on their energy and charge state. Highly charged ions, where the potential energy released during neutralization is significant and can lead to surface modifications, will not be discussed here. Ions are decelerated in the target by (a) elastic collisions with target atoms as discussed above (nuclear stopping), (b) exciting the electronic system of the target (electronic stopping), and (c) nuclear reactions. The activation barriers of nuclear reaction are in the order of several MeV. Thus nuclear reactions are not relevant for the energy used usually in ion bombardment experiments. The deceleration can be described by the energy loss per path length x or stopping power

$$\frac{dE}{dx} = \left.\frac{dE}{dx}\right|_{\text{n}} + \left.\frac{dE}{dx}\right|_{\text{e}} \quad (2.5)$$

which is the sum of the nuclear (n) and electronic stopping (e). For small energies of a few keV considered in this work nuclear stopping is the dominant stopping mechanism and electronic stopping can be neglected [54].

Collision cascade and defect generation

For ions with a kinetic energy of a few keV, nuclear stopping is associated with producing a collision cascade near the surface. During a collision with a target atom the ion transfers a part of its kinetic energy to the target atom (see eq. (2.2)). If the transferred energy is larger than the displacement threshold energy E_{D} the atom will be scattered away from its original site. This atom is called a *primary knock-on atom*. If the transferred energy is lower the atom stays at its original site and the energy will be dissipated by exciting lattice vibrations. After the collision the ion usually has enough energy

2.1. Ion bombardment of solids

to displace further atoms. When the ion has lost its kinetic energy, it is implanted into the target. If the primary knock-on atoms have enough energy they displace other atoms in secondary collisions. These secondary knock-on atoms can further displace atoms until their energy is dissipated. This sequence of collisions is called a *collision cascade*. Surface atoms receiving enough momentum in secondary collisions to overcome the surface binding energy are sputtered away from the surface. Otherwise they may form mobile ad-atoms which will soon be reincorporated into the surface. The average number of atoms sputtered away per incident ion is the *sputtering yield* Y [99]. The sputtering of surface atoms leads to the production of surface vacancies on crystalline surfaces.

For projectiles with low energies of the order of 1 keV, the mean free path between two collisions is of the order of the interatomic distances. Then, the collision cascade becomes dense and after approximately 1 ps the energy distribution of the atoms can be described with the Maxwell-Boltzmann distribution [99]. The temperature reached in this *thermal spikes* is high enough to locally melt the target material. These thermal spikes are quenched in a few ps to the bulk temperature [103].

In metals the molten pockets recrystallize and only vacancies and interstitial atoms remain. In contrast in semiconductors, like Si and Ge, the molten pockets do not recrystallize during the quenching of the thermal spike and amorphous pockets remain [103]. During ion bombardment the amorphous pockets from the impacts coalesce into an amorphous layer. Already fluences as low as $F \approx 3 \times 10^{18}$ ions/m², which corresponds to ≈ 0.4 monolayer equivalents,¹ amorphize Si(001) under 2 keV Kr⁺ bombardment [79]. At elevated sample temperature even semiconductors remain crystalline during ion bombardment [82, 107].

Ion beam mixing

On multi component targets the stochastic nature of the collision cascade leads to mixing of the components. If ions hit a surface composed of two target species A and B , the collision cascade will displace both species randomly with a probability $\rho_i(\mathbf{u})$ by displacement vector \mathbf{u} . If the composition is inhomogeneous this leads to a mixing of both species. This mixing can be approximated by a sum of ballistic drift and diffusion [30]

$$\partial_t c|_{\text{ballistic}} = -\mathbf{v}_{\text{drift},i} \cdot \nabla c + D_{\text{mix},i} \nabla^2 c. \quad (2.6)$$

The drift velocity is given by

$$\mathbf{v}_{\text{drift},i} = \Phi_{\text{ion}} N_{d,i} \int \mathbf{u} \rho_i(\mathbf{u}) d^3 u. \quad (2.7)$$

¹fluence divided by area density of atoms in one layer

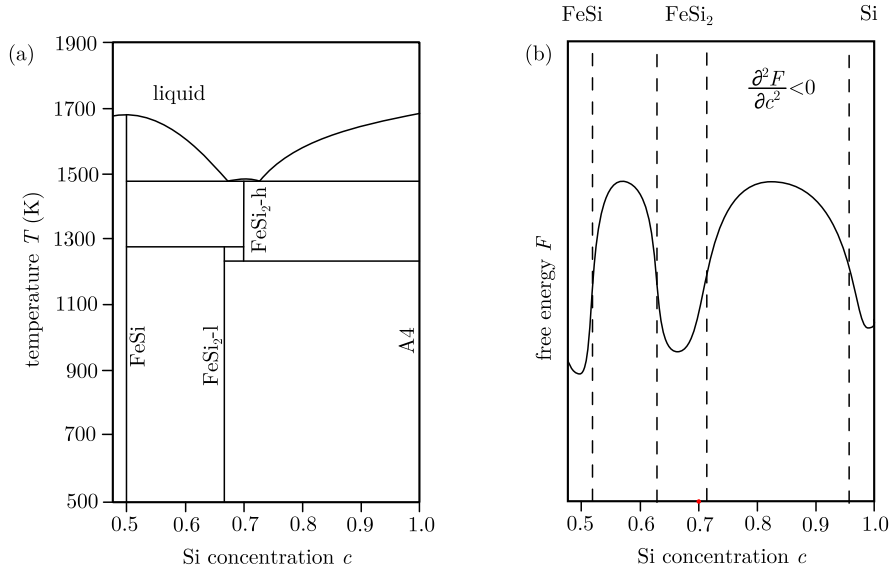


Figure 2.2.: (a) Si rich part of Fe-Si phase diagram from ref. [114]. (b) Sketch of a plausible free energy curve for a homogeneous composition.

Usually the drift velocity is in direction of the ion beam. The diffusive part is described by the effective diffusivity of ion beam mixing

$$D_{\text{mix},i} = \frac{\Phi_{\text{ion}} N_{\text{d},i}}{2} \int |\mathbf{u}|^2 \rho_i(\mathbf{u}) d^3u. \quad (2.8)$$

The strength of ion beam mixing is proportional to the ion flux Φ_{ion} and the number $N_{\text{d},i}$ of displaced atoms of species i [104].

2.2. Spinodal decomposition

Two-component systems often have thermodynamic stable phases with defined composition in their phase diagrams. If the composition deviates from these stable phases the free energy is increased. As an example, the phase diagram of Fe and Si in the Si rich region is shown in figure 2.2(a) and a sketch of a plausible free energy curve is shown in figure 2.2(b). The free energy F of a homogeneous system with concentration c_0 can be reduced by decomposing into regions with the stable concentrations. For a non homogeneous system the concentration gradient costs free energy. According to Cahn and Hilliard [17], the free energy of the system can be obtained by integrating the free energy density $f(c)$ of a homogeneous compound and the term $\kappa(\nabla c)^2$ giving the free energy

2.3. Ion beam pattern formation of amorphous elemental semiconductors

cost of the concentration gradient

$$F = \int_V f(c) + \kappa(\nabla c)^2 dV. \quad (2.9)$$

Cahn [16] showed that the diffusion current for small concentration gradients is given by

$$\mathbf{j} = -M\nabla \left(\frac{\partial f}{\partial c} - 2\kappa\nabla^2 c \right) \quad (2.10)$$

where M is the mobility. Inserting this current into the continuity equation yields the Cahn-Hilliard equation

$$\frac{\partial c}{\partial t} = -\nabla \cdot \mathbf{j} = M \frac{\partial^2 f}{\partial c^2} \nabla^2 c - 2M\kappa\nabla^4 c \quad (2.11)$$

The free energy density $f(c)$ of a homogeneous system is proportional to the free energy of $F(c)$ of a homogeneous system. Near the stable compositions the curvature $\partial_c^2 F$ of the free energy as function of the concentration is positive and phase separation happens by nucleation and growth of the nucleated clusters due to Fickian diffusion. For larger deviations from the stable compositions $\partial_c^2 F$ is negative. Then the diffusion current is in direction of the concentration gradient. This up-hill diffusion leads to spontaneous decomposition of the system as it is unstable against infinitesimal perturbations of the composition. This phase separation is called spinodal decomposition. Spinodal decomposition produces composition modulations with the wavelength

$$\lambda = 2\pi \sqrt{-\frac{2\kappa}{\partial^2 F / \partial c^2}}. \quad (2.12)$$

2.3. Ion beam pattern formation of amorphous elemental semiconductors

Elemental semiconductor surfaces amorphize under ion beam irradiation at room temperature [79, 103]. This makes them ideal test cases for continuum models of ion beam pattern formation as the properties of the surface are isotropic and effects like step edge barriers [43, 122] can be ignored.

For a given ion species, energy, and substrate combination a sequence of patterns can be observed with increasing incidence angle² ϑ . Figure 2.4 shows the dependence of the surface roughness σ as a function of the incidence angle ϑ for 2 keV Kr⁺ on Si(001). For incidence angles ϑ from normal incidence up to a critical angle ϑ_c the surface remains *flat* [81, 84, 131]. Light ions do not induce pattern formation [131]. The patterns reported

²The incidence angle ϑ is the angle between ion beam and global sample normal

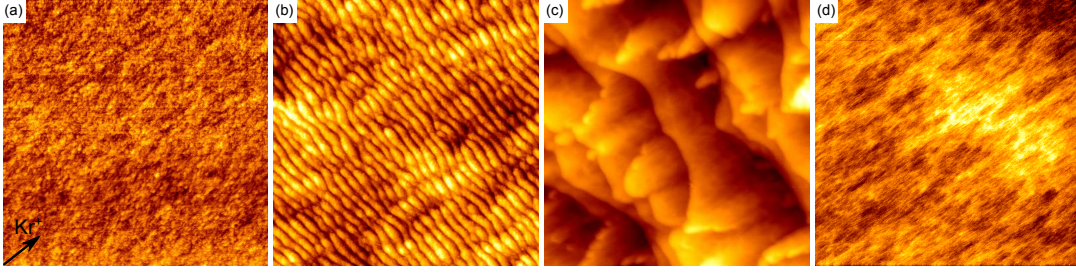


Figure 2.3.: $1\ \mu\text{m} \times 1\ \mu\text{m}$ STM topographs at (a) $\vartheta = 55^\circ$ (z-scale 2 nm), (b) $\vartheta = 63^\circ$ (z-scale 5 nm), (c) $\vartheta = 75^\circ$ (z-scale 45 nm), and (d) $\vartheta = 81^\circ$ (z-scale 2.5 nm). (a) and (d) are from ref. [79].

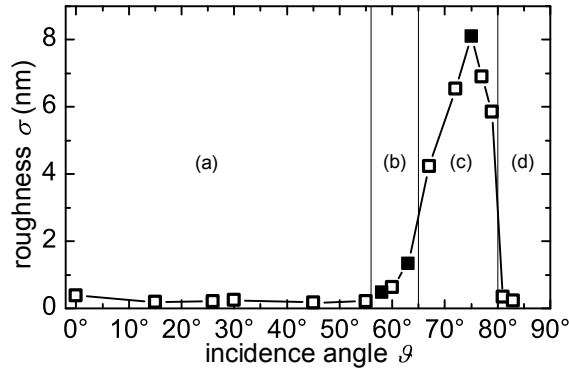


Figure 2.4.: Dependence of surface roughness on incidence angle for 2 keV Kr^+ on $\text{Si}(001)$ with a fluence $F = 1 \times 10^{22}$ ions/ m^2 . The vertical lines indicate the borders of the angular ranges. ■: new data (see chapter 5), □: data from reference [79]

earlier for normal or near normal incidence low energy ion bombardment [85, 86, 151, 152] have been shown to be caused by simultaneous impurity co-deposition [31, 32, 81, 108, 109] or ions scattered at the sample holder [84]. For incidence angles larger than the critical angle ϑ_c a *ripple pattern* with a wave vector \mathbf{k} parallel to the projection of the ion beam (projected ion beam) on the sample plane evolves. The critical angle is in the range from 50° to 65° depending on the ion–target combination for low energy ion bombardment [21, 79, 81, 84, 131]. With further increasing ϑ there is an angular range where the surface transforms into a *roof-tile* structure for sufficiently high fluences [79, 81, 131, 144]. For *grazing incidence* angles $\vartheta > 80^\circ$ the surface develops grooves in the direction of the ion beam, i. e. the wave vector is perpendicular to the projected ion beam [81, 84, 131]. In this range the surface roughness is of the same magnitude as the initial roughness [81, 131]. For 2 keV Kr^+ ion bombardment with the fluence $F = 1 \times 10^{21}$ ions/ m^2 the angular ranges are (a) *flat surfaces* for $\vartheta \leq 55^\circ$, (b) *ripple patterns* for $58^\circ \leq \vartheta \leq 63^\circ$, (c) *roof-tile patterns* for $67^\circ \leq \vartheta \leq 79^\circ$, and (d) at *grazing incidence* $\vartheta \geq 81^\circ$ a flat surface with faint grooves in ion beam direction (compare ref. [79] figure 4.2 and [81] figure 1). Characteristic morphologies after the ion fluence $F = 1 \times 10^{22}$ ions/ m^2 are shown in figure 2.3 Figure 2.4 shows the dependence of the

2.3. Ion beam pattern formation of amorphous elemental semiconductors

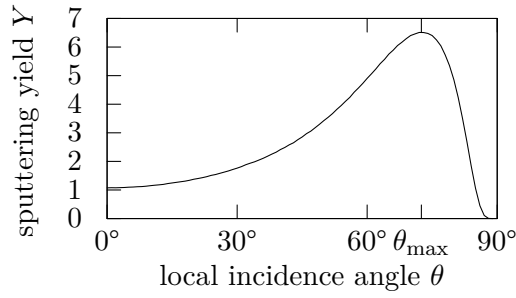


Figure 2.5.: Sputtering yield of Si bombarded with 2 keV Kr⁺ ions as function of the local incidence angle θ calculated with TRIM.SP.

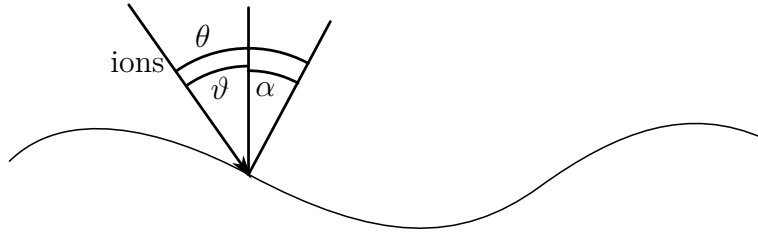


Figure 2.6.: Definition of slope angle α , (global) incidence angle ϑ , and local incidence angle θ .

surface roughness σ on the ion incidence angle ϑ .

The fluence dependence of low energy ion beam patterning has been investigated for different ion species, energies, and incidence angles on Si [3, 21, 71, 86, 144] and Ge [131].

In the following, theoretical models for ion beam pattern formation of amorphous or amorphized elemental semiconductors will be discussed. In the coordinate system used the unperturbed surface is parallel to the x - y plane and the ion beam is parallel to the x - z plane.

Slope dependence of erosion

The sputtering yield $Y(\theta)$ (figure 2.5) depends on the local incidence angle θ (see figure 2.6).

The dependence of the sputtering yield on the local ion incidence angle θ leads to a dependence of the erosion rate on the local slope angle α . The height change due to the slope dependence of the sputtering yield is

$$\partial_t h|_{\text{slope}} = -\frac{jY(\theta) \cos \theta}{\cos \alpha} \quad (2.13)$$

which can be approximated for small slopes by

$$\partial_t h|_{\text{slope}} \approx -jY(\vartheta) \cos \vartheta + j(\partial_\theta Y(\vartheta) \cos \vartheta - Y(\vartheta) \sin \vartheta) \partial_x h. \quad (2.14)$$

Carter, Colligon, and Nobes [19] showed that the local incidence angles $\theta = 0^\circ, \theta_{\max}, 90^\circ$ are the only local incidence angles on a steady state surface if one take only the slope dependence of the sputtering yield into account.

Curvature dependent erosion

Bradley and Harper proposed a model for ion beam pattern formation combining the curvature dependence of the sputtering yield as the roughening mechanism and surface diffusion as the smoothing mechanism [14]. The curvature dependence of the sputtering is derived by assuming the number of sputtered atoms being proportional to the energy deposited there by neighboring impacts and the distribution of the deposited energy being ellipsoidal as in the model of Sigmund [126]. For small slopes and amplitudes the height evolution is given by

$$\partial_t h|_{\text{BH}} = S_x^{\text{BH}}(\vartheta)\partial_x^2 h + S_y^{\text{BH}}(\vartheta)\partial_y^2 h - D\nabla^4 h, \quad (2.15)$$

where the coefficients $S_x^{\text{BH}}(\vartheta), S_y^{\text{BH}}(\vartheta)$ include the dependence of the curvature dependent sputtering on the incidence angle ϑ and D the relaxation by surface diffusion. If $S_x^{\text{BH}} < 0$ or $S_y^{\text{BH}} < 0$ there is an instability for height modulations with wave vectors in x or y direction, respectively. Whether the direction of the wave vector of the ripple pattern is parallel or perpendicular to the projection of the ion beam onto the sample plane depends on the relative strength of S_x^{BH} and S_y^{BH} . If $-S_x^{\text{BH}} > -S_y^{\text{BH}}$ the wave vector is parallel to the projected ion beam direction and perpendicular if $-S_y^{\text{BH}} > -S_x^{\text{BH}}$. For all incidence angles $\vartheta < \vartheta_{\text{crit}}$ the surface is unstable in x direction in this model, i. e. $S_x^{\text{BH}} < 0$; for larger ϑ the surface is stable in x direction, i. e. $S_x^{\text{BH}} > 0$, while the surface is always unstable in y direction, i. e. $S_y^{\text{BH}} < 0$ for all ϑ , the instability in x direction is stronger for $\vartheta < \vartheta_{\text{crit}}$. A rotation of the ripple direction from a wave vector parallel to the projected ion beam for small incidence angles to a wave vector perpendicular to the ion beam for large incidence angles is predicted.

Surface relaxation

In the original model of Bradley and Harper [14] thermal Herring-Mullins type diffusion is the smoothing mechanism behind $D\nabla^4 h$. Depending on the actual conditions other mechanisms contribute to the smoothing: (1) Herring–Mullins type diffusion [14, 26, 61, 97, 98], (2) radiation enhanced viscous flow in the thin amorphous top layer of the surface [135], and (3) dependence of the erosion rate on higher derivatives of the surface height (“effective surface diffusion”) [87]. The relaxation mechanisms (1) and (2) are connected with mass transport along the surface. The driving force is the reduction of

2.3. Ion beam pattern formation of amorphous elemental semiconductors

the surface free energy. The surface currents of diffusion are given by

$$\mathbf{j}_S = -\frac{D_S n_S V \gamma}{k_B T} \nabla \kappa, \quad (2.16)$$

where κ is the surface curvature, n_S is the density of the mobile species which can be drastically above the equilibrium density by ion beam induced defects, V the atomic volume, γ is the surface tension, and $D_S \propto \exp(-E_D/(k_B T))$ with the activation energy E_D of surface diffusion [61, 97, 98]. For low temperatures the surface diffusivity is dominated by radiation enhanced diffusion and for higher temperatures the thermal diffusion becomes important. The height change is then in the linear limit ($\kappa \approx -\nabla^2 h$)

$$\partial_t h = -V \nabla \cdot \mathbf{j}_S = -D \nabla^4 h, \quad (2.17)$$

where the relaxation constant D is the sum of all contributions. The change in surface height due to radiation enhanced viscous flow is given by

$$\partial_t h = -\frac{\gamma d^3}{\eta} \nabla^4 h = -D_{VF} \nabla^4 h \quad (2.18)$$

in the shallow water approximation $d \ll \lambda$ [135]. The ‘‘effective surface diffusion’’ (3) is not connected with any mass transport. It originates from the dependence of the erosion rate on higher derivatives of the surface height [87].

Ballistic mass drift

Ions hitting a solid surface do not only sputter atoms but also displace atoms in the near surface layer. The momentum transferred from the impinging ion to the recoil atoms leads to a net mass drift in direction of the ion beam. Carter and Vishnyakov [20] derived an approximation for the ballistic surface atom flux

$$j^{\text{CV}} = j \cos(\theta) N_d(E) d_{\text{rec}} \sin(\theta) \quad (2.19)$$

where j is the ion flux density³, $\theta = \vartheta - \arcsin(\partial h / \partial x)$ the local incidence angle, $N_d(E)$ the number of recoils generated by an ion impact, and d_{rec} is the average distance the recoils travel in direction of the ion beam. In linear approximation, this leads to a change in the surface height of

$$\partial_t h|_{\text{CV}} = S_x^{\text{CV}} \partial_x^2 h = -\frac{j}{n} N_d(E) d_{\text{rec}} \cos(2\vartheta) \partial_x^2 h \quad (2.20)$$

which is smoothing for $\vartheta < 45^\circ$ and destabilizing for $\vartheta > 45^\circ$. This model predicts ripples with wave vector parallel to the ion beam direction for $\vartheta > 45^\circ$.

³ions per unit time and area

Crater functions

An approach to unify the contributions from erosion like the curvature dependent erosion rate and the ballistic mass drift in one theory is to use crater functions $\Delta h(x, y)$ which describe the average height change due to an ion impact. Norris et al. [105, 106] derived the height change due to ion impacts

$$\partial_i h|_{\text{CF}} = S_x^{\text{CF}}(\vartheta) \partial_x^2 h + S_y^{\text{CF}}(\vartheta) \partial_y^2 h \quad (2.21)$$

where $S_x^{\text{CF}}(\vartheta), S_y^{\text{CF}}(\vartheta)$ depend on the first moment $M_x^{(1)}(\vartheta) = \iint \Delta h(x, y) x \, dx \, dy$ of the crater functions

$$\begin{aligned} S_x^{\text{CF}}(\vartheta) &= j \frac{d}{d\vartheta} [M_x^{(1)}(\vartheta) \cos \vartheta] \\ S_y^{\text{CF}}(\vartheta) &= j M_x^{(1)}(\vartheta) \cos \vartheta \cot \vartheta \end{aligned} \quad (2.22)$$

Hydrodynamic model

Combining the ideas of roughening by ballistic mass drift and relaxation by ion induced viscous flow leads to the idea of describing the surface evolution as a highly viscous incompressible fluid film of thickness d [22]:

$$\nabla \cdot \mathbf{v} = 0, \quad (2.23)$$

where \mathbf{v} is the velocity field. The conservation of momentum can be expressed by the Stokes equation

$$0 = \nabla \cdot \mathbf{T} = -\nabla P + \eta \nabla^2 \mathbf{v} + \nabla \cdot \mathbf{T}^s \quad (2.24)$$

with

$$T_{ij} = -P \delta_{ij} + \eta \left(\frac{\partial v_j}{\partial x_i} + \frac{\partial v_i}{\partial x_j} \right) + T_{ij}^s. \quad (2.25)$$

The hydrostatic pressure P , the visous stress $\eta \left(\frac{\partial v_j}{\partial x_i} + \frac{\partial v_i}{\partial x_j} \right)$ and the ion beam induced stress \mathbf{T}^s contribute to the stress tensor \mathbf{T} . The ion beam induced stress can be described by an “effective body force” $\mathbf{b} = \nabla \cdot \mathbf{T}^s$ pointing into the direction of the ion beam. The magnitude of the body force $|\mathbf{b}| = f_E \Psi(\theta)$ depends on the local incidence angle θ of the ions. By solving the Stokes equation taking into account the surface tension γ at the surface and a no-slip condition at the interface between the amorphous layer and the crystalline substrate, Castro and Cuerno [22] showed that a small height modulation $h(x, t = 0) = h_k \exp(ikx)$ grows/diminishes exponentially in the linear approximation

2.3. Ion beam pattern formation of amorphous elemental semiconductors

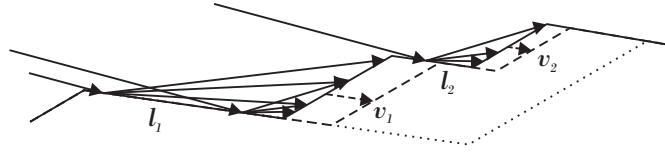


Figure 2.7.: Sketch to illustrate coarsening by reflected ions.

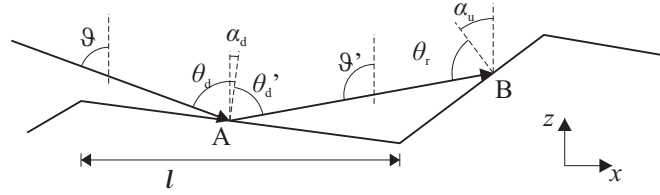


Figure 2.8.: Sketch of angles relevant for the discussion of the Hauffe mechanism (see text).

with the rate

$$\partial_t h_k = \omega(k) = -\frac{f_E \partial_\vartheta (\Psi(\vartheta) \sin(\vartheta)) d^3}{3\eta} k^2 - \frac{\gamma d^3}{3\eta} k^4 \quad (2.26)$$

With $\Psi(\vartheta) = \cos(\vartheta)$ and $f_E = 3\eta f(E) d_{rec}/n$ the ballistic mass drift model (eq. 2.20) by Carter and Vishnyakov with surface viscous flow as smoothing mechanism (eq. 2.18) is recovered.

Reflected ions

At grazing incidence angles, a large fraction of the incident ions are scattered by a sequence of small angle scattering events away from the surface. They do not penetrate the surface and are reflected with little energy loss [7]. The reflected ions can hit the surface again and contribute significantly to sputtering [116]. Hauffe [60] observed rapid coarsening of the surface morphology during 10 keV Ar^+ ion bombardment of Ag single crystals. He proposed that sputtering by reflected ions causes the observed coarsening. On a saw tooth profile like in figure 2.7 ions are reflected on the downwind facet and scattered with an angular distribution peaked near specular reflection. These reflected ions can hit the next upwind facet and increase the sputtering. The longer the downwind facet in front of an upwind facet is, the larger the increase of sputtering is at this upwind facet. Thus larger structure grow at the expense of small structures. This coarsening mechanism is also called Hauffe mechanism [131].

To estimate the erosion enhancement v_r at the point B (x_B, z_B) in a 2-dimensional model one has to integrate all fluxes $j'(E', A \rightarrow B) ds_A dE'$ of reflected particles with energy E' from all points A (x_A, z_A) on the downwind facet weighted by their sputtering

yields $Y(E', \theta_r)$. The differential length element ds_A is given by $ds_A = dx_A / \cos \alpha_d$. From figure 2.8 the following relations between the angles can be deduced

$$\alpha_d + \theta'_d = 180^\circ - \vartheta' \quad (2.27)$$

$$\vartheta' = \alpha_u + \theta_r \quad (2.28)$$

and the dependence of ϑ' from the point A

$$\tan \left(\vartheta' - \frac{\pi}{2} \right) = \frac{z_B - z_A}{x_B - x_A} = \frac{z_B - x_A \tan \alpha_u}{x_B - x_A}. \quad (2.29)$$

The flux from A to B $j'(E', A \rightarrow B) ds_A$ is proportional to the primary ion flux projected on to the downwind face $j_0 \cos \theta_d$, the fraction of ions reflected $Y_R(\theta_d, \theta'_d, E')$ with the energy E' at the angle θ'_d

$$j'(E', A \rightarrow B) ds_A dE' = j_0 \cos(\theta_d) \frac{Y_R(\theta_d, \theta'_d, E')}{r} ds_A dE' \quad (2.30)$$

with

$$r = \sqrt{(x_B - x_A)^2 + (z_B - z_A)^2} \quad (2.31)$$

Integrating over the downwind facet and all energies yields the erosion speed v_r from the reflected ions

$$v_r = \int \int_{-l/\cos \alpha_d}^0 j'(E', A \rightarrow B) Y(\theta_u) \cos(\theta_u) ds_A dE' \quad (2.32)$$

$$= j_0 \cos(\theta_d) \int_{-l/\cos \alpha_d}^0 \frac{Y_R(\theta_d, \theta'_d)}{r} Y(\theta_u) \cos(\theta_u) ds_A \quad (2.33)$$

which will increase with l if the angular distribution of reflected ions $Y_R(\theta'_d)$ is broad which is fulfilled in reality. For the extreme case of perfect specular reflection, when the angular distribution is a Dirac distribution $Y_R(\theta_d, \theta'_d) = \delta(\theta_d - \theta'_d)$, v_r does not depend on the length of the upwind face.

2.4. Pattern formation on crystalline surfaces

On crystalline surface ion beam pattern formation can be observed even at normal ion incidence and in absence of impurities. Normal incidence ion beam pattern formation has been reported for metal surfaces [24, 33, 67, 92, 94, 116, 119, 120] as well as for semiconductor surfaces at elevated temperatures [29, 53, 72, 73, 79, 82, 107, 109] which

2.4. Pattern formation on crystalline surfaces

remain crystalline at these temperatures. The patterns on crystalline surfaces can be aligned with substrates crystallographic directions [33, 67, 72, 73, 92, 94, 107, 119, 120] or especially for grazing incidence with the ion beam direction [116, 119].

The anisotropy of crystalline surfaces induces an anisotropic diffusion on the surfaces. The diffusion current is then $\mathbf{j} = \mathbf{D}\nabla\nabla^2h$ for Herring-Mullins type diffusion. The anisotropy can be accounted for by summing up the contributions along each principal crystallographic direction [33]. The height change due to diffusion is then

$$\partial_t h = \sum_{\mathbf{n}} -D_{\mathbf{n}}(\mathbf{n} \cdot \nabla)^4 h, \quad (2.34)$$

where \mathbf{n} is a principal crystallographic direction, and $D_{\mathbf{n}}$ is the diffusivity along this direction. During ion bombardment vacancies and adatom are created which diffuse on the surface. As more vacancies are produced due to sputtering, they dominate the evolution of the surface [28, 67].

Ehrlich-Schwoebel instability

The steps on a crystalline surface induce an effective mass current on the surface during ion bombardment. Ehrlich and Hudda [43] showed 1966 that adatoms on tungsten surfaces are reflected from the descending step edges. Schwoebel and Shipsey [122] explained these results theoretically by a potential energy barrier E_{ES} (Ehrlich-Schwoebel barrier) at the step edges. Adatoms diffusing to the ascending step edge are incorporated into the upper terrace. With increasing temperature, the effect of the Ehrlich-Schwoebel barrier diminishes. The probability of adatoms to cross the descending step increases $\propto \exp(-E_{\text{ES}}/k_{\text{B}}T)$ with temperature. Crossing the descending step edge is a thermally activated process for adatoms. In non-equilibrium conditions like ion bombardment, where mobile surface defects are created constantly, the Ehrlich-Schwoebel barrier induces a mass current along a stepped surface [75, 125, 136]. Vacancies, which are the mobile defects created by ion beam sputtering, are reflected by ascending step edges, thus leading to an effective uphill mass current [28, 67, 111, 112]. For small slopes the current is

$$\mathbf{j} = -S_{\text{ES}}\nabla h \quad (2.35)$$

where $-S_{\text{ES}}$ is a positive constant proportional to the rate with which the mobile defects are created and to the probability $1 - \exp(-E_{\text{ES}}/(k_{\text{B}}T))$ that vacancies are reflected at the Ehrlich-Schwoebel barrier E_{ES} .

For large slopes this approximation cannot hold, as at some point the slope corresponds to another low index plane and the Ehrlich-Schwoebel current must vanish.

2.5. Metal induced pattern formation

On elemental Si, patterns form only for ion incidence angles ϑ larger than a critical incidence angle ϑ_{crit} at low temperatures [81, 83, 84, 86]. For near normal incidence angles $\vartheta < \vartheta_{\text{crit}}$ even smoothing has been observed [81, 109, 150].

Pattern formation for ion bombardment at room temperature with incidence angles ϑ below the critical angle ϑ_{crit} is only possible when metal impurities are deposited onto the surface during ion bombardment [32, 81, 84, 108, 109, 149]. After this has been shown first by Ozaydin et al. with Mo seeding [108], more metals have been identified to induce pattern formation. The identified pattern forming metals are Mo [62, 108, 109, 130], Fe [31, 32, 62, 80–82, 121, 143, 147, 149, 150], Pt, W and Ni [62]. All of these metals form silicides with enthalpies of formation of 24 kJ/mol to 120 kJ/mol [114]. Au, which does not form a silicide, does not induce pattern formation [62]. Cu forms only silicides with much metal as Cu_3Si is the most silicon rich silicide with a low enthalpy of formation [114]. Thus, only very high Cu concentrations induce pattern formation [62].

The deposition of a metal during ion bombardment changes the composition of a surface near layer. After a time the surface layer with thickness d of a perfectly flat and homogeneous surface reaches a steady state in which the metal concentration $c = c_0$ does not change as the amount of metal sputtered away $\Phi_{\text{ion}}Y_m(c_0)$ is equal to the metal flux Φ_m . For small metal concentration it is reasonable to assume that $Y_m(c)$ is a monotonically increasing function such that the steady state concentration c_0 is uniquely defined. Infinitesimal perturbations however start a destabilization of the surface which will be discussed below.

For ion beam pattern formation in two component systems like in the situation here, where a metal is concurrently deposited during ion bombardment, different models have been proposed.

1. Zhang et al. and Hofsäss et al. [62, 143, 147] proposed a model for pattern formation with co-deposition of metal impurities. In this model phase separation into metal rich and metal poor regions triggers pattern formation. The dependence of the erosion rate then transforms the concentration modulation into a height modulation. Recently Norris [104] developed an analytical model where the pattern formation is triggered by phase separation due to spinodal decomposition (see section 2.2). During ion bombardment the surface near layer develops a steady state surface composition which is different from the bulk composition of the substrate which is especially the case for co-deposition of metal impurities. If the composition deviates sufficiently from a stable equilibrium composition, spinodal decomposition produces composition modulation. The dependence of the erosion rate on the composition then transforms the composition modulation into a height modulation. The model is a system of two coupled partial differential equations

2.5. Metal induced pattern formation

(PDEs) for the height modulations u and the composition modulations ϕ

$$\frac{\partial u}{\partial t} = -A\phi + B\nabla^2 u - C\nabla^4 u \quad (2.36)$$

$$\frac{\partial \phi}{\partial t} = -A'\phi + D'\nabla^2 \phi - E'\nabla^4 \phi + B'\nabla^2 u \quad (2.37)$$

where u and ϕ are the deviations from a flat, homogeneous surface. The concentration dependence of the sputtering yields enters through $A = j_{\text{ion}} \cos \vartheta V (\partial_c Y_m + \partial_c Y_{\text{Si}})$ and $A' = j_{\text{ion}} \cos \vartheta (V/d) ((1 - c_0) \partial_c Y_m + c_0 \partial_c Y_{\text{Si}})$ which is usually positive, with the atomic volume V . The ballistic mass drift and curvature dependent sputtering are described by B which is positive for near normal ion incidence. The difference in the strength of the ballistic mass drift B' of both components can change the composition by driving one species preferentially in the valleys. The viscous flow relaxation C is assumed to be the same for both species and not changing the composition. Chemical diffusion and ion beam mixing contribute to $D' = M \partial^2 f(c_0) / \partial c^2 + D_{\text{mix}}$ (compare equations (2.6), (2.10)) which will be negative if $\partial^2 f(c_0) / \partial c^2$ is sufficiently negative such that the spinodal decomposition is stronger than ion beam mixing. The free energy cost of a concentration gradient is encoded in $E' = M\kappa$ as in the theory of spinodal decomposition (compare equation (2.10)). The spinodal decomposition leads then to a compositional modulation which produces a height modulation due to dependence of the erosion rate on the composition $-A\phi$. In the limit $AB' \ll BA'$ called “limit of weak coupling” Norris showed that the wavelength is

$$\lambda = 2\pi \sqrt{\frac{-D'}{2E'}} \quad (2.38)$$

if $-A\phi$ and $B'\nabla^2 k$ are neglected in the PDEs. The instability occurs only if

$$\frac{B'^2}{4E'} > A'. \quad (2.39)$$

This means that the strength of spinodal decomposition must be stronger than the restoration to the steady state concentration by changing the partial sputtering yields with concentration. In the case of co-deposition of silicide forming metals, the metal rich patches will be eroded slower and the metal concentration is higher at top than in the valleys.

2. Macko et al. [80] proposed 2011 that pattern formation could also be initiated by the dependence of the deposition flux on the local slope. For oblique deposition on side of a height modulation will receive a higher impurity flux than the other. This leads to differences in erosion rate which amplify the height modulation and thus to larger slopes and larger local flux modulations. Bradley [9] developed 2013

an analytical model of the mechanism described above. In this model he takes the reduction of the sputtering yield by silicide formation into account, in contrast to his model from 2012 [10] where the instability only occurs if the impurity has a lower sputtering yield than the substrate. The basis of Bradley's model is that the local deposition flux Φ_m depends on the local slope

$$\Phi_m = \mathbf{j}_m \cdot \mathbf{n} \quad (2.40)$$

where $\mathbf{j}_m = j_m \mathbf{n}_m$ is the metal flux density, \mathbf{n}_m is the direction of the metal beam parallel to the x - z plane and \mathbf{n} is the local surface normal. For small amplitude deviations u from a flat plane Φ_m can be expanded linearly in $\partial h/\partial x = \partial u/\partial x$

$$\Phi_m = j_m \cos \theta_m - j_m \sin \theta_m \frac{\partial u}{\partial x}. \quad (2.41)$$

This leads to an instability even in the absence of surface diffusion and thus spinodal decomposition. The PDEs for the deviations from the flat and homogeneous steady state are

$$\frac{\partial u}{\partial t} = -A\phi - F \frac{\partial u}{\partial x} + C\nabla^2 u - D\nabla^4 u \quad (2.42)$$

$$\frac{\partial \phi}{\partial t} = -A'\phi - F' \frac{\partial u}{\partial x} + C'\nabla^2 u - D'\nabla^4 u \quad (2.43)$$

where A , A' , C , C' and D have the same meanings as in equations (2.36) and (2.36). The dependence of the local deposition flux on the surface slopes is encoded in $F = j_m V \sin \vartheta_m$ and $F' = j_m (V/d) \sin \vartheta_m$ and D' encodes the change in composition due to viscous flow relaxation. This leads to an instability if the impurity to ion flux ratio Φ_m/Φ_{ion} exceeds a critical value Φ_c/Φ_{ion} which decreases with increasing incidence angle ϑ_m of the impurity deposition. This critical flux is required to overcome the smoothing due to the ballistic mass drift for normal ion incidence. For impurity fluxes slightly above the critical flux the pattern wavelength diverges like

$$\lambda \propto \frac{1}{\sqrt{\Phi_m/\Phi_{\text{ion}} - \Phi_c/\Phi_{\text{ion}}}}. \quad (2.44)$$

2.6. Si(001)

Silicon (Si) has a diamond crystal structure with a lattice constant $a = 5.43 \text{ \AA}$ [141]. In the following properties of the Si(001) surface important for ion beam pattern formation will be shortly discussed. The Si(001) surface is shown in figure 2.9 with the characteristic dimer reconstruction. Surface atoms would have two dangling bonds without the reconstruction. By forming dimers they can saturate one of the dangling bonds. The

2.6. Si(001)

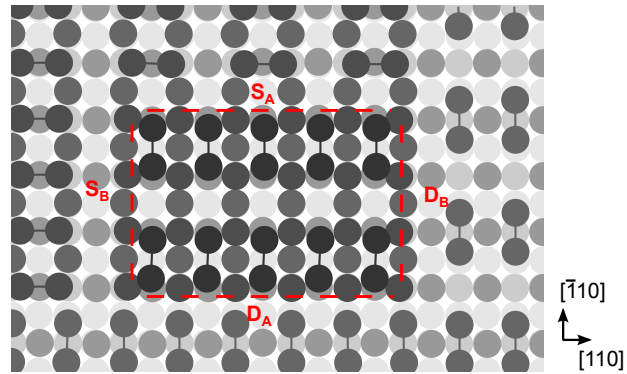


Figure 2.9.: Si(001) surface.

dimers form rows in a $c(4 \times 2)$ reconstruction [56, 134]. The direction of the dimer rows alternates between $[110]$ and $[\bar{1}10]$ on the different terraces.

The step edges on Si(001) are categorized according to direction of the dimer rows on the upper terrace. If the dimer rows on the upper terrace are parallel to the step edge then the steps are called S_A or D_A steps for single and double steps, respectively. On the other hand, if the dimer rows on upper terrace are perpendicular to the step edge then the steps are of S_B or D_B type, respectively [142]. The different types of steps are highlighted in figure 2.9.

Diffusion on Si(001) is highly anisotropic. Adatoms and vacancies diffuse along the direction of the dimer rows, while diffusion perpendicular to the dimer rows is hindered [95, 138].

3. Methods

3.1. UHV system *Athene*

The experiments were conducted in the ultra high vacuum (UHV) system *Athene* with a base pressure below 6×10^{-11} mbar. The base pressure is reached using a turbomolecular pump, an ion getter pump, and a titanium sublimation pump. By filling a cold trap with liquid nitrogen the chamber pressure can be reduced down to 2×10^{-11} mbar. A sample transfer load lock allows exchange of samples without breaking the vacuum. Up to three samples can be stored in a sample garage in the system. For sample preparation the system is equipped with a differentially pumped scannable fine focus ion source. Due to the differential pumping the chamber pressure stays below 2×10^{-8} mbar during ion bombardment. The ion current is measured with a Faraday cup moved to the sample position. The Faraday cup is mounted behind a plate with a hole of 1 mm diameter. Two electron beam evaporators can be used to co-evaporate metal onto the sample during ion bombardment: a transferable four pocket evaporator at 60° to the ion source evaporating from rods and a fixed evaporator at 105° to the ion source evaporating from a metal plate. The system is also equipped with a quadrupole mass spectrometer, two Knudsen cells, a quartz microbalance for the Knudsen cells, and gas inlets. The sample holder mount at the manipulator is equipped with an electron beam heating system and a movable type K thermocouple, which can be attached to the sample surface near the edge of the sample. The sample holder mount is connected by two copper braids with a flow cryostat for cooling. The manipulator can be translated along one axis and rotated $\pm 180^\circ$ around the same axis allowing arbitrary ion incidence angles during ion bombardment. For sample analysis the system is equipped with a scanning tunneling microscope (STM)¹ and a three grid low energy electron diffraction (LEED) system.

3.2. Calibration of the movable thermocouple

As the movable thermocouple measures the sample temperature near the edge of the sample and the clips holding the sample, the temperature measured with the thermocouple T_{disp} can be lower than at the center of the sample. During the course of the experiments the thermocouple broke and had to be replaced. To calibrate the old and the new thermocouple, we observed the melting of In and Pb with melting points T_{melt}

¹For details of the STM design see [48, 93]

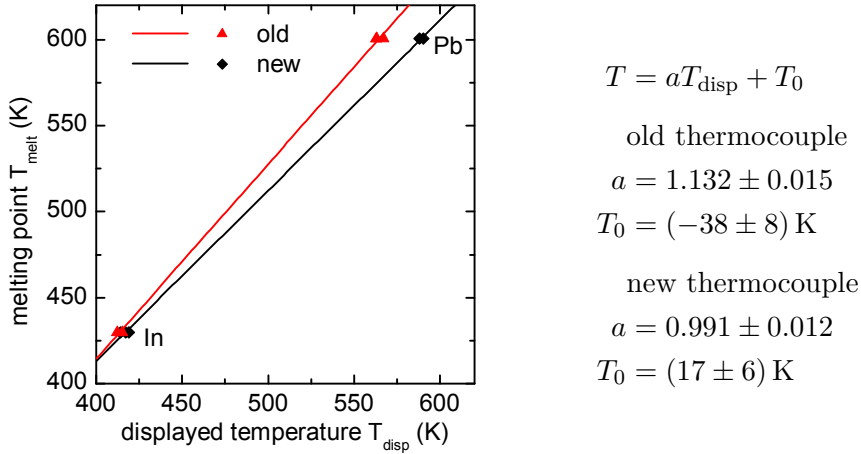


Figure 3.1.: Calibration of the movable thermocouple.

of 430 K and 601 K [141], respectively, using a telescope. Two Si samples with a droplet of either metal in the center were prepared by melting a small amount of the metal on the sample surface. After mounting the sample the thermocouple was attached to the sample and the sample was heated to $T_{\text{disp}} \approx T_{\text{melt}} - 50 \text{ K}$. Then the sample was slowly heated with a rate between 1 K/min and 10 K/min. When movement at the droplet surface was visible, the reading from the thermocouple T_{disp} was taken as measured value for the melting point. This procedure was repeated a few times for each metal. Figure 3.1 shows the literature melting points T_{melt} plotted against the readings from the thermocouple T_{disp} and the linear fits used for calibrating the temperature measurement for both thermocouples.

3.3. Sample preparation

Samples

The samples used here are 9 mm \times 9 mm pieces cut from commercial, front polished, n-doped Si(001) wafers with an orientation tolerance of $\pm 0.05^\circ$. The wafers were cut along the $\langle 110 \rangle$ directions. The Si pieces were mounted on a molybdenum sample holder. The sample rests on three sapphire balls and is fixed using tungsten springs which provide also electrical contact to the sample holder. Before transferring into the vacuum system dust was blown away using dry and oil free nitrogen.

Ion bombardment

We used Kr^+ ions with 2 keV energy for ion bombardment. The ion source produces a focused beam which is scanned over the sample with a repetition rate of $\approx 100 \text{ Hz}$ and line scan frequency $\approx 1000 \text{ Hz}$ leading to homogeneous time averaged ion flux in the

3.3. Sample preparation

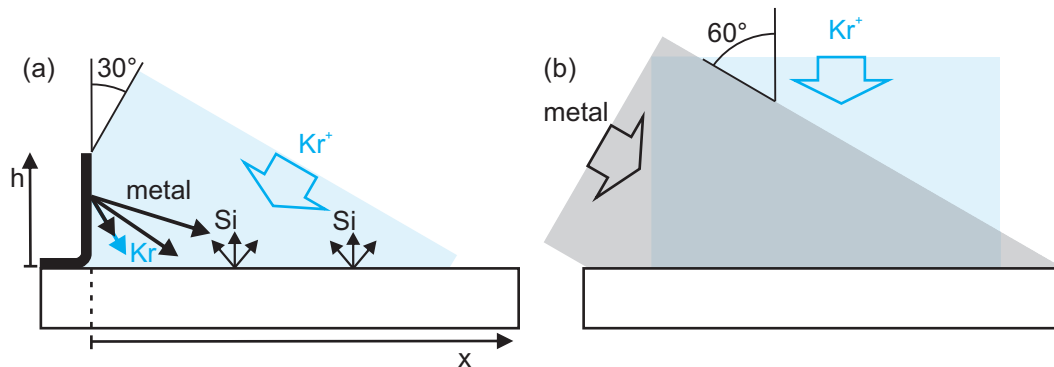


Figure 3.2.: (a) Sputter co-deposition setup, (b) co-evaporation setup.

scanned area. The flux can be controlled with the gas pressure in the ion source and the size of the scanned area. During the experiments the pressure in the ion source was kept constant with a controllable leak valve. Before and after the experiments the ion flux was checked using the Faraday cup moved in the sample position. The difference of the ion fluxes before and after the experiment was less than 10%. The samples were aligned such that the projection of the ion beam on the sample plane is parallel to the Si [1 1 0] direction.

Metal co-deposition

Two experimental setups were employed for co-deposition of metal impurities during ion bombardment. Elemental Ag, Pb, Pd, Ir (purity for all: 99.9%), and stainless steel² were co-deposited.

The first is the sputter co-deposition setup (figure 3.2(a)). A metal target made of a bend high purity metal foil is mounted on the silicon sample. The target is $h = 1.4$ mm high allowing in-situ STM measurement. A higher target would collide with the STM piezo scanner. The incidence angle ϑ of the ion beam is set to $\vartheta = 30^\circ$ and the scan area of the beam is chosen such that the metal target is hit by the ion beam during the experiment. Measurements were taken along a line perpendicular to the metal target starting at the center of front face of the metal target. TRIM.SP calculations (for details see chapter 3.6) combined with numerical integration for a pure metal target show that the flux ratio decreases with x .³ This setup allows to test a wide range of flux ratios depending on the distance x from the metal target in one experiment. Although sputter co-deposition is a fast method to test many conditions in one experiment, the interpretation is complicated for several reasons: The incidence angle of the metal sputtered onto the Si sample covers the range from $\vartheta_M = \arctan(x/h)$

²steel type EN 10027: 1.4021, composition 84% Fe, 13% Cr, 0.2% C

³See appendix A for details.

to $\vartheta_M = 90^\circ$. The metal atoms have a non-thermal energy distribution with an average energy of the order of 50 eV according to TRIM.SP calculations. Additional particle fluxes have to be considered, too. A fraction of ions impinging the metal target are scattered from the target and hit the sample. Their angular distribution is more narrow than for the sputtered atoms and peaked close to specular reflection. The average energy of the reflected ions is substantial in the order of 500 eV. The flux ratio of scattered Kr^+ ions to primary ions on the substrate is small < 0.06 . The second flux are sputtered Si atoms. Si is sputtered from the sample onto the target which will lead to a Si enriched layer at the surface of the metal target. This leads to an additional flux of Si atoms sputtered from the target onto the sample with an energy distribution similar to the metal atoms. TRIM.SP and numerical integration showed that the metal flux from the target to the sample and the Si flux from the sample to the target are of similar magnitude. This additional flux from the sample to the target leads to a change of target composition during the experiment. Also, the surface morphology of the target is modified by the ion bombardment during the experiment. The main advantage of this method is, that it allows to study a wide range of flux ratios in one experiment.

The second setup is the co-evaporation setup (figure 3.2(b)). The metal impurities are supplied by evaporation from an electron beam evaporator at an oblique incidence angle $\vartheta_M = 60^\circ$, whereas the ion beam is normal to the surface. The metal flux Φ_M has been checked before and after the experiment by measuring the size of pseudomorphic islands on an Ir(111) sample after a fixed evaporation time. The ion flux Φ_{Kr} has been adjusted to set a desired flux ratio Φ_M/Φ_{Kr} for the given metal flux. This setup provides a homogenous metal flux over a large area and avoids additional fluxes complicating the interpretation of the results.

Elevated temperature ion bombardment

For ion bombardment at elevated temperatures the sample has to be kept for an extended period of up to 3 h at a constant temperature. To achieve this the sample was heated with electron beam heating from the backside. The experimental procedure was the following:

1. The movable thermocouple was attached to the sample and the temperature is measured until the start of ion bombardment.
2. The sample was slowly heated over 30 min to 60 min to the temperature of the experiment.
3. The ion source was set to the desired ion flux, which was measured using the Faraday cup.
4. The sample was moved in front of the ion gun.

3.4. Methods of sample analysis

5. The sample was held at constant temperature for 15 min to 60 min until the temperature of the sample holder and the required heating power stabilized.
6. The sample was bombarded with the ions.
7. The sample temperature was measured again with the movable thermocouple.
8. The heating was switched off in less than 2 min after the end of ion bombardment. The sample was quenched in less than 30 s to temperatures below 500 K after switching off the heating. It took additional 45 min to cool down to room temperature.
9. After measuring the ion flux again and closing the gas supply to the ion source, the cooling trap was filled and the titanium sublimation pump as well as the ion getter pump were activated. Then the pressure fell below 10^{-10} mbar within 10 min after the end of ion bombardment.

3.4. Methods of sample analysis

The surface topography was analyzed in situ with scanning tunneling microscopy (STM). In situ low energy electron diffraction (LEED) allows to quickly determine if the surface is crystalline or amorphous. Several complimentary ex situ techniques have been employed for sample analysis.

The surface morphology has been analyzed ex situ with atomic force microscopy (AFM) using a closed-loop AFM and scanning electron microscopy (SEM) at the Leibniz Institute of Surface Modification (IOM).

The chemical composition of the samples with co-deposited metals has been analyzed with Rutherford backscattering spectrometry (RBS) at the LIPSION accelerator at the University of Leipzig. By fitting the measured energy spectrum with a simulated spectrum using the software RUMP [39] the area densities of foreign elements in the silicon matrix can be estimated. A 2 MeV He^+ ion beam with a diameter of 0.2 mm and 0.4 mm was used to investigate the sputter co-deposition and co-evaporation samples, respectively. The Cornell geometry (see figure 3.5) with an incidence angle of $\vartheta_{\text{in}} = 35^\circ$ and a scattering angle of $\theta = 171^\circ$ was used.

Transmission electron microscopy (TEM) of cross-sections allows to study the structure of the pattern and the layers below the surface. High-resolution TEM (HRTEM) and energy filtered TEM show the crystalline structure and the chemical composition, respectively. The TEM measurements were performed at the Helmholtz-Zentrum Dresden-Rossendorf (HZDR) where also the sample was prepared using a classical TEM preparation. The crystal structure has been determined by comparing the Fourier transform of HRTEM images with diffraction patterns simulated using the JEMS software package [128].

Scanning tunneling microscopy

Scanning tunneling microscopy (STM) is a scanning probe technique based on the quantum mechanical tunneling between a sharp tip and the sample surface.⁴ In one dimension the tunneling current depends exponentially on the tip-sample separation $z - z_s$ in the Wentzel-Kramers-Brillouin (WKB) approximation

$$I(z) \propto \exp\left(-\frac{\sqrt{2m\bar{\Phi}}(z - z_s)}{\hbar}\right) \quad (3.1)$$

with the apparent barrier height $\bar{\Phi} = \frac{1}{2}(\Phi_s + \Phi_t - eU)$, where Φ_s , Φ_t are the work functions of the sample and the tip, respectively, and U is the voltage between tip and sample [50]. Here the STM was operated in constant-current mode, i. e. the current is held constant by changing the displacement z of the tip by a feedback loop. The topography $h(x, y)$ of the sample is acquired by scanning the tip over the sample and recording the tip displacement $z(x, y)$.

A more sophisticated model of scanning tunneling microscopy has been developed by Tersoff and Hamann [132]. They approximated the tip as a free-electron-metal ball with radius R centered at \mathbf{r}_0 . Assuming that only s-wave tip wavefunctions contribute to tunneling, they derived that the tunneling current depends on the surface local density of states at \mathbf{r}_0 :

$$I \propto R^2 \exp\left(\frac{2\sqrt{2m\bar{\Phi}}R}{\hbar}\right) \rho(\mathbf{r}_0, E_F). \quad (3.2)$$

Thus, constant current imaging in STM follows a surface of constant local density of states.

Atomic force microscopy

Atomic force microscopy (AFM) is a scanning probe microscopy technique using the force between the tip and surface.⁵ Figure 3.3 shows a sketch of the force-distance curve. Negative forces are attractive and positive forces are repulsive. Far away from the surface the tip-surface interaction is attractive, whereas close to the surface the interaction becomes strongly repulsive [40]. A basic AFM setup is sketched in figure 3.4. Usually the tip is attached to a cantilever. The bending of the cantilever, which depends on the force, is measured by the deflection of a reflected laser beam using a segmented photo diode. The basic principle of operation of AFM is scanning the sample surface laterally with a sharp tip and maintaining a constant distance to the sample by adjusting the height of the tip. Then the height of the tip gives the topography of the surface. How

⁴A comprehensive review of STM can be found in reference [27].

⁵For a review of AFM see reference [40]

3.4. Methods of sample analysis

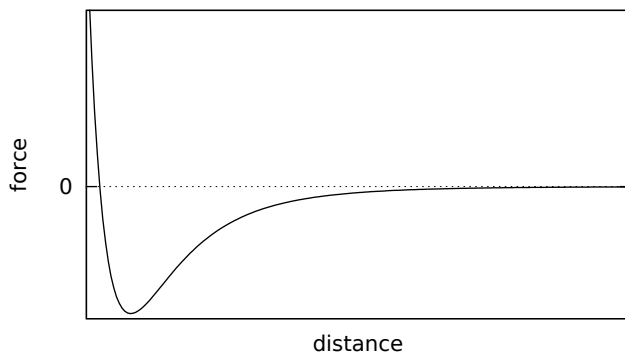


Figure 3.3.: Sketch of force-distance curve for AFM

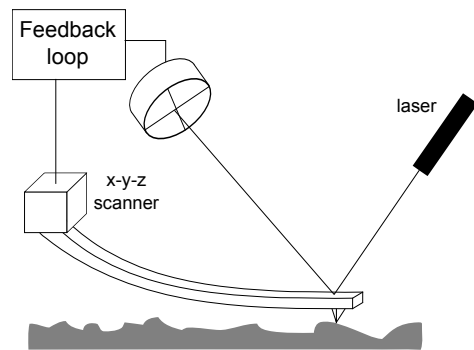


Figure 3.4.: Sketch of an AFM setup

a constant distance is maintained depends on the mode of operation.

The simplest mode is the *contact mode*. In this mode the tip is approached into the repulsive force range. The force increases strongly with decreasing distance. A feedback loop keeps the deflection of the laser beam constant by adjusting the tip height. Thus the repulsive force is kept constant. Due to the close distance between tip and sample strong lateral forces can occur especially in rough areas. These forces can damage the sample or tip.

In another way of operation the cantilever is excited to oscillate and the change of the cantilever oscillation during scanning is determined either by the change of the amplitude, the resonance frequency of the oscillation, or the phase between excitation and oscillation. For small oscillation amplitudes the force F between tip and surface is effectively changing the spring constant of the oscillator $k = k_0 - \frac{dF}{dz}$ where k_0 is the spring constant of the oscillator far away from the surface. The resulting change in the resonance frequency is measured usually by the change of the phase difference between driving force and cantilever oscillation. During scanning the phase difference is kept constant by adjusting the tip height. This mode is called *non-contact* or *close-contact mode*. As the forces are much lower than in contact mode this mode is especially suitable for soft samples. A drawback of this method is that under ambient conditions the sample is usually covered with an adsorbate layer which exerts additional capillary forces to the tip. Thus this mode is used usually in vacuum, where these capillary forces are not present [40].

A third mode of operation using oscillating cantilevers is the *tapping* or *intermittent contact mode*. In this mode the oscillation amplitude of the cantilever is much larger, typically 1 nm to 100 nm [40]. The tip moves from the zero force range far away, through intermediate the attractive range into the repulsive range and back during one oscillation period. The contact with the sample in the repulsive range reduces the oscillation amplitude. During scanning the tip height is adjusted to maintain a constant oscillation amplitude. Due to the short time in close contact the lateral forces are mostly eliminated and the influence of capillary forces is minimized.

The tip is scanned over the surface using a piezo tube. The scanning can be done in *open*

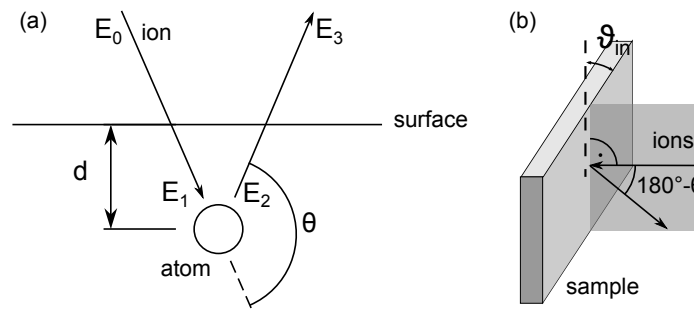


Figure 3.5.: (a) Sketch of the scattering geometry in Rutherford backscattering spectrometry (RBS), (b) Cornell geometry.

or *closed loop* mode. In the open loop mode the position is determined from the voltages applied to the scan piezos. In the closed loop mode an additional position sensor, e. g. a capacitive sensor, is mounted to the piezo scanner and the piezo voltage is adjusted by a feedback loop to reach the set position. This avoids non-linearity, creep, and hysteresis of the scan piezos. However the lateral resolution is limited by the resolution of the position sensor.

Rutherford backscattering spectrometry

Rutherford backscattering spectrometry (RBS) uses the energy of backscattered ions to estimate the composition of a sample. A beam of light ions – usually protons or $^4\text{He}^+$ ions – is accelerated to a few MeV and focused on the sample surface, while the energy spectrum of the ions backscattered under the scattering angle θ is measured [91]. Figure 3.5(a) shows a sketch of the scattering geometry. The Cornell geometry used here is shown in figure 3.5(b). In the Cornell geometry the rotation axis of the sample, the incident beam, and the exit beam are in the same plane. The scattering angle θ is connected to the incidence angle ϑ_{in} and the exit angle ϑ_{out} by

$$\cos \vartheta_{\text{out}} = \cos \vartheta_{\text{in}} \cos \theta. \quad (3.3)$$

The angles ϑ_{in} and ϑ_{out} are measured with respect to sample surface normal. As backscattering is only possible for $M_{\text{ion}} < M_{\text{target}}$, only atoms lighter than the projectile can be detected.

The energy of the backscattered ion depends on the mass M_{target} of the backscattering atom

$$E_2 = E_1 K \quad (3.4)$$

$$K = \frac{M_{\text{ion}}^2}{(M_{\text{ion}} + M_{\text{target}})^2} \left[\cos \theta + \left(\frac{M_{\text{target}}^2}{M_{\text{ion}}^2} - \sin^2 \theta \right)^{1/2} \right]^2 \quad (3.5)$$

3.5. Image analysis

for target atoms heavier than the ion (compare equation (2.2) in chapter 2.1). K is the kinematic factor. The energy loss is larger the larger the scattering angle θ . Thus a large scattering angle improves the mass resolution for a given instrumental energy resolution.

In addition to the energy loss at the backscattering event the ion loses energy before and after backscattering due to nuclear and electronic stopping (see chapter 2.1). If E_0 is the initial ion energy than the energy before backscattering is

$$E_1 = E_0 - \int_0^{d/\cos\vartheta_{\text{in}}} \frac{dE}{dx} dx \quad (3.6)$$

where d is the depth of backscattering atom (see figure 3.5(a)), ϑ_{in} is the incidence angle of the ion beam on the surface, and $\frac{dE}{dx}$ is the stopping power. The backscattered ion again loses energy due to stopping and the final energy is

$$\begin{aligned} E_3 &= E_2 - \int_0^{d/\cos\vartheta_{\text{out}}} \frac{dE}{dx} dx \\ &= \left(E_0 - \int_0^{d/\cos\vartheta_{\text{in}}} \frac{dE}{dx} dx \right) K - \int_0^{d/\cos\vartheta_{\text{out}}} \frac{dE}{dx} dx \end{aligned} \quad (3.7)$$

where ϑ_{out} is the exit angle of the ion beam reaching the detector. If the stopping power is known, the energy spectrum can be calculated for a given composition profile of the sample. The sample composition is estimated by fitting the model composition profile to the measured spectrum. For fitting also the straggling of the ion path has to be accounted for.

3.5. Image analysis

The STM and AFM topographs were analyzed using WSxM [65] and Gwyddion [101]. For determining the roughness σ a background has to be subtracted. After subtracting a global plane the STM images were corrected by subtracting a parabolic surface to compensate for piezo creep and drift. The AFM images were corrected by subtracting the average height from each line. As roughness the root mean square roughness

$$\sigma = \sqrt{\langle h_{ij} - \langle h_{ij} \rangle \rangle} = \left(\frac{1}{NM} \sum_{i=1}^N \sum_{j=1}^M (h_{ij} - \langle h_{ij} \rangle)^2 \right)^{1/2} \quad (3.8)$$

is used where N and M are the number of rows and columns in the image and $\langle \dots \rangle$ is the average over all points. For analyzing the wavelength two methods have been employed.

(a) The position of the first peak in the radial power spectral density function (PSD)

$$P(k) = \int_0^{2\pi} |F(k \cos \phi, k \sin \phi)|^2 k \, d\phi \quad (3.9)$$

is evaluated, where $F(k_x, k_y)$ is the Fourier transform of the topography. The wavelength is then $\lambda = 2\pi/k$. (b) The distance d_i between neighboring maxima along profiles in ion beam direction is measured $N > 100$ times. The wavelength is then the average distance

$$\lambda = \langle d_i \rangle = \frac{1}{N} \sum_{i=1}^N d_i. \quad (3.10)$$

Both methods yield the same wavelength if the PSD has a peak. Method (b) can also be applied to evaluate the average structure size of surfaces with a broad distribution of structure sizes and little order. The normalized standard deviation of the length distribution

$$\frac{\delta\lambda}{\lambda} = \frac{1}{\lambda} \left(\frac{\sum_{i=1}^N (d_i - \lambda)^2}{N - 1} \right)^{1/2} \quad (3.11)$$

is a measure for the disorder in the pattern.

Slope angles

The inclination of a surface element can be characterized by two angles (see figure 3.6(a)): 1) the slope angle α with respect to the x - y -plane which is equal to the angle of the local surface normal \mathbf{n} to the z -axis, 2) the azimuthal angle ϕ between the projection of the surface normal to the x - y -plane and the x -axis. The distribution of surface inclinations was calculated using a self written software. After the background correction described above was applied, the topography data $h_{i,j}$ (figure 3.6(b)) was exported and read by the program. The calculation is based on calculating the local surface normal on every image point (i, j) by using the central finite differences approximation

$$\mathbf{n}_{i,j} = \begin{pmatrix} -\frac{h_{i+1,j} - h_{i-1,j}}{2\Delta x} \\ -\frac{h_{i,j+1} - h_{i,j-1}}{2\Delta y} \\ 1 \end{pmatrix} \quad (3.12)$$

where Δx and Δy are spacings between two image points in x and y direction. The local surface slope angles $\alpha_{i,j}$ and azimuthal angles $\varphi_{i,j}$ are then

$$\alpha_{i,j} = \arccos \left(\frac{1}{|\mathbf{n}_{i,j}|} \right) \quad \text{and} \quad \varphi_{i,j} = \arctan \left(\frac{n_{i,j}^y}{n_{i,j}^x} \right) \quad (3.13)$$

3.5. Image analysis

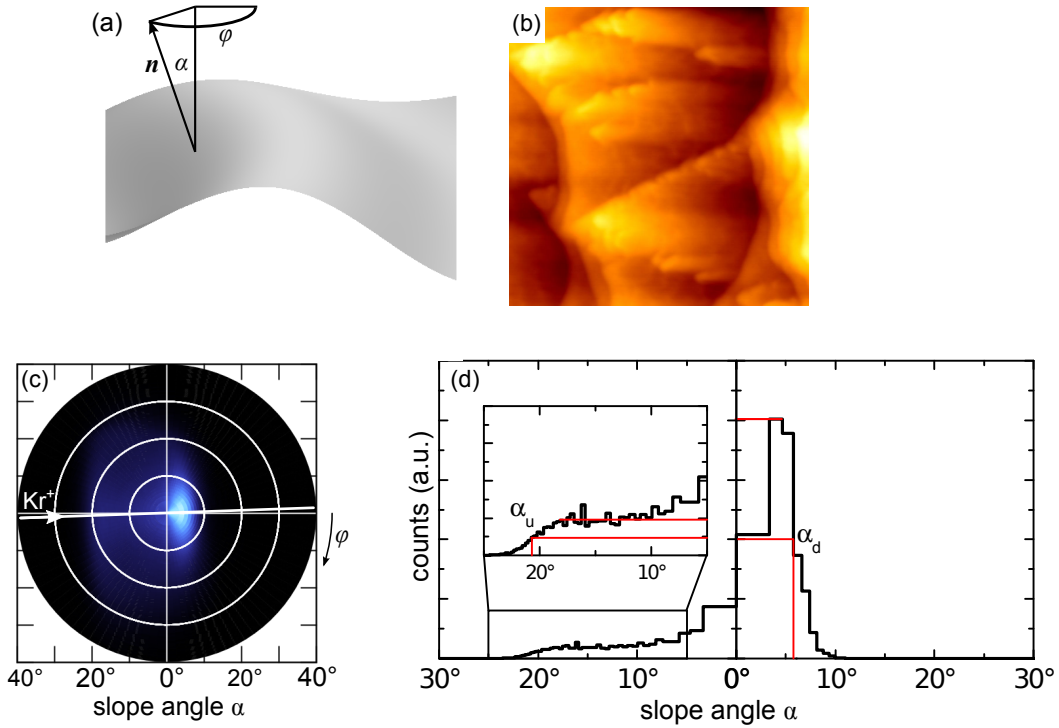


Figure 3.6.: Determination of slope distributions: (a) Definition of the slope angles, (b) $1 \mu\text{m} \times 1 \mu\text{m}$ AFM topograph, (c) polar histogram of (b), (d) cut along white line through (b)

where $n_{i,j}^{x,y}$ are the x - and y -components of $\mathbf{n}_{i,j}$. The distribution of the slope angles (figure 3.6(c)) can be obtained by calculating a two dimensional histogram of $(\alpha_{i,j}, \varphi_{i,j})$ with a binning which guarantees equal statistical weights of each bin. The azimuthal angle interval $\varphi \in [0, 2\pi)$ is divided into N_φ equally sized intervals $I_m^\varphi = [2(m-1)\pi/N_\varphi, 2m\pi/N_\varphi)$ with $m = 1, \dots, N_\varphi$. The polar angle interval $\alpha \in [0, \pi/2)$ is divided into N_α intervals $I_n^\alpha = [\alpha_{n-1}, \alpha_n)$ with $\alpha_n = \arccos(1 - n/N_\alpha)$ with $n = 0, \dots, N_\alpha$. The number of image points with inclinations $(\alpha_{i,j}, \varphi_{i,j}) \in I_n^\alpha \times I_m^\varphi$ is counted.

Figure 3.6(d) shows a cut through the slope angle distribution along the ion beam direction. The maximum slope angles α_u of the upwind and α_d of the downwind face were determined as described in the following. For the upwind face α_u is the angle where the intensity drops to half of the plateau value marked by the upper red line in the inset of figure 3.6(d) and for the downwind face α_d is the angle where the intensity drops to the half of the maximum.

For the downwind face with the pronounced maximum in the slope angle distribution, alternatively one might have chosen the position of the maximum as characteristic slope angle, resulting in values of α_d about 3° to 4° smaller. However, there is no maximum in the slope angle distribution for the upwind face, implying an asymmetry in the evaluation of α_u and α_d with such a choice. The convention chosen here is unambiguous and emphasizes the maximum slopes present in the morphology.

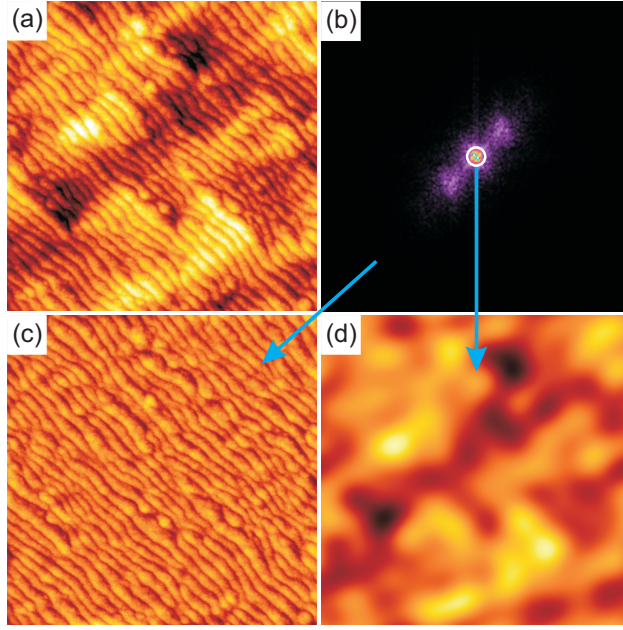


Figure 3.7.: (a) STM topograph (image size $1.2 \mu\text{m} \times 1.2 \mu\text{m}$, z-scale 9 nm) and (b) zoom into Fourier transform of (a) (limits $\pm 100 \mu\text{m}^{-1}$). The blue circle with a radius $7 \mu\text{m}^{-1}$ separates short wavelength and long wavelength components of the pattern. (c) Inverse Fourier transform of the short wavelength component of (b) (z-scale 6 nm). (d) Inverse Fourier transform of the long wavelength component of (b) (z-scale 9 nm).

Separating long and short wavelength components

To analyze the different ripple modes at $\vartheta = 63^\circ$, the long wavelength components with $1/\lambda < 7 \mu\text{m}^{-1}$ were separated from the short wavelength components with $1/\lambda > 7 \mu\text{m}^{-1}$ using a FFT filter as shown in figure 3.7. The separation was performed using the software Gwyddion [101]. Starting from an STM topograph (figure 3.7(a)), its Fourier transform is calculated (figure 3.7(b)). To separate short wavelength and long wavelength components of the pattern, within the Fourier transform a circle around the origin is drawn. The low frequency contribution inside of the circle and the high frequency contribution outside of it are back transformed separately and represented in figures 3.7(c) and (d), respectively. Thereby a clear separation of the short wavelength parallel ripple mode (wave vector of the ripple pattern parallel to the projection of the ion beam on the surface) and the long wavelength perpendicular mode is achieved. The roughness obtained for figure 3.7(c) is defined as short wavelength roughness σ_s , the one of Fig. 3.7(d) as long wavelength roughness σ_l .

Sobel filtering

Sobel filtering can be used to enhance the visibility of small details on top of large corrugations, e. g. the Si(001) dimer rows on very corrugated surfaces (figure 3.8). Convolving the kernels

$$K_x = \frac{1}{4} \begin{pmatrix} 1 & 0 & -1 \\ 2 & 0 & -2 \\ 1 & 0 & -1 \end{pmatrix}, \quad K_y = \frac{1}{4} \begin{pmatrix} 1 & 2 & 2 \\ 0 & 0 & 0 \\ -1 & -2 & -1 \end{pmatrix} \quad (3.14)$$

3.6. Kinetic Monte Carlo simulations with TRIM.SP

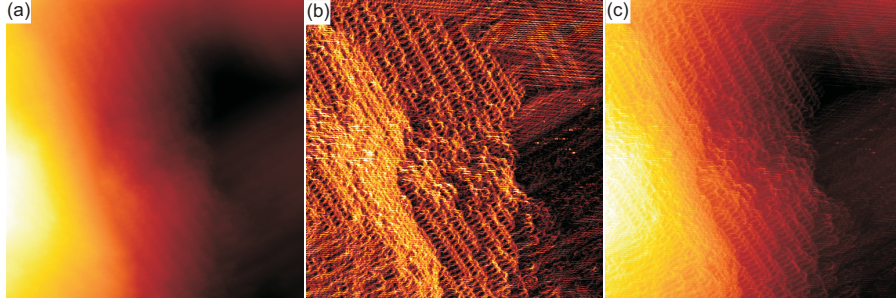


Figure 3.8.: (a) original STM image, image size $45 \text{ nm} \times 45 \text{ nm}$, z-scale 6.4 nm , (b) Sobel filtered image, (c) linear combination of both.

with the original image matrix $H = (h_{ij})$ (figure 3.8(a)) give the matrices $S_x = K_x * H$ and $S_y = K_y * H$ which contain approximations of the local slope in x and y direction respectively. The Sobel filtered image (figure 3.8(b)) is then $S = (S_{ij}) = \left(\sqrt{S_{x,ij}^2 + S_{y,ij}^2} \right)$ [35]. Adding a multiple cS of the Sobel filtered image S to the original image H enhances the visibility of small details in the combined image $H + cS$ (figure 3.8(c)) if c is chosen suitably.

3.6. Kinetic Monte Carlo simulations with TRIM.SP

TRIM.SP is a kinetic Monte Carlo simulation program for simulating ion impacts into an amorphous target [5, 41]. TRIM.SP is based on the binary collision approximation, i. e. only collisions between two particles are considered. This is a good approximation as in close collisions only one atom contributes significantly and more distant collisions can be approximated as a sequence of small angle scattering events. The binding of target atoms and projectiles to the surface is approximated by a potential step at the surface. This surface binding energy E_{SB} has to be chosen reasonably. Target atoms moving out of the target are counted as sputtered atoms when they have crossed this potential barrier. When the energy of a particle drops below the recoil cut off energy E_{RC} it will not be followed any longer.

For accurate results, the input parameters must be chosen carefully. As interaction potential the Kr-C potential [140] was chosen in accordance with Biersack and Eckstein [5]. For sputtering, a correct choice of the surface binding energy is essential. As Kr is non-reactive, the surface binding energy for Kr is set to 0. For the target atoms, the surface binding energy is larger than 0. For silicon, iron and the iron silicides the surface binding energies were taken from [96]. For the other elements and silicides the surface binding energy was calculated following the approach of Eckstein and Biersack [42]:

$$E_{\text{SB}} = N_{\text{A}}^{-1} \left(-\Delta H_{\text{f}}(\text{M}_m\text{Si}_n) + \frac{m\Delta H_{\text{s}}(\text{M}) + n\Delta H_{\text{s}}(\text{Si})}{m+n} \right) \quad (3.15)$$

where N_A is the Avogadro constant, m and n are the numbers of metal and silicon atoms in a molecule M_mSi_n respectively, ΔH_f is the enthalpy of formation of the silicide and $\Delta H_s(\text{Si}/M)$ are the enthalpies of sublimation of the pure elements. The enthalpies of sublimation were taken from [148], the enthalpies of formation for palladium silicides from [114], the enthalpy of formation of IrSi from [114] (the only iridium silicide for which ΔH_f is known), and for silicon carbide from [114]. The recoil cut-off energy E_{RC} was set to the surface binding energy E_{SB} .

4. Silicide induced patterns

The results of this chapter have been published in *Nanotechnology* [44].

Co-deposition of metal impurities during ion bombardment can yield ordered patterns even for low ion incidence angles $\vartheta < \vartheta_c$, where ϑ_c is the critical incidence, angle for pattern formation without impurities (see chapter 2.5). The pattern inducing impurities Mo, Ni, Pt, and W [31, 32, 62, 80–82, 108, 109, 121, 130, 143, 147, 149, 150] all form silicides [114]. Au, a non-silicide forming metal [114], does not induce pattern formation [62] and Cu, which only forms silicides with a large metal concentration and a very low enthalpy of formation [114], needs very high concentrations to induce pattern formation [62]. This indicates that silicide formation is necessary for pattern formation. Comparing the pattern forming abilities of metals which form silicides and metals which do not form silicides allows one to analyze the importance of silicide formation for pattern formation. By choosing pairs of metals, where the metals in each pair have similar atomic mass and one metal forms a silicide and the other metal does not, we can evaluate how important silicide formation is compared to the effect of different collision kinetics. Here we chose the pairs Ag–Pd and Pb–Ir which have a similar nuclear charge ($Z_{\text{Pd}} = 46$, and $Z_{\text{Ag}} = 47$; $Z_{\text{Ir}} = 77$, and $Z_{\text{Pb}} = 82$) and atomic mass ($m_{\text{Pd}} = 106.42 \text{ u}$, and $m_{\text{Ag}} = 107.87 \text{ u}$; $m_{\text{Ir}} = 192.22 \text{ u}$, and $m_{\text{Pb}} = 207.2 \text{ u}$) [141] which were sputter co-deposited. While Pd and Ir form silicides, Ag and Pb do not [114]. More controlled co-evaporation experiments were performed for Pd and Fe. For Fe, new data of the metal area density of an sputter co-deposition sample prepared and analyzed with STM by Sven Macko [79] will be shown.

For metal impurity induced pattern formation different models have been proposed (see chapter 2.5). Macko et al. [80] proposed that local metal flux variation at existing height fluctuations amplify these height fluctuations by differences in the erosion rate due to differences in the chemical composition. This idea has been studied analytically by Bradley [9]. Zhang et al. and Hofsäss et al. [62, 143, 147] proposed that phase separation drives the pattern formation. Norris [104] analyzed ion beam induced pattern formation driven by spinodal decomposition as phase separating mechanism. The applicability of the different models will be discussed in view of the experimental results.

4.1. Ag co-deposition

Figure 4.1 shows micrographic images of the Si surface after ion bombardment with concurrent deposition of Ag using the sputter co-deposition setup (figure 3.2(a)). The

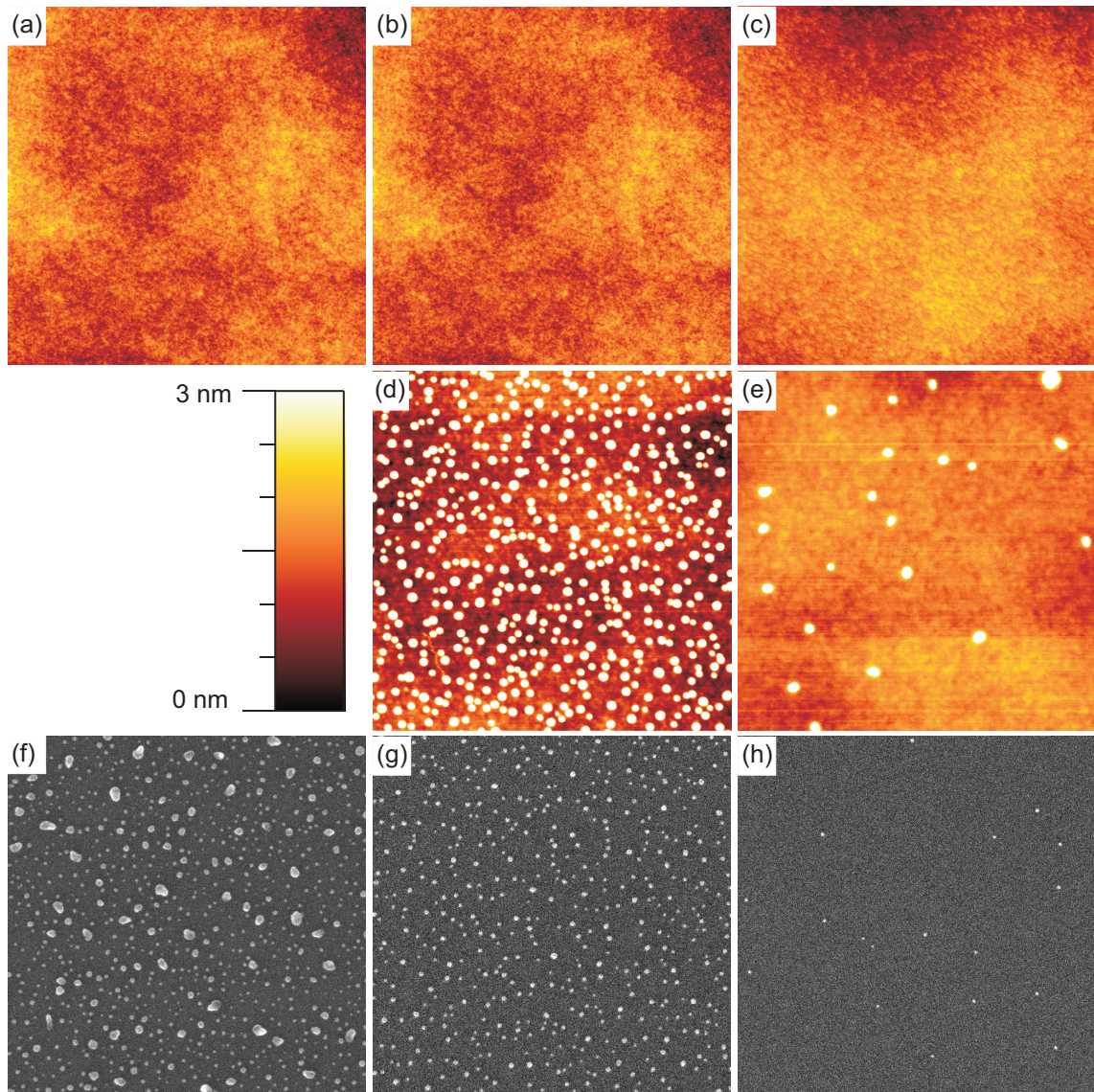


Figure 4.1.: Microscopic images after Ag sputter co-deposition: (a)–(c) in-situ STM topographs, (a) $x = 0.8$ mm, (b) $x = 1.8$ mm, (c) $x = 2.9$ mm; (d)–(e) ex-situ AFM images, (d) $x = 2$ mm, (e) $x = 3.5$ mm; (f)–(h) ex-situ SEM micrographs, (f) $x = 0.8$ mm, (g) $x = 1.8$ mm, (h) $x = 3.5$ mm. Image size is $900 \text{ nm} \times 900 \text{ nm}$ for all images. The z-scale is 3 nm for all STM and AFM topographs (a)–(e). A color scale bar is shown left to (d).

4.1. Ag co-deposition

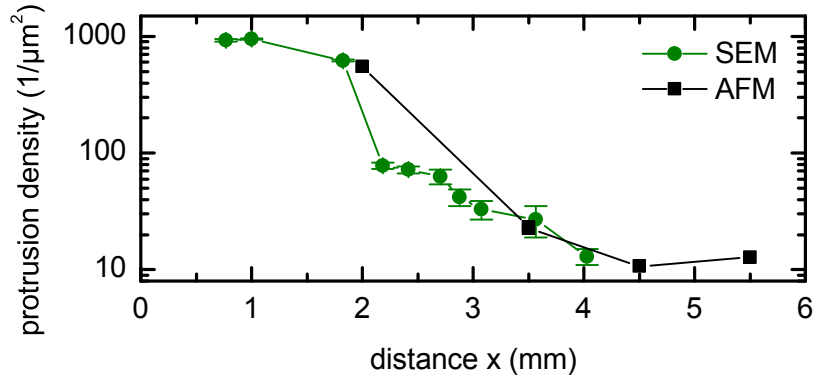


Figure 4.2.: Protrusion density vs. distance x from Ag target.

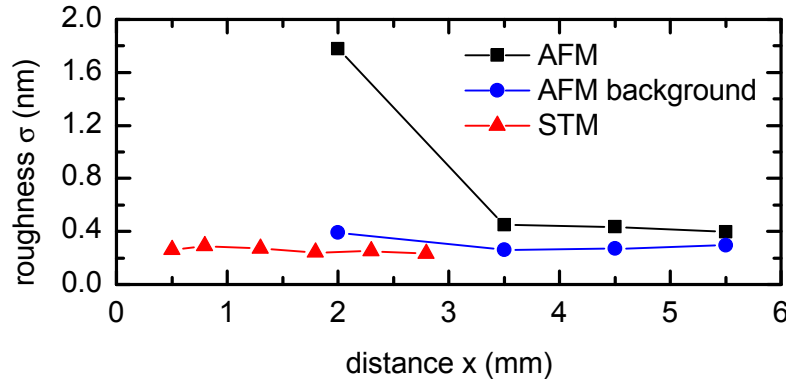


Figure 4.3.: Roughness σ after Ag sputter co-deposition determined from STM and AFM topographs as a function of distance x from the Ag target (see text).

distance x from the metal target increases from left to right and is approximately constant for each column. The rows show the different microscopy methods used: (a)–(c) in-situ STM, (d)–(e) ex-situ AFM and (f)–(h) ex-situ SEM. The in-situ STM measurements reveal a smooth and flat surface. It shows only long wavelength corrugations and is indistinguishable from the surface after ion bombardment without impurities (compare [81]).

After taking the sample out of vacuum and thus exposing it to air the surface topography changed substantially. Ex-situ AFM (figure 4.1(d)–(e)) and ex-situ SEM (figure 4.1(f)–(h)) show protrusions with a typical height of 5 nm, not visible in in-situ STM at the same distances x . The protrusion density decreases with increasing distance x as shown in figure 4.2. The SEM data shows that the size of the protrusions decreases with the distance x to the metal target. The surface roughness measured ex-situ with AFM (figure 4.3) also decreases with increasing distance x . The ex-situ measured roughness $\sigma_{\text{AFM}} = 1.8$ nm is much larger than the in-situ measured roughness $\sigma_{\text{STM}} = 0.25$ nm at $x = 2$ mm. The roughness of the background in the AFM data is approximately the same

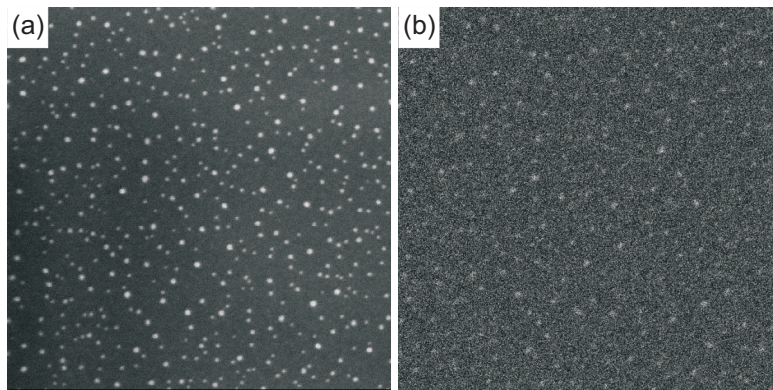


Figure 4.4.: (a) Secondary (in lens detector) and (b) backscattered electron SEM images of the same sample location. Image size $870 \text{ nm} \times 870 \text{ nm}$.

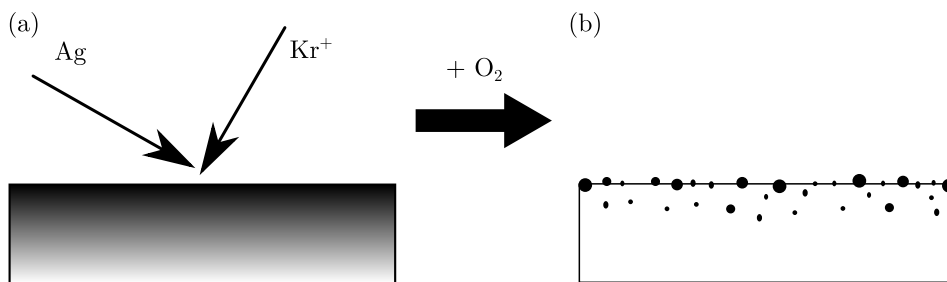


Figure 4.5.: Sketch of the Ag cluster formation

as the surface roughness measured in-situ with STM. The AFM background roughness was estimated by evaluating only regions with a height $h < 3.3 \text{ nm}$, thus excluding the protrusions. From this we can see that the increased surface roughness after exposure to air is due to the formation of the protrusions.

Figure 4.4 shows a secondary electron (a) and a backscattered electron SEM image (b) of the same location. The large protrusions in (a) appear as bright spots in the backscattered electron image (b). As the backscattering probability is increased for large nuclear charges of the substrate atoms, the bright protrusions can be assigned to Ag clusters on the surface. The Ag area density $n_{\text{Ag}} = (2.86 \pm 0.14) \times 10^{19} \text{ Ag atoms/m}^2$ is substantial, as measured with RBS at $x = 2 \text{ mm}$. The decrease of the protrusion density with increasing distance x from the target plate is consistent with the decreasing of the metal flux with the distance x .

A model for Ag cluster formation

The absence of the clusters at in-situ imaging and presence at ex-situ imaging shows that the cluster formation is connected with the exposure of the sample to air. During Ag sputter co-deposition the ion beam mixes the deposited Ag into the surface layer with a thickness of about the ion range. Ion beam mixing produces a metastable mixed phase [89] despite the fact that Ag and Si are immiscible in equilibrium [114]. The ion beam amorphizes the surface and Ag can bind to dangling Si bonds similar to adsorption of Ag on Si [74, 113]. This leads to a laterally homogeneous Ag distribution as sketched in figure 4.5(a). As the composition is uniform, no patterns form and the surface is smooth as observed in-situ.

When the sample is transferred out of the vacuum the Si surface is exposed to air. Si oxidizes with a large enthalpy of formation $-\Delta H_{\text{SiO}_2} = 911 \text{ kJ/mol}$ when exposed to O_2 [25]. As the mixing enthalpy of Ag in Si is approximately zero [114], Ag is displaced by O. Ag precipitates to the surface where it diffuses and forms clusters as sketched in figure 4.5(b). A fraction of the Ag might form clusters inside the SiO_2 matrix. Matsunami and Hosono [90] observed the formation of Ag clusters after ion implantation of Ag into SiO_2 . Consistent with the model outlined above, this implies that Ag is insoluble in SiO_2 .

The mechanism sketched above is probably also responsible for the formation of Ag clusters on top of flat ripple faces by Ag sputter co-deposition with 5 keV Xe^+ ions at an incidence angle $\vartheta = 70^\circ$ [64].

Previously, phase separation by oxidization was already reported for thin – $\approx 15 \text{ nm}$ thick – Cu_3Si films on Si by Alford et al. [1]. The implanted Cu segregates into a network of filaments at the surface and the interface between SiO_2 and Si during room temperature oxidization in air. The driving force for phase separation is the very large enthalpy of formation of SiO_2 compared to the small enthalpy of formation $-\Delta H_{\text{Cu}_{19}\text{Si}_6} = -6 \text{ kJ/mol}$ [114] of $\text{Cu}_{19}\text{Si}_6$, the Cu silicide with the largest enthalpy of formation. This large difference in enthalpy of formation is a strong driving force for phase separation. Therefore, it can not be ruled out the faint dot patterns observed ex-situ after Cu sputter co-deposition on Si reported by Hofsäss et al. are just a result of oxidization induced phase separation in air.

4.2. Pd co-deposition

The atomic mass of Pd $m_{\text{Pd}} = 106.42 \text{ u}$ and Ag $m_{\text{Ag}} = 107.87 \text{ u}$ are approximately the same. As Pd forms silicides while Ag does not, the differences in pattern formation can be attributed to the different chemical interaction with Si and are not caused by different collision kinetics. The two co-deposition methods – sputter co-deposition with ions at an incidence angle $\vartheta = 30^\circ$ and the co-evaporation with normal incident ions – were used (see chapter 3.3) for Pd co-deposition.

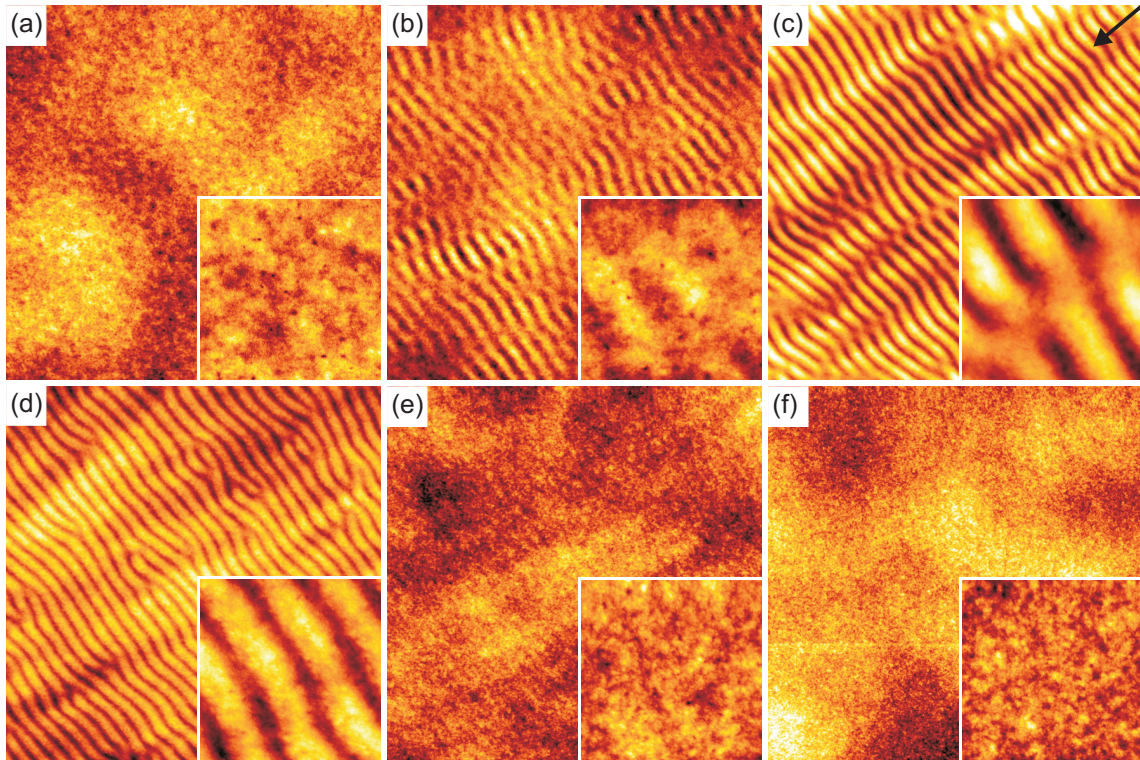


Figure 4.6.: STM topographs after Pd sputter co-deposition. (a) $x = 0.7$ mm, z-scale 2 nm; (b) $x = 0.9$ mm, z-scale 3 nm; (c) $x = 1.1$ mm, z-scale 6 nm; (d) $x = 1.6$ mm, z-scale 5 nm; (e) $x = 1.9$ mm, z-scale 2 nm; (f) $x = 2.4$ mm, z-scale 2 nm; Image size $1.2 \mu\text{m} \times 1.2 \mu\text{m}$, inset size $160 \text{ nm} \times 160 \text{ nm}$. The arrow indicates the direction of the Pd.

Pd sputter co-deposition

Pd sputter co-deposition leads to ripple pattern formation. Figure 4.6 shows in-situ STM images taken at increasing distances x . The insets show magnifications of details. The pattern depends strongly on the distance x to the Pd target plate. At $x = 0.7$ mm the surface shows shallow depressions (holes) on top of shallow long wavelength modulations (figure 4.6(a)). These depressions are very shallow with a characteristic width of ≈ 5 nm and an apparent depth of ≈ 0.8 nm. The long wavelength corrugations are also found in absence of co-deposition. The ripple pattern starts $x = 0.9$ mm where shallow ripples with short ridges are present (figure 4.6(b)). There are neighboring domains with a 180° phase shift. At the boundary of such domains the ripples vanish. Between $x = 0.9$ mm and $x = 1.1$ mm the surface transforms from the shallow ripple pattern with an amplitude of 0.8 nm into a well pronounced ripple pattern with an amplitude of 1.5 nm (figure 4.6(c)). At $x = 1.1$ mm the length of the ripple ridges is longer, but there are still domains with a 180° phase difference between neighboring domains (see inset of figure 4.6(b)).

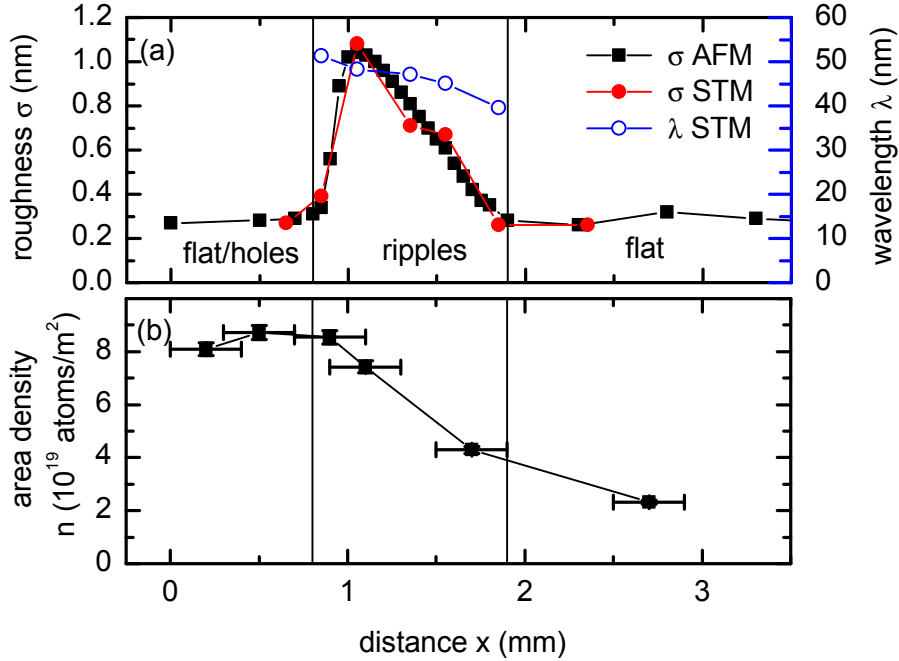


Figure 4.7.: (a) roughness σ and wavelength λ as function of distance x , (b) Pd area density n_{Pd} measured with RBS as function of distance x . The x ranges of the different surface structures are indicated by vertical lines.

With further increasing x the ripple amplitude decreases. Figure 4.6(d) is an STM topograph taken at $x = 1.6$ mm. At $x = 1.9$ mm the ripple pattern is almost vanished (figure 4.6(e)). The ripples are only small modulations with ≈ 0.2 nm amplitude on top of a long wavelength background with a corrugation of ≈ 0.4 nm. Further away no pattern is visible. There, the surface is indistinguishable from a surface after ion bombardment without co-deposition.

In figure 4.7(a) the roughness of the surface as a function of the distance x is plotted. The roughness measured in situ with STM (red circles) and ex-situ with AFM (black squares) agree quantitatively. Near the Pd target the surface remains flat with the holes/depressions shown in figure 4.6(a) for $x < 0.8$ mm. The pattern formation sets on at the critical distance $x_c = 0.8$ mm. The on-set of pattern formation is accompanied by a strong increase in surface roughness. The maximum roughness is $\sigma = 1.1$ nm at $x = 1.1$ mm. In the range from $x = 1.1$ mm to $x = 1.9$ mm the roughness decreases linearly with x . Beyond $x = 1.9$ mm the surface is flat with $\sigma = 0.3$ nm. The ripple wavelength is also plotted in figure 4.7(a). The ripple wavelength decreases monotonically from $\lambda = 5$ nm at $x = 0.9$ mm to $\lambda = 40$ nm at $x = 1.9$ mm.

Figure 4.7(b) shows the Pd area density n_{Pd} measured with RBS as function of x . The Pd area density has a broad maximum in the range $x = 0.5$ mm to $x = 0.9$ mm

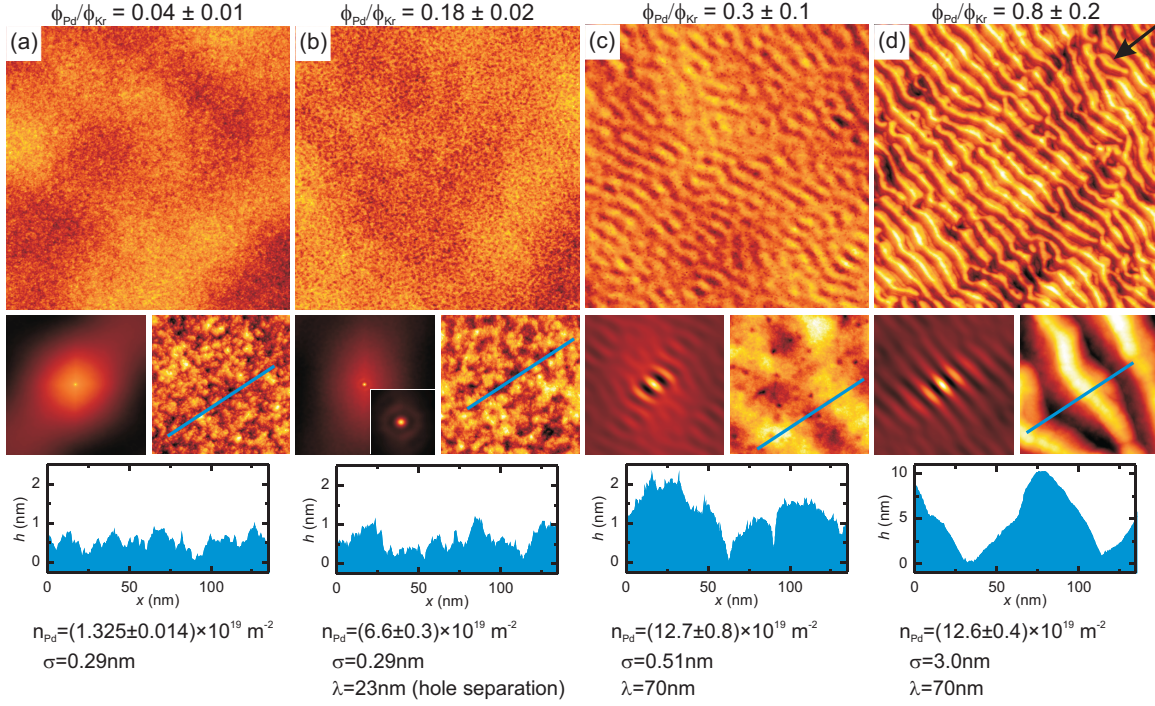


Figure 4.8.: (a)–(d) Pd co-evaporation experiments with flux ratios $\Phi_{\text{Pd}}/\Phi_{\text{Kr}}$ as indicated, increasing from left to right. The size of the large scale STM topographs is $1.2 \mu\text{m} \times 1.2 \mu\text{m}$, the auto-correlations (left) have a range of $\pm 300 \text{ nm}$ (range in the inset of (b) is $\pm 50 \text{ nm}$) and the size of the zoomed STM topographs (right) is $180 \text{ nm} \times 180 \text{ nm}$. Height profiles are shown along the lines in the zoomed STM topographs. Additionally, Pd area density n_{Pd} , roughness σ and wavelength λ are specified for each experiment. The z-scales are (a) 3 nm, (b) 3 nm, (c) 5 nm, and (d) 16 nm. The projection of the Pd flux direction on the surface is indicated by the black arrow in (d).

with $n_{\text{Pd}} = (8.5 \pm 0.3) \times 10^{19} \text{ Pd atoms/m}^2$ and decreases slowly for larger x . The x -dependence of the Pd area density n_{Pd} can be considered to be a good approximation of the x -dependence of the Pd flux Φ_{Pd} in the late stage of the experiment. As discussed in chapter 3.3, Φ_{Pd} is effected by the complicated cross-talk between substrate and target. The x -dependence of n_{Pd} may be effected by the surface morphology. Due to the small surface slopes ($\lesssim 8^\circ$), the morphology effects are not important here.

Pd co-evaporation

Pd co-evaporation (figure 3.2(b)) is a more controlled approach, which provides a homogeneous Pd flux from the same direction over the whole sample. The ion beam is incident normal to the surface and the incidence angle of the Pd atoms is $\vartheta_{\text{Pd}} = 60^\circ$. Figure 4.8 shows an overview of the Pd co-evaporation experiments. Each column shows the results of a specific Pd to Kr^+ flux ratio $\Phi_{\text{Pd}}/\Phi_{\text{Kr}}$. For each flux ratio $\Phi_{\text{Pd}}/\Phi_{\text{Kr}}$ a

4.2. Pd co-deposition

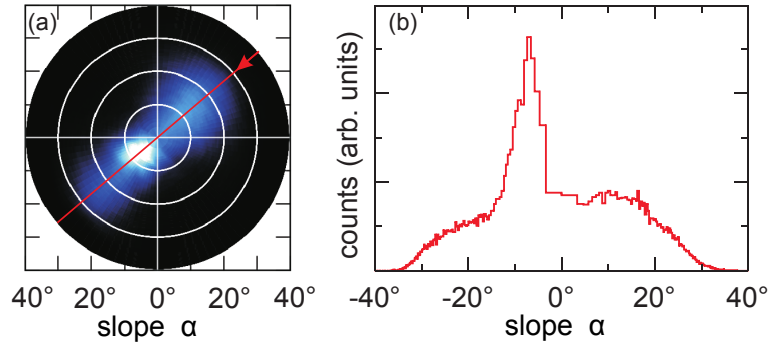


Figure 4.9.: (a) Polar plot of surface slope angles after Pd co-evaporation with $\Phi_{\text{Pd}}/\Phi_{\text{Kr}} = 0.8$. (b) Cut of (a) along the Pd flux direction. Positive slope angles α refer to the side facing the Pd flux, negative ones refer to the opposite side. The arrow in (a) shows the direction of the Pd flux.

large scale STM image, the 2d auto-correlation, a magnified image of surface details, and a line profile along the line in the detail image are shown. In addition, the analytic results are stated for each experiment: the Pd area density n_{Pd} , the roughness σ , and the wavelength λ . The arrow in figure 4.8(d) indicates the projection of the Pd beam onto the sample plane. With increasing the flux ratio from $\Phi_{\text{Pd}}/\Phi_{\text{Kr}} = 0.04$ to $\Phi_{\text{Pd}}/\Phi_{\text{Kr}} = 0.8$ the surface morphology changes from a flat surface to a surface with a pronounced ripple pattern. The surface at the lowest flux ratio (figure 4.8(a)) has a grainy fine structure on top of long wavelength modulations with a low roughness of $\sigma = 0.29$ nm. The surface is very similar to a surface after ion bombardment without metal co-deposition. The flux ratio $\phi_{\text{Pd}}/\Phi_{\text{Kr}} = 0.18$ (figure 4.8(b)) yields a surface with small holes of characteristic depth ≈ 0.5 nm on top of long wavelength modulation. The characteristic separation of the holes is 23 nm giving rise to the ring in the autocorrelation function (inset in figure 4.8(b)). The surface roughness is still $\sigma = 0.29$ nm. Ripple patterns appear at a flux ratio $\Phi_{\text{Pd}}/\Phi_{\text{Kr}} = 0.3$ (figure 4.8(c)). These ripple patterns are weakly ordered with a wave vector parallel to the Pd flux direction. The wavelength is $\lambda = 70$ nm and the surface roughness $\sigma = 0.5$ nm. On top of the ripples small holes are visible with a depth of up to 1 nm – the line profile shows a cut through such a hole. At the high flux ratio $\Phi_{\text{Pd}}/\Phi_{\text{Kr}} = 0.8$ a pronounced and ordered ripple pattern develops. The corrugation of the ripples is ≈ 10 nm with a wavelength of $\lambda = 70$ nm. The shape of the ripples is asymmetric as shown in the profile of figure 4.8(d). The side facing the Pd flux has a smooth slope while the opposite side has two characteristic slopes: a smaller slope close to the valley and a larger slope near the ridge.

Figure 4.9 shows the distribution of surface slope angles α of the large topography image in figure 4.8(d) to analyze the slopes of the ripple in more detail. The polar plot of the distribution is shown in figure 4.9(a). The distribution has a sharp maximum for small slope angles at the side opposite to the Pd flux indicated by the arrow. The cut along the direction of the Pd flux is shown in figure 4.9(b). The side facing the Pd flux

has a broad slope angle distribution around $\alpha \approx 15^\circ$. The slope angle distribution on the opposite side displays a sharp maximum at $\alpha = 7^\circ$ by the facets near the ripple valleys. The steep region near the ridges give rise to the broad shoulder between 15° and 30° .

Surprisingly, the Pd area density is not proportional to the flux ratio $\Phi_{\text{Pd}}/\Phi_{\text{Kr}}$ for the entire range investigated. In fact, for $\Phi_{\text{Pd}}/\Phi_{\text{Kr}} = 0.3$ and $\Phi_{\text{Pd}}/\Phi_{\text{Kr}} = 0.8$ the Pd area densities are identical within the limits of error, although the resulting morphologies differ substantially, e.g. the roughness by a factor of six [compare figure 4.8(c) and (d)]. This observation implies that the steady state impurity concentration does not allow one to uniquely characterize or classify morphologies. Obviously, for very different impurity fluxes qualitatively different morphological evolutions take place that accidentally may result in identical steady state impurity concentrations.

The spatial distribution of Pd and the structure of the ion beam modified surface layer were analyzed by cross-sectional TEM for the sample with $\Phi_{\text{Pd}}/\Phi_{\text{Kr}} = 0.8$, as represented by the STM topographs in figure 4.8(d). The cross-sectional bright-field TEM overview image in figure 4.10(a) displays at the bottom the crystalline Si (dark) and above the ion beam amorphized layer with a thickness of 8 nm to 11 nm (bright) which includes a Pd enriched layer at the top (dark). It is obvious that the Pd enrichment of the amorphous layer is nonuniform. It is highest in an approx. 4 nm thick layer at the top of the ripple and the mountainside facing the Pd beam. The Pd enriched layer is thinner or even absent in the ripple valleys. The thickness of the entire amorphized layer is thinner, where the Pd enriched layer is thicker. This is a consequence of the larger stopping power of the Pd enriched matrix. The high-resolution TEM image in figure 4.10(b) shows the crystalline structure of the Si substrate, the ion beam amorphized Si layer and the Pd rich layer on top in more detail. The Pd rich layer occasionally contains crystalline inclusions of a few nm in size. Figure 4.10(c) is a magnification of such an inclusion. Using the JEMS software package [128], it is identified as a Pd_3Si crystallite in $[212]$ zone axis geometry by comparing its Fourier transform shown in figure 9(d) with simulated spot diffraction patterns of various Pd silicides, in particular Pd_3Si [figure 9(e)]. Based on our observation, we conclude that the Pd enriched layer is Pd_mSi with m in the range of 2–3. Pd_2Si and Pd_3Si are the two Pd-silicides with the highest Si content stable at low temperatures. The energy filtered TEM image in figure 4.10(f) of the same location as shown figure 4.10(c) shows the brighter contrast, the higher the Pd concentration. It is consistent with the interpretation of the bright-field image shown in figure 4.10(a) and the high-resolution TEM image in figure 4.10(b).

4.3. Pb co-deposition

Pb was deposited with the sputter co-deposition setup (see chapter 3.3) during ion bombardment. Figure 4.11 shows the resulting morphology at different positions on the sample. Clearly no pattern forms and the surface stays flat with a roughness $\sigma < 0.2$ nm.

4.3. Pb co-deposition

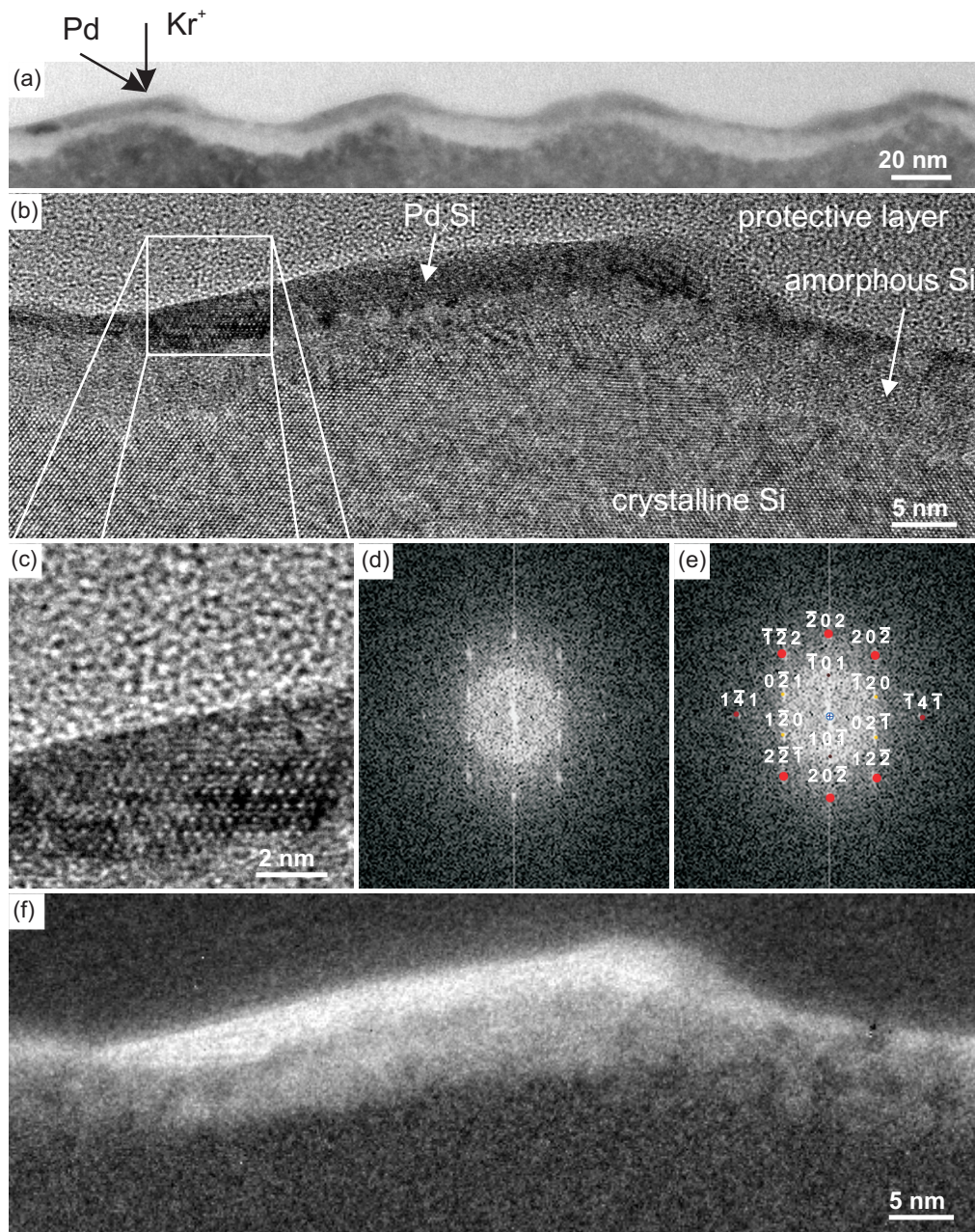


Figure 4.10.: (a) Cross-sectional TEM image of co-evaporation sample with flux ratio $\Phi_{\text{Pd}}/\Phi_{\text{Kr}} = 0.8$, (b) high-resolution TEM image, (c) detail of (b) showing crystalline Pd_3Si , (d) Fourier transform of (c) with contrast enhanced, (e) indexed Fourier transform (see text), and (f) energy-filtered TEM image showing Pd distribution. Pd is concentrated in the bright areas.

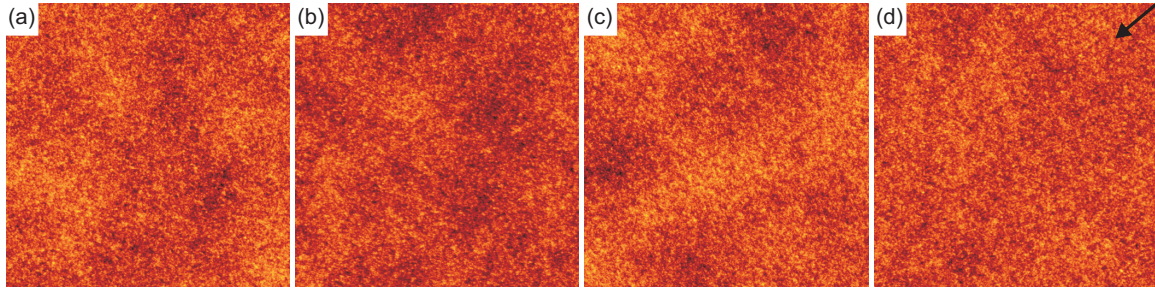


Figure 4.11.: In-situ STM topographs after Pb sputter co-deposition. x increases from left to right: (a) $x = 1.0$ mm, (b) $x = 1.5$ mm, (c) $x = 2.0$ mm, (d) $x = 2.5$ mm, The arrow indicates the direction of the Pb flux. The image size is always $1.2 \mu\text{m} \times 1.2 \mu\text{m}$ and the z-scale 2 nm.

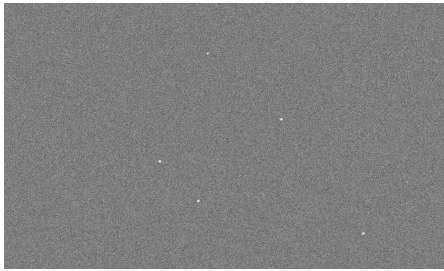


Figure 4.12.: Ex-situ secondary electron SEM image ($5 \mu\text{m} \times 3 \mu\text{m}$) of the Pb sputter co-deposition sample at $x \approx 2$ mm

The morphology is indistinguishable from the one without co-deposition during ion bombardment. During ion bombardment Pb is mixed into the amorphous near surface layer analogous to Ag co-deposition (chapter 4.1) and Pb attaches to dangling Si bonds. Ex-situ SEM (figure 4.12) shows the same morphology. As PbO is soluble in SiO_2 [127] no phase separation takes place upon oxidization and no Pb or PbO clusters form.

4.4. Ir co-deposition

For Ir co-deposition the sputter co-deposition setup (see chapter 3.3) has been employed. Ir sputter co-deposition produces a large variety of patterns depending on the distance x to the Ir target in contrast to Pb sputter co-deposition. The surface morphology as a function of x is shown with in-situ STM topographs in figure 4.13 and ex-situ AFM topographs in figure 4.14. The roughness σ measured with in-situ STM and ex-situ AFM, and the wavelength λ are shown in figure 4.15. For small x the surface is flat with nanometer sized holes (figure 4.13(a)). At $x_c = 1.2$ mm a sharp transition from a flat surface to ripple pattern occurs (compare also with the roughness shown in figure 4.15). At this transition ($x = 1.3$ mm) islands of high (> 10 nm) ripples emerge on a background of lower (< 6 nm) ripples (figures 4.13(b) and 4.14(a)) resembling the “pillbugs” observed by Macko et al. [80]. The ripple pattern after this transition has a very high amplitude > 20 nm which is too corrugated to be imaged artifact free with STM, so only AFM images (figure 4.14(b) and (c)) are shown. For distances larger than the distance of

4.4. Ir co-deposition

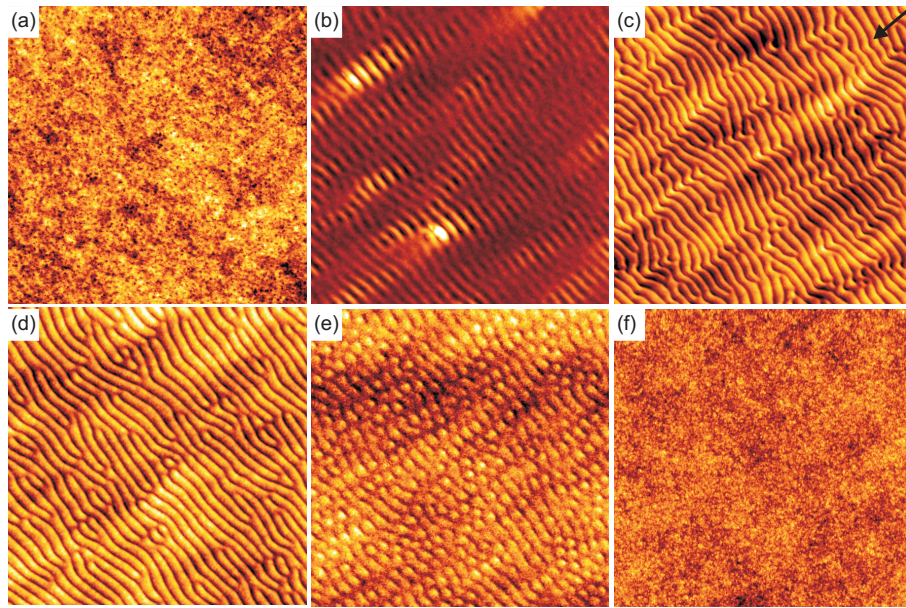


Figure 4.13.: In-situ STM topographs ($1.4 \mu\text{m} \times 1.4 \mu\text{m}$) after Ir sputter co-deposition: (a) $x = 1.0$ mm z-scale 1.5 nm (b) $x = 1.3$ mm z-scale 10 nm (c) $x = 2.5$ mm z-scale 8 nm (d) $x = 3.5$ mm z-scale 4 nm (e) $x = 4.3$ mm z-scale 3 nm (f) $x = 4.5$ mm z-scale 1.5 nm

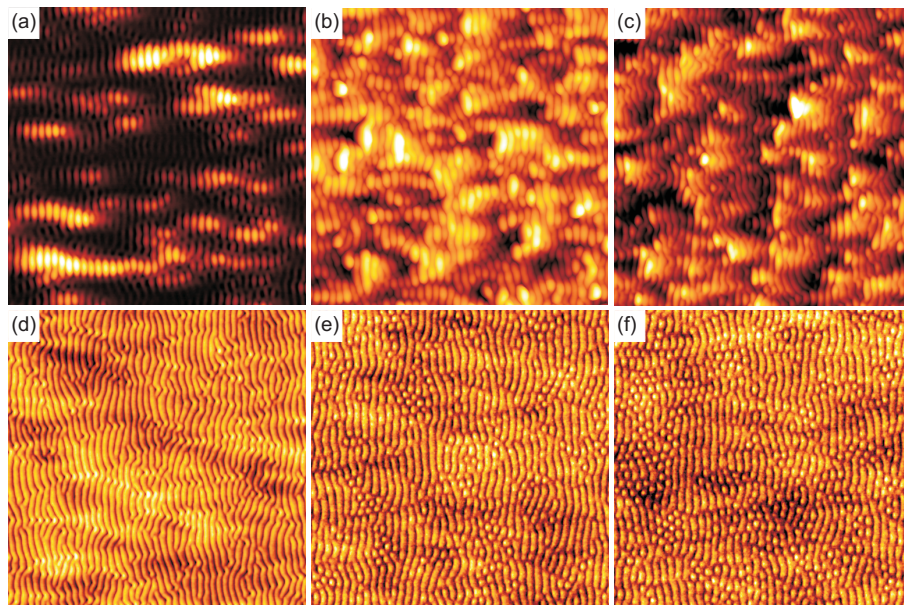


Figure 4.14.: Ex-situ AFM images ($2 \mu\text{m} \times 2 \mu\text{m}$) of the Ir sputter co-deposition sample: (a) $x = 1.3$ mm z-scale 50 nm (b) $x = 1.4$ mm z-scale 80 nm (c) $x = 2.3$ mm z-scale 40 nm (d) $x = 2.6$ mm z-scale 8.5 nm (e) $x = 3.7$ mm z-scale 3 nm (f) $x = 3.8$ mm z-scale 2.5 nm

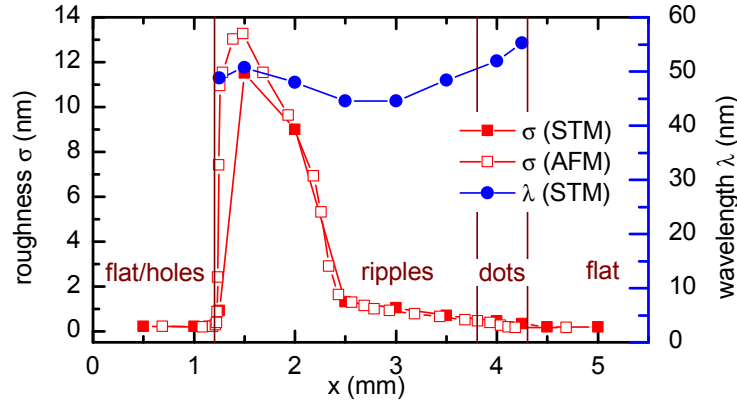


Figure 4.15.: Roughness σ and wavelength λ for Ir sputter co-deposition. The vertical lines separate the x ranges of the different pattern types.

maximum roughness $x_{\max} = 1.5$ mm (figure 4.14(b)) the roughness decreases strongly with increasing x . This high amplitude ripple region is characterized by the peak in the roughness curve of figure 4.15. After the high ripple range well ordered ripples with smaller amplitudes (figure 4.13(c), 4.14(d)) develop in the range $x = 2.5$ mm to $x = 3.7$ mm. The surface roughness decreases monotonically with increasing distance x . Near the end of the ripple range at $x = 3.7$ mm (figure 4.14(e)) the defects in the ripples increase and the ripple ridges separate into rows of dots. At $x = 3.8$ mm (figure 4.14(f)) the surface is covered mainly with rows of dots with some small ripple domains. In the dot range $x = 3.8$ mm to $x = 4.3$ mm the surface is covered with rows of dots (figure 4.13(e)). For $x \geq 4.5$ mm the surface is patternless and flat as without metal co-deposition.

The wavelength λ depends on the distance x (figure 4.15). It is in the range between $\lambda = 45$ nm and $\lambda = 55$ nm. There is a local maximum of the wavelength in the high amplitude ripple region at the distance $x_{\max} = 1.5$ mm of maximum roughness. For distances $x \geq 2.5$ mm the wavelength increases monotonically with x from $\lambda = 45$ nm to $\lambda = 55$ nm at $x = 4.3$ mm before the dot patterns vanishes.

4.5. Fe co-deposition

For comparing Pd and Ir co-deposition with the Fe co-deposition results by Macko et al. [79–82] new data on Fe co-deposition is presented here. The Fe area density n_{Fe} as function of the distance x to the steel target has been measured with RBS on the sputter co-deposition sample prepared at 140 K from the study presented in reference [80] and the PhD thesis of Sven Macko [79]. In addition steel co-evaporation experiments have been performed in the geometry (see chapter 3.3) used for Pd co-evaporation.

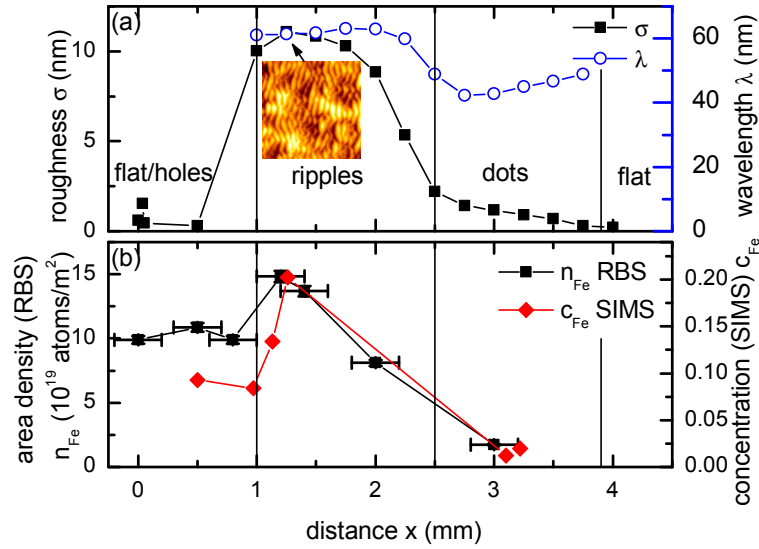


Figure 4.16.: (a) Roughness σ , wavelength or characteristic dot spacing λ as well as (b) Fe concentration c_{Fe} estimated by SIMS for a 300 K Fe sputter co-deposition sample. Data for σ and c_{Fe} taken from [79, 81]. For comparison in (b) also the Fe area density n_{Fe} measured by RBS after Fe sputter co-deposition at 140 K is plotted. The inset in (a) is a $1 \mu\text{m} \times 1 \mu\text{m}$ AFM image (z -scale 60 nm) taken at $x \approx 1.2$ mm.

Fe sputter co-deposition

Figure 4.16 shows the quantitative analysis – roughness σ , wavelength λ , and the Fe concentration c_{Fe} estimated with secondary ion mass spectroscopy (SIMS) – of the Fe sputter co-deposition sample bombarded at 300 K taken from references [79, 81].¹ The pattern evolution is similar to Ir sputter co-deposition (chapter 4.4). The sequence of morphologies with increasing x is the same: Near the target plate, there is a flat region with nanometer sized shallow holes which transforms abruptly at $x_c = 1$ mm into a rough ripple pattern with a roughness $\sigma \approx 10$ nm. Further away the ripple amplitude reduces and the ripple pattern transforms into a dot pattern which vanishes for $x > 4$ mm. The wavelength is in the range $\lambda = 42$ nm to $\lambda = 63$ nm, similar to Ir (figure 4.15) and Pd (figure 4.7(a)). The x dependence of the wavelength is qualitatively similar to Ir (figure 4.15): The wavelength has a maximum in the high amplitude ripple range, then decreases until the end of the high amplitude ripple range and finally increases until the end of the dot range.

Figure 4.16(b) shows the x dependence of the Fe area n_{Fe} density measured with RBS at the 140 K sample. For comparison the Fe concentration c_{Fe} measured with SIMS is also plotted. Note that the RBS data was measured on a different sample prepared

¹For topographic images see references [79, 81]

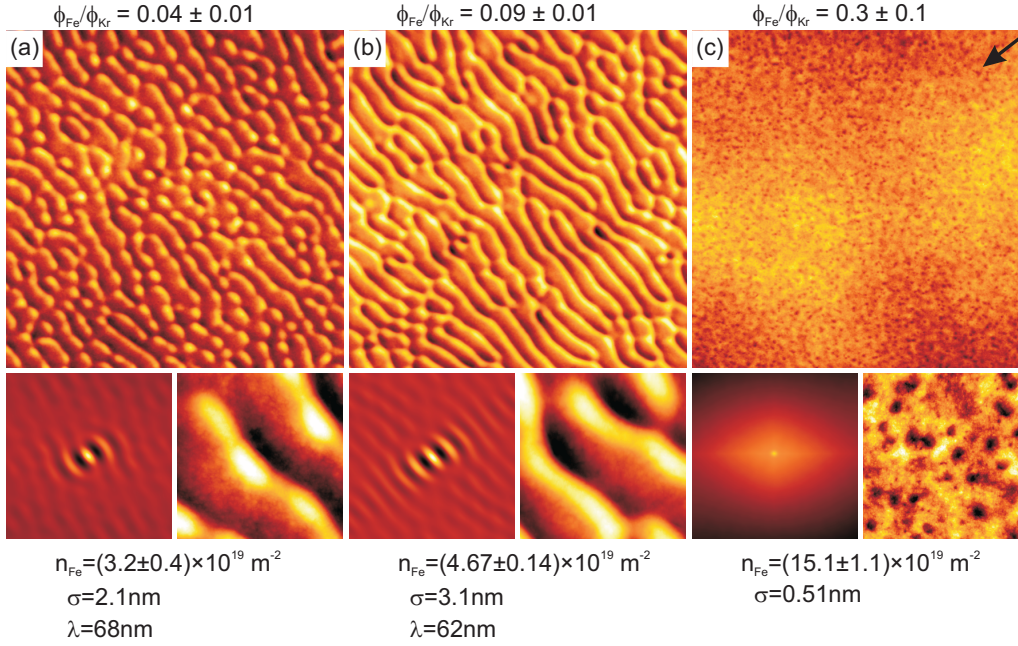


Figure 4.17.: STM topographs and autocorrelation for Fe co-evaporation experiments. For each experiment characterized by the flux ratio $\Phi_{\text{Fe}}/\Phi_{\text{Kr}}$ a large scale STM topograph of size $1.2 \mu\text{m} \times 1.2 \mu\text{m}$, the corresponding auto-correlation using a range of size $\pm 300 \text{ nm}$, and a zoomed STM topograph of size $180 \text{ nm} \times 180 \text{ nm}$ are shown. Additionally, Fe area density n_{Fe} , roughness σ and wavelength λ are specified. The z-scales are (a) 14 nm, (b) 19 nm, and (c) 4 nm. The arrow in (c) indicates the projection of the Fe flux direction onto the surface.

identically, except for the largely irrelevant temperature of ion bombardment (see [80] for details). With the onset of pattern formation at x_c the Fe area density n_{Fe} (RBS) increases by 50% which is less pronounced than the increase of the Fe concentration c_{Fe} (SIMS) but in qualitative agreement. This increase at x_c is most likely a secondary effect of the evolving ripple morphology and not related to the x dependence of the Fe flux Φ_{Fe} . The increased n_{Fe} has its origin in the reduction of Fe sputtering due to steep slopes and will be discussed later (see page 55 in chapter 4.6). Zhang et al. [143] conducted recently a Fe sputter co-deposition experiment under similar conditions, where the authors did not find a rise of n_{Fe} at $x = x_c$, but that n_{Fe} monotonically decreases with increasing x . Besides slight differences in geometry, also the inferior spatial RBS resolution (1 mm beam diameter compared to 0.2 mm beam diameter here) might have smeared out this effect.

Fe co-evaporation

To connect the Pd co-evaporation experiment with previous Fe co-deposition experiments [79, 80] conducted in a different co-evaporation geometry and to obtain additional insight

4.5. Fe co-deposition

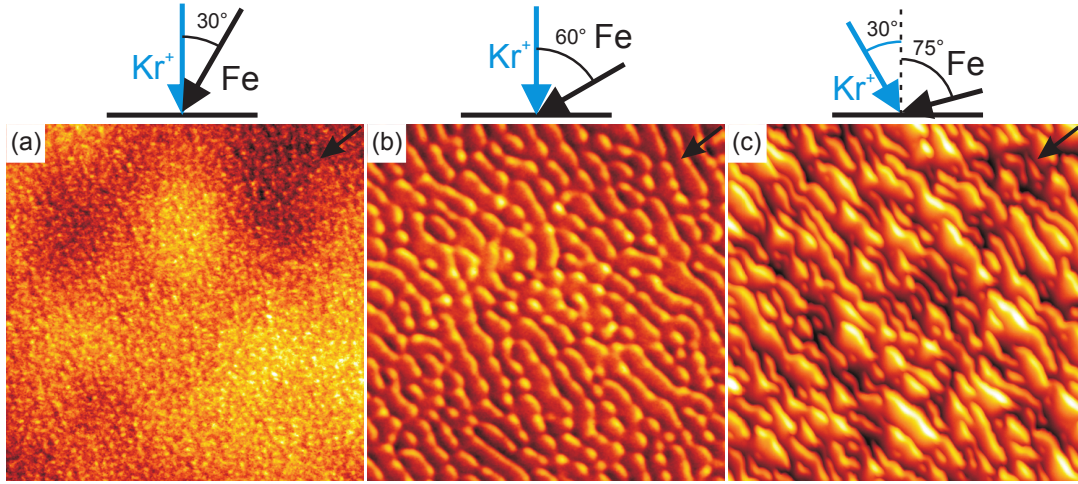


Figure 4.18.: Dependence of pattern formation on angle α between ion beam and Fe flux. (a) $\alpha = 30^\circ$, $\Phi_{\text{Fe}}/\Phi_{\text{Kr}} = 0.05$, z-scale 3 nm, (b) $\alpha = 60^\circ$, $\Phi_{\text{Fe}}/\Phi_{\text{Kr}} = 0.04$, z-scale 14 nm, and (c) $\alpha = 105^\circ$, $\Phi_{\text{Fe}}/\Phi_{\text{Kr}} = 0.04$, z-scale 50 nm. STM image size $1.2 \mu\text{m} \times 1.2 \mu\text{m}$. The arrows indicate the Fe direction. The data of (a) and (c) is taken from [79].

into the pattern formation mechanism, we co-evaporated Fe in the same geometry (see figure 3.2(b) in chapter 3.3) as used for Pd. Figure 4.17 shows the results of the Fe co-evaporation experiments. A flux ratio of $\Phi_{\text{Fe}}/\Phi_{\text{Kr}} = 0.04$ is already enough to yield a pattern which is in the transition from a dot to a ripple pattern (figure 4.17(a)). The dots align in rows. At a higher flux ratio $\Phi_{\text{Fe}}/\Phi_{\text{Kr}} = 0.09$ the morphology is a pronounced ripple pattern (figure 4.17(b)). In both cases the structures have asymmetric profiles in direction of the ion beam: the side facing the Fe flux is steeper than the opposite side. For the highest flux ratio $\Phi_{\text{Fe}}/\Phi_{\text{Kr}} = 0.3$ the surface remains flat again with $\sigma = 0.5 \text{ nm}$ slightly larger but comparable to the situation without co-deposition. The surface morphology displays nanometer holes on a long wavelength background. This is remarkable considering that $n_{\text{Fe}} = 15 \times 10^{19} \text{ Fe atoms/m}^2$ is the same Fe area density as measured at $x = 1.2 \text{ mm}$ for Fe sputter co-deposition where this is the position of the most pronounced ripples with corrugations of 50 nm to 100 nm (compare figure 4.16).

Compared with Pd co-evaporation (see chapter 4.2) the flux ratios required for formation of patterns of similar amplitude are an order of magnitude lower for Fe co-evaporation than for Pd co-evaporation (compare figure 4.8(d) with figure 4.17(b)). This indicates that Pd is a worse pattern former than Fe, which will be discussed in chapter 4.6.

Figure 4.18 shows the dependence of the pattern on the angle α between ion beam and Fe flux for a flux ratio $\Phi_{\text{Fe}}/\Phi_{\text{Kr}} \approx 0.04$. In figure 4.18(a) with $\alpha = 30^\circ$ no regular pattern evolves. The surface is just grainy on top of a long wavelength background and the roughness $\sigma = 0.4 \text{ nm}$ is as low as in the absence of metal impurities. Increasing α to 60° (figure 4.18(b)) leads to a pattern in transition between dots and ripples. The pattern is most pronounced for $\alpha = 105^\circ$ (figure 4.18(c)). The roughness is $\sigma = 9.4 \text{ nm}$. The flux ratio $\Phi_{\text{Fe}}/\Phi_{\text{Kr}} = 0.04$ of the experiments forming patterns (figures 4.18(b) and (c)) is

4.6. Discussion

Table 4.1.: Densities n , total sputtering yields Y , partial Si sputtering yields Y_{Si} , partial metal ($M = \text{Pd, Fe, Ir, C}$) sputtering yields Y_{M} , total erosion rates $\rho = Y/n$, partial Si erosion rates $\rho_{\text{Si}} = Y_{\text{Si}}/n$ calculated with TRIM.SP.

	$\vartheta = 0^\circ$						$\vartheta = 30^\circ$					
	n (atoms/nm ³)	Y	Y_{Si}	Y_{M}	ρ	ρ_{Si}	Y	Y_{Si}	Y_{M}	ρ	ρ_{Si}	
		(atoms/ion)			(10 ⁻³ nm ³ /ion)		(atoms/ion)			(10 ⁻³ nm ³ /ion)		
Pd	68.0	3.61	—	3.61	53.1	—	4.73	—	4.73	69.5	—	
Pd ₃ Si	70.2	2.45	0.73	1.72	34.9	10.3	3.47	1.01	2.46	49.5	14.4	
Pd ₂ Si	71.7	2.24	0.88	1.36	31.2	12.3	3.26	1.25	2.01	45.5	17.4	
Fe	84.8	2.38	—	2.38	28.1	—	3.54	—	3.54	41.8	—	
Fe ₃ Si	88.8	1.78	0.51	1.27	20.1	5.7	2.77	0.77	2.00	31.2	8.7	
FeSi	89.0	1.49	0.84	0.65	16.8	9.4	2.40	1.31	1.09	27.0	14.8	
FeSi ₂	79.8	1.40	1.02	0.38	17.5	12.7	2.18	1.56	0.62	27.4	19.6	
IrSi	71.3	1.79	1.10	0.69	25.1	15.4	2.55	1.53	1.03	35.8	21.4	
SiC	96.6	0.51	0.20	0.31	5.2	2.1	0.98	0.43	0.55	10.2	4.5	
Si	50.0	1.07	1.07	—	21.4	21.4	1.76	1.76	—	35.3	25.3	

form or not.

Observations (a), (b) and (c) agree with the finding of Hosäss et al. [62].

Why silicide formation is essential for pattern formation will be discussed later. Here we will only discuss the effect of sputtering yield differences due to silicide formation. The mechanisms proposed for pattern formation with metal co-deposition by Zhang, Brötzmann, and Hofsäss [147] and Macko et al. [80] both emphasize the importance of the different erosion rates of areas of different composition irrespective of the initial pattern forming steps. In both models the difference in erosion rates for different surface compositions amplifies the corrugation and thus produces the pattern. In table 4.1 the partial Y_{M} , Y_{Si} and total Y sputtering yields of silicon, silicides, and metals determined with TRIM.SP for the incidence angles $\vartheta = 0^\circ$ and $\vartheta = 30^\circ$ are summarized.

Let us assume first a situation in which the surface is composed of pure silicon and silicide patches *without* additional metal supply. In this situation the total erosion rate $\rho = Y/n$ (see table 4.1) determines which patches are eroded faster. Depending on the silicide either the silicon or silicide patches would be eroded faster. Especially palladium silicide patches would be eroded faster than silicon patches, despite the fact that we found palladium silicide near the ridges (figure 4.10 in chapter 4.2). However, one has to consider a dynamic equilibrium between sputtered metal and replenished metal such that the silicide is maintained. The mechanisms of replenishment will be discussed later. In this situation the partial Si erosion rate $\rho_{\text{Si}} = Y_{\text{Si}}/n$ determines the speed of erosion of the different patches. The partial Si erosion rate is lower for all silicides compared to pure silicon. From this model the silicides are expected near the ridges of the ripples or peaks of the dots. This has been found experimentally for Fe [80, 147], Mo [62] and Pd (compare figure 4.10 in chapter 4.2). Silicide formation increases the surface binding energy E_{SB} by $-\Delta H_{\text{f}}/N_{\text{A}}$. This effect reduces Y_{Si} up to 10% compared to a target of

same composition without taking the increase of E_{SB} into account.

Even for Si-rich silicides the partial metal sputtering yields Y_M are substantial (compare table 4.1). Therefore, either efficient material supply by diffusion or by geometrical effects are required for reaching a stationary composition close to FeSi_2 or IrSi_3 with a flux ratio of $\Phi_M/\Phi_{\text{Si}} \approx 0.1$. Such a geometrical effect may consist in facet formation that enhances the local impurity flux and reduces the local metal sputtering yield. It is also obvious from table 4.1 that the much higher Y_M for metal rich silicides, e.g. Pd_2Si , makes a much larger supply of metal necessary, as observed experimentally.

Mechanism of pattern formation

First we will discuss whether initial phase separation or height fluctuations or both of them trigger the pattern formation. For details of both models see chapter 2.5.

Zhang, Brötzmann, and Hofsäss [147] proposed that initial phase separation of the metal rich layer triggers the pattern formation. The near surface layer decomposes into metal enriched patches and metal depleted silicon patches. The strongest argument for the relevance of phase separation for pattern formation is an indirect argument given by the results of the Fe co-evaporation (chapter 4.5). While for the flux ratios $\Phi_{\text{Fe}}/\Phi_{\text{Kr}} = 0.04$ and $\Phi_{\text{Fe}}/\Phi_{\text{Kr}} = 0.09$ dot and ripple patterns evolve, for the high flux ratio $\Phi_{\text{Fe}}/\Phi_{\text{Kr}} = 0.3$ no pattern develops (figure 4.17). This behavior can be explained easily by assuming that phase separation is the mechanism of pattern formation: If the surface composition is close to a stoichiometric silicide, e.g. FeSi_2 , there is no driving force for phase separation into metal enriched and metal depleted patches (compare chapter 2.2). Small concentration fluctuations increase the free energy of the system and are driven back by ion beam mixing.

In the model of Macko et al. [80] where height fluctuations induce composition fluctuations (see chapter 2.5) for oblique metal deposition it is hard to understand how this could destabilize the surface for the flux ratios $\Phi_{\text{Fe}}/\Phi_{\text{Kr}} = 0.04$ and $\Phi_{\text{Fe}}/\Phi_{\text{Kr}} = 0.09$ but not for the higher flux ratio $\Phi_{\text{Fe}}/\Phi_{\text{Kr}} = 0.3$. The flank of an elevation exposed to Fe would receive a higher Fe flux which would reduce the partial Si erosion rate and thus amplify the height fluctuation. A damping of the fluctuation for higher metal fluxes is only possible by making special assumptions on the variation of partial sputtering yields with composition.

The model proposed by Macko et al. [80] where high fluctuations induce composition modulations can easily explain the dependence of the pattern formation on the angle α between ion beam and metal flux (figure 4.18). The flux ratio $\Phi_{\text{Fe}}/\Phi_{\text{Kr}}$ is almost the same for all three incidence angles. For a small $\alpha = \vartheta_{\text{Fe}} - \vartheta_{\text{Kr}}$ like in figure 4.18(a) the variation of the local flux ratio

$$\frac{\Phi_{\text{Fe}}}{\Phi_{\text{Kr}}}(\partial_x h) - \frac{\Phi_{\text{Fe}}}{\Phi_{\text{Kr}}}(0) \approx \frac{j_{\text{Fe}} \cos \vartheta_{\text{Fe}} \sin \vartheta_{\text{Kr}} - \sin \vartheta_{\text{Fe}} \cos \vartheta_{\text{Kr}}}{j_{\text{Kr}} \cos^2 \vartheta_{\text{Kr}}} \partial_x h \quad (4.1)$$

4.6. Discussion

due to height modulations is only small. The resulting concentration modulations are rapidly driven back by ion beam mixing and the height fluctuation are driven back by the smoothening of viscous flow and ballistic mass drift (CV effect). For a large α like in figure 4.18(c) the resulting flux modulations are much larger. Then these concentration modulations cannot be driven back by ion beam mixing and the height fluctuations are amplified by the reduced erosion rate due to silicide formation.

If phase separation would be the driving force, then pattern formation should be independent of α . As the flux ratio $\Phi_{\text{Fe}}/\Phi_{\text{Kr}}$ is the same also the average surface composition is the same. If this composition is in the range for phase separation then a pattern should form independently of α . On the other hand, if the composition is not in the range for phase separation, then no pattern should form.

To solve the problem that each of the models alone can only explain the results partially, one has to realize that ion beam pattern formation with impurity co-deposition is a synergetic effect of height and composition modulations. Both amplify each other in a feedback loop. Both mechanism discussed above contribute to this feedback. If composition modulations are induced by the oblique deposition these modulations are sustained by phase separation and not driven back by ion beam mixing. If phase separation leads to composition modulations these modulations induce height modulation. These height modulations enhance the composition modulations by the locally modulated impurity flux. Under conditions where one of both mechanisms is weak or inactive this feedback loop fails to amplify the pattern growth. If phase separation operates but α is too low, i. e. the flux modulation due to oblique deposition is small, the height modulations due to erosion rate differences are driven back by the CV effect. If, on the other hand, the effect of oblique deposition is substantial but no phase separation takes place, e. g., when a composition close to a stoichiometric silicide is reached fast for large metal-to-ion flux ratios $\Phi_{\text{M}}/\Phi_{\text{Kr}}$, the concentration modulations induced by the flux modulations are driven back by ion beam mixing and the amplification by the reduced erosion rate vanishes.

The coupling between morphology and composition discussed above has an important consequence. It takes time for both patterns, morphological and chemical, to develop. This helps to understand why the final impurity concentration alone is not enough to determine the resulting pattern. The morphology is influenced by the composition pattern, and vice versa, the composition pattern is influenced by the morphology. Thus the pattern does not only depend on the impurity flux ratio but also on the exact deposition geometry. With this in mind we will discuss a number of issues arising from our experiments.

One of the most striking results is the finding that for two co-deposition situations with the same Fe area density $n_{\text{Fe}} = 15 \times 10^{19}$ Fe atoms/m² very different morphologies result: after co-evaporation with a flux ratio $\Phi_{\text{Fe}}/\Phi_{\text{Kr}} = 0.3$ the sample remains flat (compare figure 4.17(c)), while after sputter co-deposition at $x = 1.2$ mm the sample displays a pronounced ripple pattern with $\sigma > 10$ nm (compare figure 4.16). The

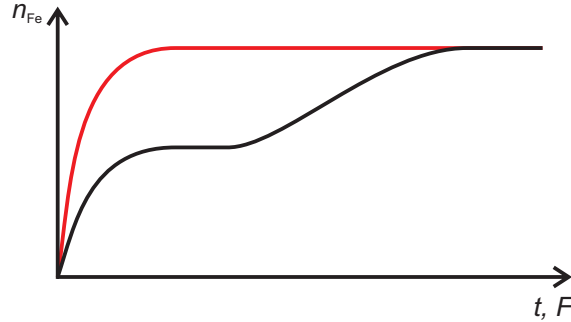


Figure 4.20.: Sketch of the assumed evolution of n_{Fe} during co-evaporation with $\Phi_{\text{Fe}}/\Phi_{\text{Kr}} = 0.3$ (red) and during sputter co-deposition at $x = 1.2$ mm (black). See the text for a detailed explanation.

two qualitatively different morphologies with identical Fe area density n_{Fe} evolved entirely different due to the different deposition conditions. The Fe area density evolutions sketched in figure 4.20 as a function of the ion fluence F are likely models of the history of n_{Fe} . For co-evaporation with the flux ratio $\Phi_{\text{Fe}}/\Phi_{\text{Kr}} = 0.3$ (red curve) the Fe area density n_{Fe} increases rapidly to the steady state value close to a stoichiometric silicide. During the increase of n_{Fe} the composition range where phase separation takes place (compare figure 4.17(b) with $n_{\text{Fe}} = 4.67 \times 10^{19}$ Fe atoms/m²) is crossed too fast to build up large concentration and height modulations. At the steady state composition ion beam mixing smooths out any concentration modulations created before. For sputter co-deposition at $x = 1.2$ mm (black curve in figure 4.20) n_{Fe} quickly rises initially, but reaches an intermediate saturation level. This intermediate level is probably close to n_{Fe} in the no-pattern zone at $x = 0.8$ mm, i. e. $n_{\text{Fe}} \approx 10 \times 10^{19}$ Fe atoms/m². While in the no-pattern zone pattern formation is suppressed for reasons discussed below, height and concentration fluctuations are not driven back and a pattern evolves. With increasing pattern amplitude kinetic facets evolve. The facets facing the Fe flux grow steeper to a slope $\alpha \approx 50^\circ$. These slopes receive almost the whole Fe flux. Due to the large slope only little Fe is sputtered away and most of the sputtered Fe is redeposited onto the surface. Due to this protection of Fe from sputtering n_{Fe} increases and may even exceed n_{Fe} of a smooth sample covered with a thin, homogeneous silicide layer.

A second result we want to discuss is the no-pattern zone near the metal target plate with $x < x_c$. We observe this zone for all three pattern forming metals Pd, Fe, and Ir investigated here. The critical distance x_c which is the end of the no-pattern zone increases with decreasing metal concentration of the Si rich silicide: 0.8 mm for Pd (Pd₂Si), 1.0 mm for Fe (FeSi₂), and 1.2 mm for Ir (IrSi₃). For Pd and Fe, where the metal area density was measured as a function of the distance x , the value of $n_{\text{Fe}/\text{Pd}}$ in the no-pattern zone can be found in the pattern zone at larger distances x .

4.6. Discussion

We identified three contributions to the no pattern zone, but cannot determine which of these contribution is decisive.

- (1) For each point x the impurity flux on the substrate comes from the entire target. The average angle α between ion beam and impurity flux increases with x . We have seen in figure 4.18 that a larger angle α between impurity flux and ion beam leads to stronger pattern formation. As α is smaller for $x < x_c$ than for $x > x_c$ we conclude that the deposition geometry fosters pattern formation for $x > x_c$.
- (2) As pointed out in chapter 3.3, the flux ratio $\Phi_{\text{Si}}/\Phi_{\text{metal}}$ of Si atoms to metal atoms decreases with increasing x . The additional deposition of Si reduces compositional modulations by modulations of the local deposition fluxes. This fosters pattern formation for $x > x_c$.
- (3) The ions hitting the target do not only sputter metal but are also partially scattered and hit the sample with significant energies. The flux of scattered ions onto the sample decreases with increasing x . This can be seen as an additional ion beam with a small angle α to the metal flux. This flux suppresses pattern formation due to the small α . As the flux decreases with x it fosters pattern formation for $x > x_c$.

An alternative explanation for the no-pattern zone was proposed by Zhang et al. [143]. Based on their experiments for Fe sputter co-deposition, they assume that in the no-pattern zone the impurity area density just matches the concentration for a thin layer of stoichiometric silicide. Similar to our Fe co-evaporation experiment with $\Phi_{\text{Fe}}/\Phi_{\text{Kr}} = 0.3$, this would suppress pattern formation, as impurity concentration fluctuations are efficiently driven back. This idea is consistent with our finding that the extension of the no-pattern zone is the larger, the lower the metal concentration in the first, Si-rich silicide (Pd_2Si , FeSi_2 , IrSi_3). However, identical metal area densities n_{M} can be found in the no-pattern zone and in the pattern zone for both, Pd and Fe (compare figure 4.7 and figure 4.16). Especially for Pd co-deposition, where all patterns are rather smooth with low corrugations, the variation of the measured Pd area density n_{Pd} must be assumed to reflect rather well the variation of the impinging Pd impurity flux. Thus, the absence of patterns in the no-pattern zone is most likely not due to the formation of a uniform stoichiometric silicide layer as proposed by Zhang et al. [147], but due to the x dependence of sputter deposition geometry, additional Si flux, as well as scattered Kr flux. In the Pd co-evaporation experiments (figure 4.8(c) and (d)), patterns form for a Pd area density n_{Pd} 50% larger than measured in the no pattern zone of the Pd sputter co-deposition experiment. This observation contradicts the assumption of a uniform layer of a stoichiometric silicide.

A third interesting observation is that the Pd area density n_{Pd} is the same for both flux ratios $\Phi_{\text{Pd}}/\Phi_{\text{Kr}} = 0.3$ (figure 4.8(c)) and $\Phi_{\text{Pd}}/\Phi_{\text{Kr}} = 0.8$ (figure 4.8(d)) of the Pd co-evaporation experiments. The morphology differs substantially for both flux ratios.

For the low flux ratio $\Phi_{\text{Pd}}/\Phi_{\text{Kr}} = 0.3$ the surface is rather smooth with shallow symmetric ripples with an amplitude of 1 nm. The high flux ratio plausible assumption that the steady state concentration is reached for both samples, the spatially averaged partial Pd sputtering yield is $0.8/0.3 = 2.7$ times higher for the high flux ratio than for the low flux ratio. The enhanced sputtering of Pd must be caused by the different morphologies and differences in the Pd distribution.

- (1) The TEM cross-section in figure 4.10 shows that the sample is covered by an ≈ 4 nm thick Pd_mSi layer with m in the range 2–3 on the flanks oriented toward the Pd flux. On the flanks oriented away from the Pd flux the Pd rich layer is thinner and the Pd concentration is lower as shown by the energy-filtered TEM image (figure 4.10(f)). Thus, it is plausible that phase separation was stronger for the flux ratio $\Phi_{\text{Pd}}/\Phi_{\text{Kr}} = 0.8$ than for $\Phi_{\text{Pd}}/\Phi_{\text{Kr}} = 0.3$, which is consistent with higher pattern amplitude for $\Phi_{\text{Pd}}/\Phi_{\text{Kr}} = 0.8$. If the average metal sputtering yield of a phase separated sample with metal rich and metal poor patches is considerably higher than the average metal sputtering yield of a sample with uniform composition, our finding, that n_{Pd} is the same for both flux ratios, could be understood. For the extreme case of a sample phase separated into Si and Pd as compared to uniform Pd_xSi layer the partial sputtering yields in table 4.1 support this view. But it is unclear whether this holds also for a more realistic material distribution.
- (2) Phase separation can also be observed in the direction perpendicular to the surface (see figure 4.10). The ion beam amorphized zone is composed of a Pd-rich layer close to the surface and a Pd-poor layer next to the crystalline bulk. If the Pd distribution within the amorphous layer is more uniform for the $\Phi_{\text{Pd}}/\Phi_{\text{Kr}} = 0.3$, i.e. the Pd surface concentration is lower, also the partial Pd yield would be lower, simply because sputtered atoms are surface atoms.
- (3) The larger slope of the facets helps to explain their larger average Pd sputtering yield for the $\Phi_{\text{Pd}}/\Phi_{\text{Kr}} = 0.8$. Pd arrives mainly at the facets facing the Pd flux. The slope of these facets facing is 10° and 30° for the flux ratios $\Phi_{\text{Pd}}/\Phi_{\text{Kr}} = 0.3$ and $\Phi_{\text{Pd}}/\Phi_{\text{Kr}} = 0.8$, respectively. TRIM.SP calculations show that the partial Pd sputtering yield is 40% higher for the latter.

All three arguments lead to enhanced Pd sputtering for the $\Phi_{\text{Pd}}/\Phi_{\text{Kr}} = 0.8$ sample and taken together may explain its much larger sputtering yield as compared to the $\Phi_{\text{Pd}}/\Phi_{\text{Kr}} = 0.3$ sample.

The fourth issue is the question, why no patterns form for Ag and Pb co-deposition. As seen in chapter 4.6 the formation of a silicide lowers the sputtering yields due to its enthalpy of formation. This transforms chemical patterns into morphological patterns. Although Ag and Pb do not form silicides and this effect is not operative, the erosion rate anyway depends on the composition. Therefore the absence of a morphological pattern

4.6. Discussion

indicates the absence of a chemical pattern. One could argue, that, because no silicide is formed, the free energy could not be lowered by phase separation into metal rich and metal poor patches and consequently the ion beam mixing drives back composition fluctuations. But, as Ag and Pb are virtually insoluble in Si, the free energy will be lowered by phase separation into patches of pure metal and pure silicon. To understand why phase separation does not take place we will recall some facts on spinodal decomposition from chapter 2.2. Spontaneous phase separation by uphill diffusion separation only takes place for concentrations c where the free energy $F(c)$ as function of the concentration is negatively curved, i. e. $\partial_c^2 F < 0$. For a situation with an average metal concentration far away from a well defined phase, e.g. pure metal, pure Si or a stoichiometric silicide, $F(c)$ will be far away from minima and fulfill the condition above. As the diffusion coefficient $D \propto \partial_c^2 F$ the uphill diffusion is stronger for larger $-\partial_c^2 F$. If uphill diffusion is strong enough concentration fluctuations are not driven back by the ion beam mixing (see chapter 2.1). For system with phases of large enthalpies of formation $-\Delta H_f$ and which are close in composition $-\partial_c^2 F$ is large. For Ag and Pb co-deposition on Si the two phases are the pure metals and pure Si. Even if the minima for pure metal and Si may be substantial $-\partial_c^2 F$ is still to small and ion beam mixing is stronger than spinodal decomposition.

The discussion above helps to understand the difference between good and poor pattern forming metal. In chapter 4.6 we saw that poor pattern formers are those that require larger metal concentrations in the silicide. This implies a larger separation of the minima in the $F(c)$ plot and thus smaller values of $-\partial_c^2 F$. Similarly important, to maintain a pattern with silicide patches a much larger supply of metal is necessary. It is obvious from table 4.1 that the metal sputtering yield from a metal-rich silicide is much larger than the one of a silicon-rich silicide.

The mechanisms discussed above have been modeled theoretically (see chapter 2.5). Bradley [9] discusses the destabilizing effect of oblique impurity deposition. Norris [104] discusses ion induced phase separation as origin of the surface instability. Next we compare the experimental results presented here to predictions from the theoretical models.

In Bradley's model the origin of the instability is the modulation of the local metal fluxes by height fluctuations in combination with the reduction of the erosion rate by silicide formation. Predictions from Bradley's model will be discussed in the following:

- (1) The wave vector of the ripples is predicted to be parallel to the projected metal flux direction. This has been observed here and several times in literature, e. g. [62, 79, 81, 115, 147].
- (2) Pattern formation is predicted to be stronger for larger angles between ion beam and metal flux. A smaller metal flux ratio $\Phi_{\text{metal}}^C/\Phi_{\text{ion}}$ is required to induce pattern formation. This prediction is confirmed by the experiments on the dependence of pattern formation on the angle between ion beam and metal flux (figure 4.18).

- (3) The model predicts that the metal is enriched at the mountainside of the ripple facing the metal flux near the crest. In agreement with this prediction, we observe the highest Pd concentration on the mountainside facing the Pd deposition. This region extends to the crest of the ripple. Previous work on impurity induced pattern formation on Si found the same behavior [32, 62, 80, 147, 149].
- (4) Bradley predicts that the pattern wavelength λ diverges like

$$\lambda \propto \left(\Phi_{\text{metal}}/\Phi_{\text{ion}} - \Phi_{\text{metal}}^{\text{C}}/\Phi_{\text{ion}} \right)^{-1/2}. \quad (4.2)$$

for metal flux ratios $\Phi_{\text{metal}}/\Phi_{\text{ion}}$ close above the critical flux ratio $\Phi_{\text{metal}}^{\text{C}}/\Phi_{\text{ion}}$ for pattern formation. In the experiments presented here we did not observe such a divergence. For Pd sputter co-deposition (compare figure 4.7) the wavelength even decreases monotonically with decreasing flux ratio until the pattern vanishes.

- (5) Bradley's model is only valid for small flux ratios that do not give rise to closed silicide layers. Evidently, situations where we observe no pattern due to formation of a continuous silicide layer, as in Fe co-evaporation with $\Phi_{\text{Fe}}/\Phi_{\text{Kr}} = 0.3$, are not accounted for by it.
- (6) In the model, pattern formation is only possible if the erosion speed Y/n of the silicide is smaller than the one for pure Si. Here, Y is the total sputtering yield and n the atom density. According to the calculated yields in table 4.1 we expect the erosion speeds of Pd₂Si or Pd₃Si to be 30% or 40% larger than the one for pure Si. A sufficiently large lateral Pd transport would make the partial Si sputtering the decisive quantity for the erosion speed as sputtered Pd is replenished by lateral transport. Phase separation is a mechanism that could provide such a lateral transport. The partial Si yields are in fact reduced for both silicides (compare with table 4.1).

In summary Bradley's model describes many central aspect of pattern formation induced by co-deposition of silicide forming metals correctly, while some predictions differ from the observed results. The pattern wavelength observed experimentally does not diverge as predicted for low flux ratios. The model requires that the erosion speed of the silicide has to be lower than of pure silicon, which is not the case for Pd. In this model the tendency of materials to phase separate to reduce the free energy is neglected.

In Norris' model [104] phase separation by spinodal decomposition is the driving force of pattern formation. The chemical pattern is than transformed into a morphological one by the dependence of the erosion rate on the composition. Within this model the suppression of pattern formation for high Fe flux ratios in the Fe co-evaporation experiments can be explained easily: If the average composition is close to an equilibrium phase the uphill diffusion from spinodal decomposition is too weak to overcome the ion beam mixing and an homogeneous layer is formed. For intermediate flux ratios spinodal decomposition

4.6. Discussion

drives the pattern formation. Also that pattern formation is stronger for metals with silicon rich silicides and large enthalpies of formation is explained by this model, as the uphill diffusion is then stronger. However important aspects of pattern formation are not explained by this model.

- (1) The ripple patterns are aligned with the metal flux. As this model is isotropic, it does not predict a preferential orientation of the pattern.
- (2) With increasing angle α between ion beam and metal flux the pattern formation is stronger. In this model the strength of pattern formation depends only on the average composition, which should be the same for the same flux ratio at different angles α .
- (3) The wavelength of the pattern formed by spinodal decomposition depends on the curvature of the free energy curve $\partial_c^2 F$. Thus one would expect large variations of the wavelength depending on the co-deposited metal and flux ratio. However the wavelength is $\lambda \approx 50$ nm for Pd, Fe and Ir.

The synergetic coupling between composition and height fluctuations destabilizes the surface. Phase separation helps to maintain and enhance composition fluctuations, which may occur spontaneously or can be induced by height fluctuations via the slope dependence of the metal deposition flux. The composition dependence of the erosion rate transforms composition modulations into height modulations. On the other hand, the slope dependence of the metal deposition flux transforms height fluctuations, either spontaneous or induced by composition fluctuations via the composition dependence of erosion, into composition fluctuations.

The formation of regular patterns requires that the destabilization is counteracted by a stabilization mechanism damping short wavelength fluctuations and thus a characteristic wavelength is selected. The destabilization mechanism described above is $\propto k^2$ in linear approximation. Ballistic mass drift [20] damps height fluctuations (see chapter 2.3) and ion beam mixing destroys composition modulations [30, 104] (see chapter 2.1). Both mechanisms are $\propto k^2$ and can suppress pattern formation. Ion induced viscous flow relaxation damps short wavelength fluctuations $\propto k^4$ [23, 26, 135] (see chapter 2.3). Also the free energy cost of concentration gradients $\propto k^4$ [16] might contribute, but as the wavelength depends only marginally on the deposited metal, this effects is unlikely to be relevant.

Conclusions

The data presented and discussed here give a strong evidence that neither height fluctuations nor phase separation alone can explain the wide range of phenomena observed in ion beam pattern formation with co-deposition of metal impurities.

For metal induced ion beam pattern formation it is necessary that the deposited metal forms silicides, but it is not a sufficient condition. The deposition parameters like metal flux, ion flux, incidence angles of metal atoms and ions determine if a pattern forms or not. By combining the results here with literature we can conclude that pattern formation is stronger the more Si rich the silicide is (compare figure 4.19). A large enthalpy of formation contributes to strong pattern formation, but is less decisive than the presence of a Si rich silicide.

For Ag co-deposition we have seen that in-situ experiments are essential for determining the resulting surface morphology. The ion beam mixes the deposited Ag into the surface yielding a homogeneous Ag distribution. Upon oxidization of the surface in air Ag precipitates to the surface and forms clusters.

Neither the modulation of the local deposition flux by height modulations nor phase separation alone can explain the various phenomena observed for ion beam pattern formation with metal co-deposition. The orientation of the pattern with respect to the metal flux is easily explained by the local flux variations, but not explained by phase separation. That patterns form more easily for large angle α between metal flux and ion beam can also be explained by the local flux variations, but not by phase separation. While the suppression of pattern formation for the high Fe flux ratio $\Phi_{\text{Fe}}/\Phi_{\text{Kr}} = 0.3$ can be explained easily by phase separation, but there is no obvious explanation through the local flux modulation. Here one has to take into account that both mechanisms can enhance each other by a synergistic coupling. Composition modulations induced by local flux modulations due to height fluctuations are sustained by phase separation. This leads to an amplification of the height fluctuations by the composition dependence of the erosion rate, which in turn enhances the local flux modulations.

We have seen that the metal area density n is not a good measure for pattern formation, as the resulting pattern depends not on n but on the metal flux ratio and details of the deposition geometry. The history of the sample morphology determines together with the former parameters the resulting metal area density.

The absence of pattern formation for the non-silicide forming metals Ag and Pb cannot be explained by the inability of phase separation. However, their driving force to phases separation is much smaller as the stable equilibrium phases are pure Si and pure metal. Therefore ion beam mixing may be stronger than phase separation. Also, the sputtering yield of the pure metals is higher than the partial metal sputtering yield in the mixed phase and precipitated metal is rapidly sputtered away. The weakly pattern forming metals are also characterized by these difficulties for pattern formation.

The sputter co-deposition setup can be used for a quick test whether a metal is suitable for pattern formation. For a detailed analysis of the mechanisms of pattern formation this setup introduces additional complexity due to complex particle fluxes involved. The co-evaporation setup provides more controlled conditions easing the analysis, although more experimental effort is needed.

5. Pattern formation without impurities

The results of this chapter have been published in *Physical Review B* [45].

Understanding ion beam pattern formation of Si at room temperature without co-deposition of impurities is essential for understanding ion beam pattern formation in more complicated situations like impurity co-deposition.

In this chapter the transition from a flat surface at $\vartheta = 55^\circ$ to the rippled surface at larger incidence angles and the fluence dependence of the pattern will be studied. For studying the temporal evolution of the surface morphology the angular ranges $\vartheta = 58^\circ$ to $\vartheta = 63^\circ$ yielding ripple patterns (figure 2.3(b)) and $\vartheta = 67^\circ$ to $\vartheta = 79^\circ$ yielding roof-tile patterns (figure 2.3(c)) are suited. For $\vartheta \leq 55^\circ$ no dependence of the morphology on fluence could be detected. For $\vartheta \geq 81^\circ$ the morphology changes only marginally with fluence. The evolution of the morphology will be studied at $\vartheta = 63^\circ$ in the ripple pattern range and at $\vartheta = 75^\circ$ in the roof-tile pattern range, where the roughness is maximal (figure 2.4).

5.1. Angle dependence near the transition from a flat surface to ripples

The transition from a flat surface at $\vartheta \leq 55^\circ$ to a ripple pattern at $\vartheta \geq 58^\circ$ is shown in figure 5.1. The quality of the patterns increases gradually from a shallow ripple pattern with a less defined wavelength at $\vartheta = 58^\circ$ (figure 5.1(a)) to a well pronounced ripple

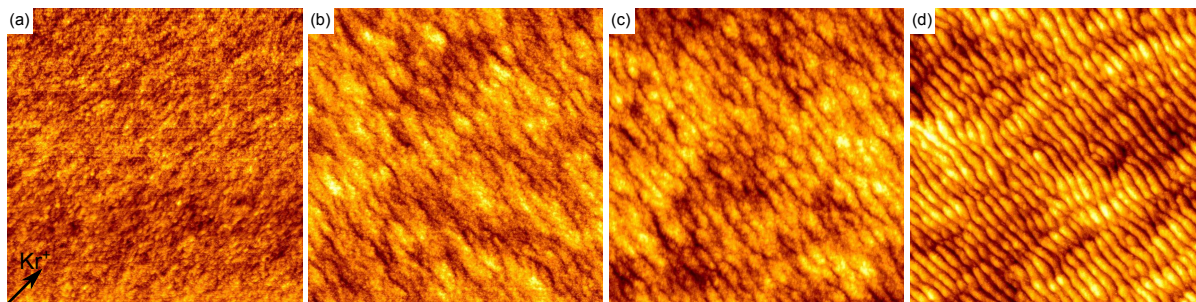


Figure 5.1.: STM topographs ($1\ \mu\text{m} \times 1\ \mu\text{m}$) after a fluence of $F = 1 \times 10^{22}$ ions/ m^2 2 keV Kr^+ with (a) $\vartheta = 55^\circ$, (b) $\vartheta = 58^\circ$, (c) $\vartheta = 60^\circ$, and (d) $\vartheta = 63^\circ$. The z-scales are (a) 2 nm, (b) 3.4 nm, (c) 4 nm, and (d) 5 nm. The arrow in (a) indicates the direction of the ion beam. (a) and (c) are from ref. [79].

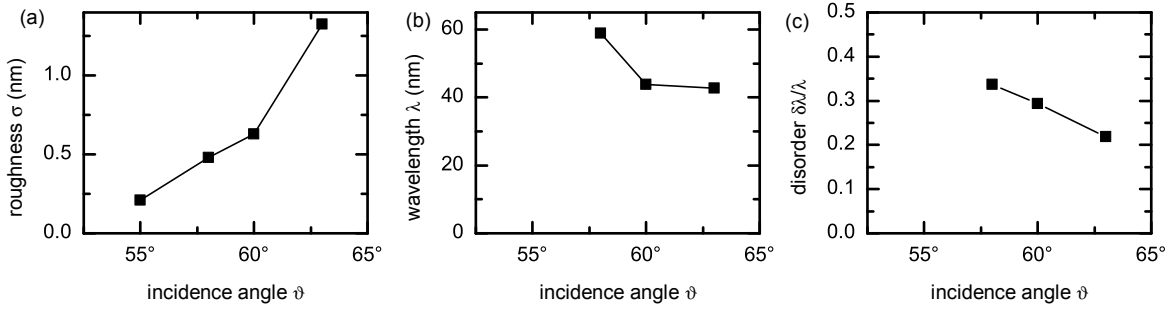


Figure 5.2.: Dependence of (a) roughness σ , (b) wavelength λ , and (c) disorder $\delta\lambda/\lambda$ on incidence angle ϑ near transition from flat to ripple surface.

pattern at $\vartheta = 63^\circ$ (figure 5.1(d)). With the onset of pattern formation the roughness increases from $\sigma = 0.2$ nm at $\vartheta = 55^\circ$ to $\sigma = 0.5$ nm at $\vartheta = 58^\circ$ (figure 5.2(a)). The roughness increases with ϑ to $\sigma = 1.3$ nm at $\vartheta = 63^\circ$. The pattern wavelength λ decreases with ϑ in the range $58^\circ \leq \vartheta \leq 63^\circ$ of ripple patterns (figure 5.2(b)). The wavelength is expected to be $\lambda \propto \sqrt{-D/S_x}$ from theory (see chapter 2.3) and $S_x \rightarrow 0$ when approaching the critical incidence angle from above. The increase in pattern quality with ϑ is reflected by the decreasing pattern disorder $\delta\lambda/\lambda$ measured by the standard deviation of the wavelength distribution normalized to the average wavelength (see equation (3.11) in chapter 3.5).

5.2. Pattern evolution at 63° incidence angle

A ripple pattern evolves at an ion incidence angle of $\vartheta = 63^\circ$. The evolution of the surface morphology with increasing fluence is shown in figure 5.3 with STM topographs and the corresponding slope angle distributions in figure 5.4 (see chapter 3.5). Initially the native oxide was removed by normal incidence 2 keV Kr^+ ion bombardment with a fluence of 5×10^{20} ions/m². The resulting amorphous surface is smooth with long wave length corrugations and a low roughness $\sigma \leq 0.3$ nm (figure 5.3(a)). The isotropic slope angle distribution is narrow and centered at $\alpha = 0^\circ$ (figure 5.4(a)). Off normal ion bombardment at $\vartheta = 63^\circ$ leads initially to the formation of shallow, segmented ripples (figure 5.3(b)) which connect to parallel mode ripples (figure 5.3(b)–(d)) with wave vector parallel to the projection of the ion beam onto the surface with increasing fluence. The shape of the ripples is initially symmetric which can also be seen in the slope angle distributions (figure 5.4(b)–(c)). Eventually they become asymmetric at $F = 1.0 \times 10^{21}$ ions/m² (figure 5.3(d)) with a pronounced downwind face. The upwind face is rounded. The slope of the downwind face is significantly smaller than for the upwind face (figure 5.4(d)). For larger fluences additional disordered, long wavelength ripples with wave vector perpendicular to the ion beam direction emerge (figure 5.3(e)–

5.2. Pattern evolution at 63° incidence angle

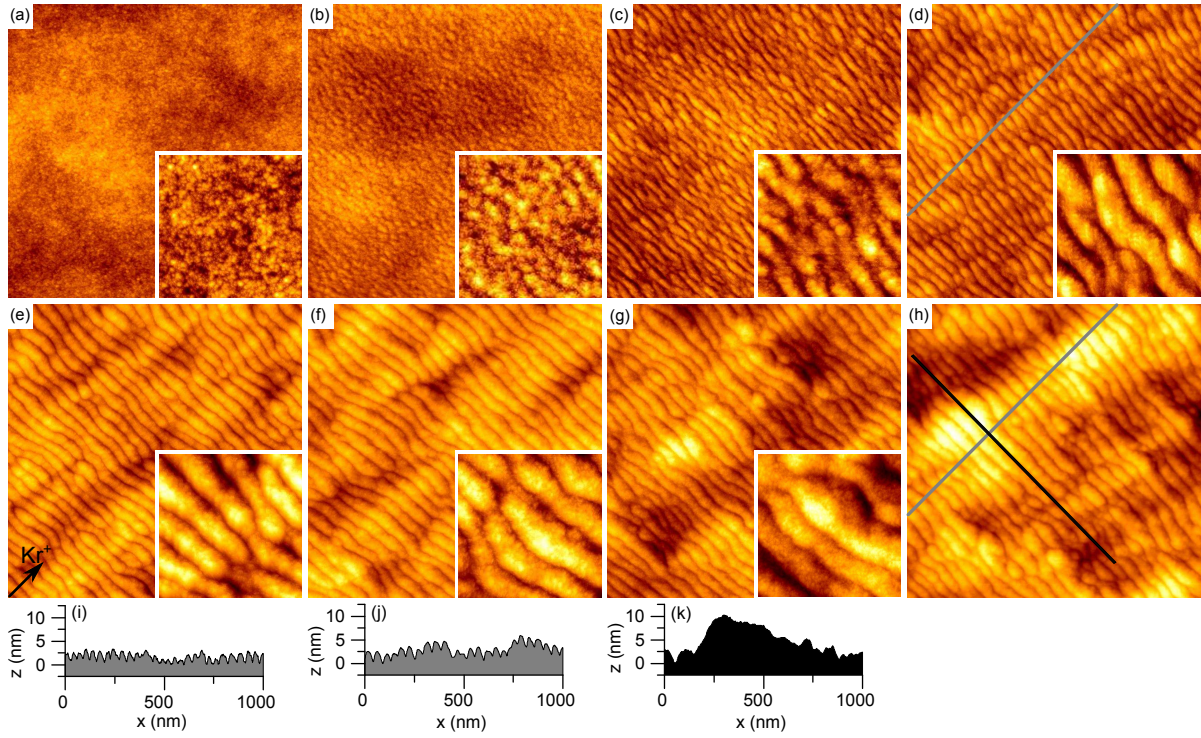


Figure 5.3.: (a)–(h) STM topographs (image size $1\ \mu\text{m} \times 1\ \mu\text{m}$, inset size $0.2\ \mu\text{m} \times 0.2\ \mu\text{m}$) after 2 keV Kr^+ ion bombardment: (a) initial state after removal of native oxide and amorphization by normal incidence ion bombardment, (b)–(h) after ion bombardment at $\vartheta = 63^\circ$ with increasing ion fluence: (b) $F = 1.0 \times 10^{20}$ ions/ m^2 , (c) $F = 3.0 \times 10^{20}$ ions/ m^2 , (d) $F = 1.0 \times 10^{21}$ ions/ m^2 , (e) $F = 3.0 \times 10^{21}$ ions/ m^2 , (f) $F = 1.0 \times 10^{22}$ ions/ m^2 , (g) $F = 3.0 \times 10^{22}$ ions/ m^2 , and (h) $F = 9.5 \times 10^{22}$ ions/ m^2 . The z-scales are (a) 4 nm, (b)–(c) 5 nm, (d) 8 nm, (e) 10 nm, and (f)–(h) 12 nm. The projected ion beam direction is indicated by the arrow in (e). (i) Height profile along line in (d). (j)–(k) Height profiles along lines in (h) parallel and perpendicular to the ion beam direction, respectively.

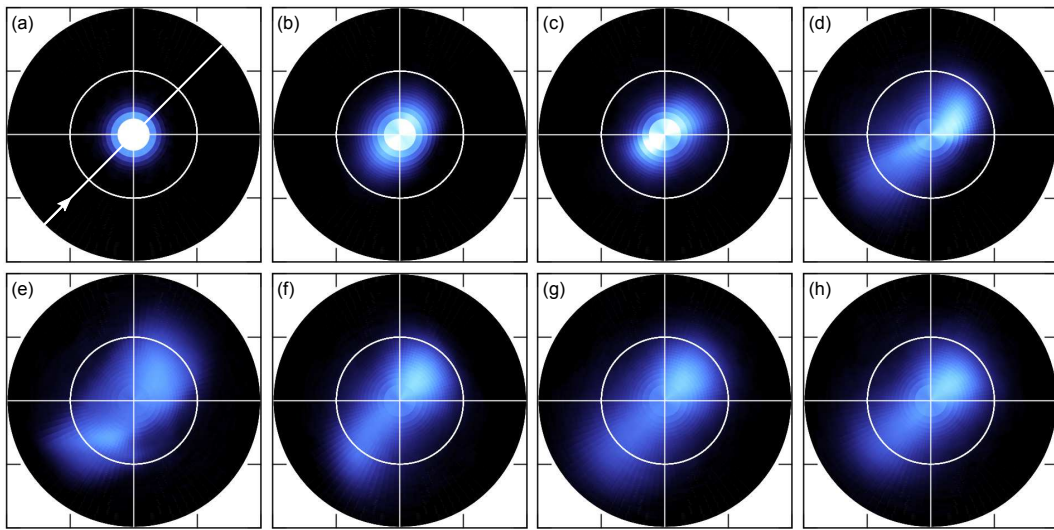


Figure 5.4.: (a)–(h) Slope angle distributions of Figs. 5.3(a)–(h). The slope angle varies from $\alpha = 0^\circ$ in the center to $\alpha = 20^\circ$ at the edge of the polar plot.

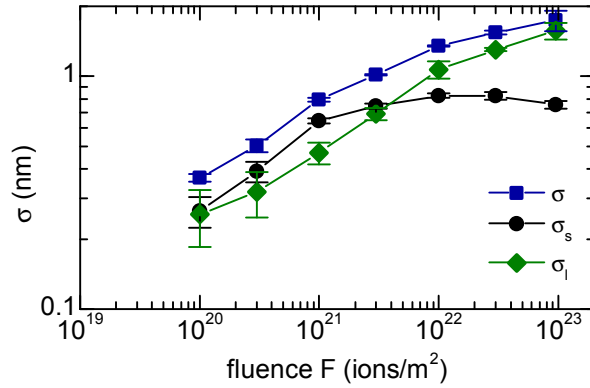


Figure 5.5.: Evolution of the roughness σ , the short wavelength roughness component σ_s , and the long wavelength roughness component σ_l as a function of ion fluence F for $\vartheta = 63^\circ$.

(h)), while the amplitude of the parallel ripple mode saturates.

The STM images are too small to decide whether the perpendicular long wavelength ripples have a characteristic wavelength or whether they are a superposition of undulations with a broad range of wavelengths. Keller et al. [71] reported the emergence of such perpendicular long wavelength ripple on Si(001) after 300 eV and 500 eV Ar^+ ion bombardment at $\vartheta = 67^\circ$. They could determine the characteristic wavelength of the perpendicular ripples by analyzing large scale AFM topographs. The surface morphology we observe is very similar to the surface morphology of Keller et al. [71] at the same scale. Following Keller et al. [71] these ripples will be referred to as a disordered perpendicular mode although our STM images are too small to decide if these ripples possess a characteristic wavelength. Such a disordered perpendicular mode of ripples has also been observed by Castro et al. [21] for 500 eV and 700 eV Ar^+ on Si(001) with $\vartheta = 65^\circ$ and $\vartheta = 70^\circ$ respectively, and by Teichmann et al. [131] for 600 eV Xe^+ on Ge(001) with $\vartheta = 65^\circ$.

The saturation of the parallel mode is obvious by comparing the height profiles in figure 5.3(i) and (j) along the gray lines parallel to the ion beam in figure 5.3(d) and (h) respectively. The wavelength increases slightly, but shape and amplitude of the ripples is almost the same. Along the ion beam direction the distribution of slope angles does not change much for high fluences $F \geq 1.0 \times 10^{21}$ ions/m² (figure 5.4(d)–(h)). Perpendicular to the ion beam direction the distribution gets broader with increasing fluence. This coincides with the emergence of a disordered perpendicular mode which modulates the height of the parallel mode ripples along the direction of the ripple ridges. Comparing the height profiles figure 5.3(j) and (k) taken parallel and perpendicular to the ion beam respectively (gray and black lines in figure 5.3(h)) at the fluence $F = 9.5 \times 10^{22}$ ions/m² shows that the amplitude of the disordered perpendicular mode is eventually larger than the amplitude of the parallel mode.

5.2. Pattern evolution at 63° incidence angle

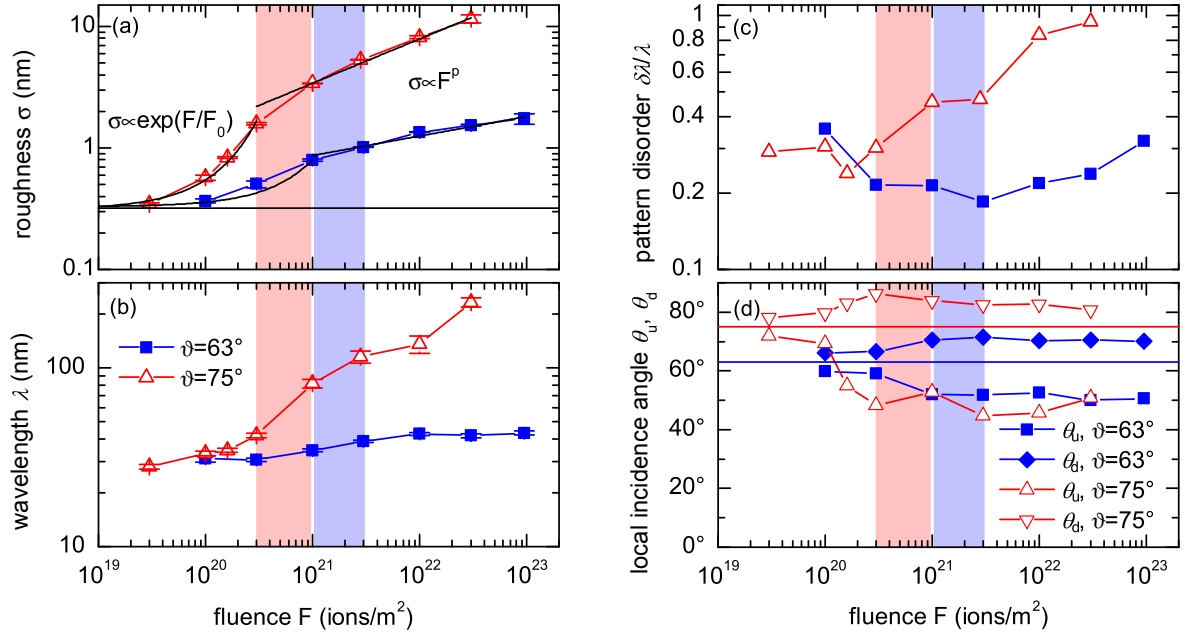


Figure 5.6.: Evolution of (a) roughness σ , (b) wavelength λ , (c) pattern order $\delta\lambda/\lambda$, and (d) local ion incidence angle θ_u on upwind and θ_d on downwind ripple faces. In (a) the horizontal line indicates the sample roughness prior to off-normal ion exposure. In (d) the horizontal lines indicate the global incidence angles. The transition range between the low fluence and high fluence regimes is highlighted by the light blue shaded area for the $\vartheta = 63^\circ$ experiments and by the light red shaded area for the $\vartheta = 75^\circ$ case.

Figure 5.5 displays the evolution of the roughness σ of the sample, the roughness σ_s of the short wavelength components with $\lambda < 140$ nm, and the roughness σ_l of the long wavelength components with $\lambda > 140$ nm (see chapter 3.5). At $F = 3.0 \times 10^{21}$ ions/m² the evolution of the roughness changes characteristically: For lower fluences the roughness σ is dominated by the short wavelength components σ_s from the parallel mode ripples, while for higher fluences the roughness is dominated by the long wavelength components σ_l from the disordered perpendicular mode. The roughness of the short wavelength components σ_s grows faster than σ_l initially, until it saturates for $F > 1.0 \times 10^{21}$ ions/m². The roughness of the long wavelength components σ_l continues to grow and crosses σ_s at $F = 3.0 \times 10^{21}$ ions/m². At this fluence the surface displays a clearly visible disordered perpendicular mode with a characteristic length scale of 100 nm to 200 nm (figure 5.3(e)).

Figure 5.6 summarizes the evolution of (a) roughness σ , (b) parallel mode ripple wavelength λ , (c) pattern disorder $\delta\lambda/\lambda$, and (d) the local incidence angles of upwind θ_u and downwind θ_d face for both incidence angles $\vartheta = 63^\circ$ (blue symbols) and for comparison also for $\vartheta = 75^\circ$ (red symbols). The horizontal line in figure 5.6(a) indicates the initial sample roughness. The wavelength of the parallel mode increases only slowly with fluence from $\lambda = (31 \pm 1)$ nm at $F = 3.0 \times 10^{20}$ ions/m² to $\lambda = (43 \pm 1)$ nm at

$F = 9.5 \times 10^{22}$ ions/m². For fluences $F < 3 \times 10^{21}$ ions/m² the disorder $\delta\lambda/\lambda$ of the pattern decreases, which is supported by the visual appearance of the patterns (figure 5.3(b)–(e)). The minimum of the disorder is $\delta\lambda/\lambda = 0.2$ at $F = 3 \times 10^{21}$ ions/m². For larger fluences disorder increases again, which is also visible in the topography (figure 5.3(e)–(h)).

The local incidence angles in figure 5.6(d) θ_u and θ_d on the upwind and downwind are calculated from the maximum slope angles¹ α_u and α_d of the upwind and downwind face via $\theta_u = \vartheta - \alpha_u$ and $\theta_d = \vartheta + \alpha_d$. The blue horizontal line indicates the (global) incidence angle ϑ . For fluences $F \leq 3.0 \times 10^{20}$ ions/m² the symmetric shape of the ripples (figure 5.3(b)–(c)) is reflected by the equal maximum slopes visible by the equal separation of θ_u and θ_d from ϑ . In the fluence range from $F = 3.0 \times 10^{20}$ ions/m² to $F = 1.0 \times 10^{21}$ ions/m² the ripples become steeper: the upwind face tilts toward the ion beam and the downwind face away from it. The ripples also become asymmetric in this fluence range. For high fluences $F > 1.0 \times 10^{21}$ ions/m² the slopes $\alpha_u \approx 11^\circ$, $\alpha_d \approx 8^\circ$ and the local incidence angles $\theta_u \approx 52^\circ$, $\theta_d \approx 71^\circ$ are stable.

The surface morphology differs for low and high fluences. Also the evolution of the roughness of short and long wavelength components, of the pattern disorder and the surface slopes differ for low and high fluences. This leads to distinction of a low fluence regime for $F < 1 \times 10^{21}$ ions/m² and a high fluence regime for $F > 3 \times 10^{21}$ ions/m². The gradual transition is highlighted by the light blue vertical bar in figure 5.6 between $F = 1 \times 10^{21}$ ions/m² and $F = 3 \times 10^{21}$ ions/m². In the low fluence regime only the parallel ripple is present. The ripple amplitude grows, the pattern disorder decreases and the ripple slopes increase with increasing fluence while the ripple shape changes from symmetric to asymmetric. In the high fluence regime a disordered perpendicular mode evolves which dominates the roughness. The wavelength and profile of the parallel mode ripples becomes stationary. Due to the growth of the perpendicular mode, the disorder of the parallel mode increases.

5.3. Pattern evolution at 75° incidence angle

At the incidence angle $\vartheta = 75^\circ$ a roof-tile morphology develops and the surface roughening is the strongest (compare figure 2.4). The evolution of the surface morphology during ion bombardment with the incidence angle $\vartheta = 75^\circ$ as function of the fluence is shown by the STM and AFM topographs in figure 5.7. Figure 5.8 shows the corresponding slope angle distributions. Already for a fluence as low as $F = 3.0 \times 10^{19}$ ions/m² the grains in the grainy surface structure have a characteristic separation (figure 5.7(a)). The slope angle distribution is still isotropic (figure 5.8(a)). With increasing fluence the pattern transforms into a ripple pattern at $F = 1.0 \times 10^{20}$ ions/m² (figure 5.7(b)). The shape of the ripple is still symmetric, which can be seen in the slope angle distribution

¹See figure 3.6 in chapter 3.5 for the definition of α_u and α_d .

5.3. Pattern evolution at 75° incidence angle

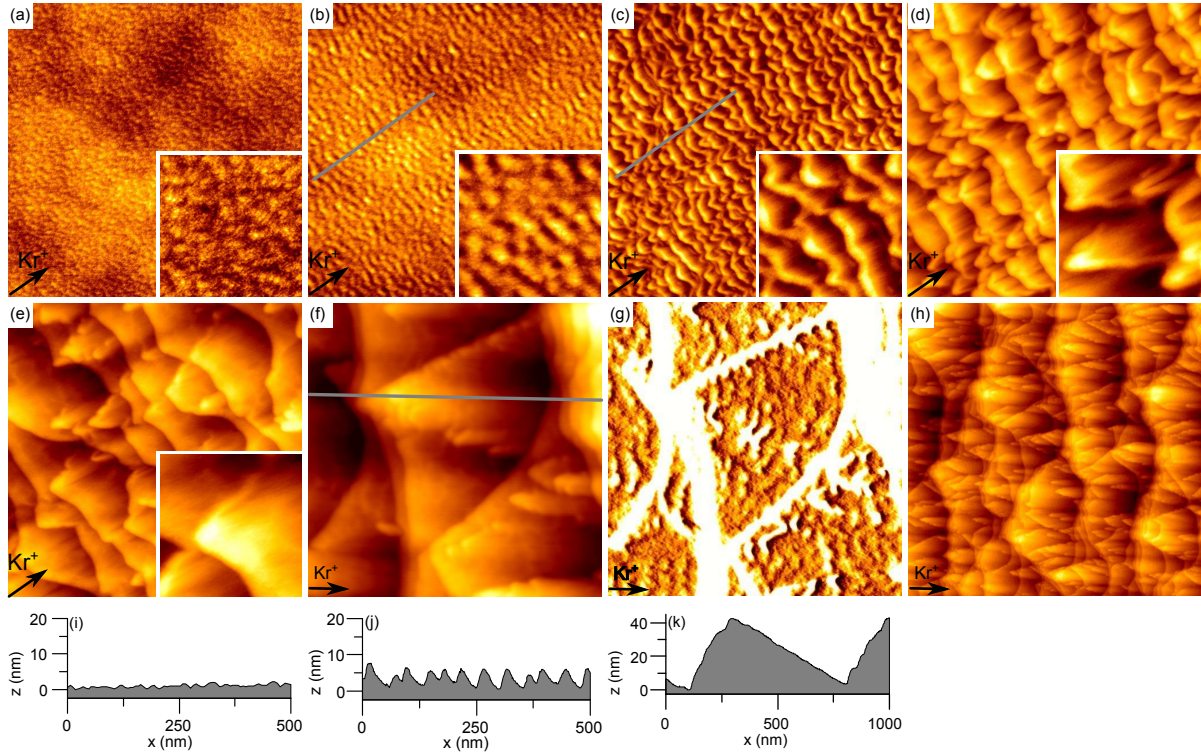


Figure 5.7.: (a)–(e) In-situ STM topographs and (f) ex-situ AFM image (image size $1 \mu\text{m} \times 1 \mu\text{m}$, inset size $0.3 \mu\text{m} \times 0.3 \mu\text{m}$) after 2 keV Kr^+ ion bombardment at $\vartheta = 75^\circ$ with fluences of (a) $F = 3.0 \times 10^{19}$ ions/ m^2 , (b) $F = 1.0 \times 10^{20}$ ions/ m^2 , (c) $F = 3.0 \times 10^{20}$ ions/ m^2 , (d) $F = 1.0 \times 10^{21}$ ions/ m^2 , (e) $F = 3.0 \times 10^{21}$ ions/ m^2 , and (f) $F = 3.0 \times 10^{22}$ ions/ m^2 . The z -scales are (a) 10 nm, (b)–(c) 20 nm, (d) 30 nm, (e) 35 nm, and (f) 70 nm. (g) Derivative of (f) in horizontal direction that highlights the corrugation on downwind faces. (h) Large scale ex-situ AFM $5 \mu\text{m} \times 5 \mu\text{m}$ image after $F = 3.0 \times 10^{22}$ ions/ m^2 (z -scale 100 nm). The projected ion beam direction is indicated by an arrow in each case. (i)–(k) Height profiles along lines parallel to ion beam direction as indicated in (b), (c), and (f), respectively.

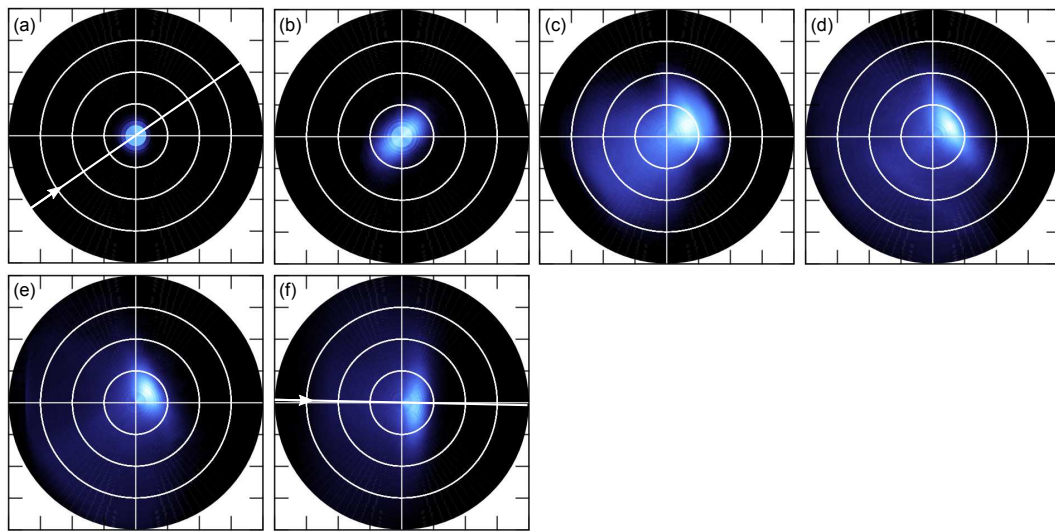
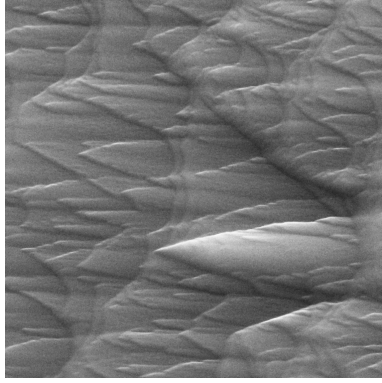


Figure 5.8.: (a)–(h) Slope angle distributions of Figs. 5.7(a)–(f). The slope angle varies from $\alpha = 0^\circ$ in the center to $\alpha = 40^\circ$ at the edge of the polar plot.

**Figure 5.9.:**

Secondary electron SEM image of the roof-tile pattern after 2 keV Kr^+ bombardment at $\vartheta = 75^\circ$ with the fluence $F = 3.0 \times 10^{22}$ ions/m². The image width is 3 μm and the tilt angle is 38.9°

(figure 5.8(b)). The pattern is better developed at this fluence for $\vartheta = 75^\circ$ than for $\vartheta = 63^\circ$. The pattern amplitude grows fast while the pattern coarsens strongly for larger fluences (see figures 5.7(c)–(f) and the height profiles in figures 5.7(i)–(k)). The downwind faces develop well defined kinetic facets (figure 5.8(c)–(f)). The upwind faces become steep and develop the appearance of a rounded step. The ridge-line of the ripples is initially wavy with some v-shaped tips (figure 5.7(c)). On top of the downwind faces grooves in ion beam direction develop (figure 5.7(d)). These grooves lead to a broadening of slope angle distribution perpendicular to the ion beam. The v-shaped tips develop into triangular shaped roof tile structures. The pattern coarsens strongly and the downwind faces grow (figure 5.7(d)–(f)), while the regularity of the pattern decreases with fluence. At the fluence $F = 3.0 \times 10^{22}$ ions/m² the length of the downwind faces is up to 1 μm (figure 5.7(f) and (h)). These roof-tile structures are often separated by stair like bunches of alternating upwind and downwind faces. The downwind faces are hit by the ions at a grazing local incidence angle of $\theta_d = 82^\circ$. The additional ripple pattern on the large downwind faces with a periodicity of ≈ 50 nm is highlighted by the horizontal derivative figure 5.7(g). Figure 5.9 shows an SEM image of the surface at the fluence $F = 3.0 \times 10^{22}$ ions/m².

The evolution of the surface roughness shown in figure 5.6(a) in red is much faster than for $\vartheta = 63^\circ$. For fluences $F < 1.0 \times 10^{21}$ ions/m² the roughness growth exponentially and can be fitted by $\sigma \propto \exp F/F_0$ with $F_0 = (1.8 \pm 0.1) \times 10^{20}$ ions/m². For higher fluences the roughness grows by a power law $\sigma \propto F^p$ with $p = 0.36 \pm 0.03$.

Initially, for fluences $F \leq 3.0 \times 10^{20}$ ions/m², the structure size in direction of the ion beam λ (wavelength) grows only moderately (see figure 5.6(b)). For higher fluences the pattern coarsens rapidly, in contrast to $\vartheta = 63^\circ$. The coarsening coincides with a dramatic disordering of the pattern. At $F = 3.0 \times 10^{22}$ ions/m² the standard deviation $\delta\lambda$ of the structure size distribution almost equals the average structure size λ (figure 5.6(c)).

The local incidence angles θ_u , θ_d of the upwind and downwind side, respectively, move away from the global incidence angle $\vartheta = 75^\circ$ indicated by the red line in figure 5.6(d) for low fluences $F \leq 3.0 \times 10^{20}$ ions/m². Only for $F \leq 1.0 \times 10^{20}$ ions/m² the evolution of θ_u and θ_d is symmetric. During further ion bombardment, the local incidence angle of

5.4. Discussion

the upwind face θ_u moves much faster away from the global incidence angle ϑ than θ_d . Therefore, the ripple shape is asymmetric as seen in the topographs (figure 5.7(c)–(f)). Above the fluence $F = 3.0 \times 10^{20}$ ions/m² the local incidence angle are stable. The slopes are $\alpha_u \approx 25^\circ$ corresponding to an local incidence angle of $\theta_u \approx 50^\circ$ for the upwind face and $\alpha_d \approx 8^\circ$ corresponding to an local incidence angle of $\theta_d \approx 82^\circ$ for the downwind face. The larger scatter of θ_u for $\vartheta = 75^\circ$ may be caused by the steepness of the face, as the measured slope could be limited by the tip sharpness.

Also for $\vartheta = 75^\circ$ we can distinguish two fluence regimes of pattern formation: the low fluence regime for $F \leq 3.0 \times 10^{20}$ ions/m² and the high fluence regime for $F \geq 1.0 \times 10^{21}$ ions/m². The gradual transition is highlighted by the light red shaded bar in figure 5.6. Compared to $\vartheta = 63^\circ$ the transition takes place at lower fluences. In the low fluence regime a parallel mode ripple pattern emerges quickly. After the ripples emerged, the roughness grows exponentially, the pattern slightly coarsens, the pattern disorder is constant, and the ripples steepen and develop well oriented faces while their shape becomes asymmetric with increasing fluence. In the high fluence regime the ripple pattern is lost and a roof-tile pattern with well defined faces develops. The roof-tile pattern strongly coarsens and disorders. During this coarsening the slopes remain fixed.

5.4. Discussion

For both incidence angles, $\vartheta = 63^\circ$ and $\vartheta = 75^\circ$, two fluence regimes can be identified by phenomenological differences in the evolution of the surface morphology. The transition between the regimes is gradual and the fluence range of the transition is higher by a factor of approximately 3 for $\vartheta = 63^\circ$ compared to $\vartheta = 75^\circ$. The tables 5.1 and 5.2 summarize important properties of both regimes for $\vartheta = 63^\circ$ and $\vartheta = 75^\circ$ respectively. In the low fluence regime the evolution is similar for both incidence angles, while the high fluence regimes differ qualitatively.

The low fluence regimes can be approximated by a linear model of the form proposed by Bradley and Harper [14] (see also chapter 2.3):

$$\partial_t h = -v_0 + \partial_\theta v_0 \Big|_{\theta=\vartheta} \partial_x h + S_x \partial_x^2 h + S_y \partial_y^2 h - D \nabla^4 h. \quad (5.1)$$

Here, v_0 is the erosion speed of a flat surface, $\partial_\theta v_0$ is the contribution of its dependence on the local incidence angle θ . S_x and S_y are curvature dependent contributions, and D is the surface relaxation due to the minimization of the surface free energy. The projected ion beam direction is parallel to the x -axis. If S_x or S_y are negative the surface is unstable to perturbations and a ripple pattern forms. As already discussed in chapter 2.3 the curvature dependence of the erosion speed, as shown by Bradley and Harper [14], and mass redistribution contribute to S_x and S_y . Mass redistribution contributing to pattern formation has been introduced by Carter and Vishnyakov [20] and was further studied in the models of ion induced solid flow [21, 22] or the crater function approach [105, 106].

Table 5.1.: Regimes of morphological evolution at $\vartheta = 63^\circ$

	Low fluence regime	High fluence regime
fluence F	$\leq 1.0 \times 10^{21}$ ions/m ²	$\geq 3.0 \times 10^{21}$ ions/m ²
morphology	parallel mode ripples	disordered perpendicular mode + parallel mode ripples
roughness σ_s, σ_1	σ_s increases σ_1 increases slowly	σ_s constant σ_1 increases
slope angles α_d, α_u	increase	constant
wavelength λ	slight coarsening	slight coarsening
pattern disorder $\frac{\delta\lambda}{\lambda}$	decreases	increases

Table 5.2.: Regimes of morphological evolution at $\vartheta = 75^\circ$

	Low fluence regime	High fluence regime
fluence F	$\leq 3.0 \times 10^{20}$ ions/m ²	$\geq 1.0 \times 10^{21}$ ions/m ²
morphology	parallel mode ripples	roof-tile structure
roughness σ	exponential growth	power law growth
slope angles α_d, α_u	increase	constant
wavelength λ	slow coarsening	fast coarsening
pattern disorder $\frac{\delta\lambda}{\lambda}$	constant	increases

For elemental semiconductors and sufficiently low incidence angles ϑ , all of these theories predict that $S_x < S_y$, i. e. that if the surface is unstable to perturbations parallel mode ripples grow. The disorder of the pattern will decrease with fluence. The wave vector of the fastest growing ripple mode selects the wavelength of the pattern and eventually dominates the surface morphology. Experimentally, we observe parallel mode ripples in the low fluence regime for both incidence angles. The roughness can be fitted moderately at $\vartheta = 63^\circ$ and quite well at $\vartheta = 75^\circ$ with an exponential growth (compare figure 5.6(b)). The observed pattern disorder decreases with ion fluence as expected at $\vartheta = 63^\circ$ or at least, it does not increase at $\vartheta = 75^\circ$ (compare figure 5.6(c)).

This low fluence regime can only be described *approximately* by linear models, as the evolution deviates slightly from the behaviour expected from linear models: for example the ripple patterns slowly coarsens at $\vartheta = 75^\circ$.

Our observations differ in two aspects from models based on the Sigmund theory of sputtering [126], like the Bradley-Harper model [14] and its extensions [8, 88]. First, we observe no ripple rotation from parallel mode ripples to perpendicular mode ripples with increasing ϑ . The ripple rotation with increasing ϑ has been observed experimentally for other systems [69] and the ability of the Bradley-Harper type models to reproduce this ripple rotation was key to their acceptance as a valid description of ion beam induced pattern formation.

Second, ripples emerge only for angles ϑ larger than a critical angle ϑ_c . The curvature

5.4. Discussion

dependence of sputtering leads to an instability for $\vartheta > 0^\circ$ as shown by Bradley and Harper [14]. For 2 keV Kr^+ ions we observe ripples only for $\vartheta > 55^\circ$. The fact that ripples emerge only for incidence angles larger than a critical angle, can be explained by models taking mass redistribution into account (see chapter 2.3), either by ballistic mass drift [20], by solid flow [21, 22], or by the average crater shape of single impacts called “crater function” [105, 106]. The solid flow model of Castro and Cuerno [22] together with the assumption of an ion induced “effective body force” $b \propto \cos\theta$ in direction of the ion beam, where θ is the local incidence angle, predicts a critical angle $\vartheta_c = 45^\circ$, independent of ion energy and species, like in the ballistic mass drift model of Carter and Vishnyakov [20]. To explain the transition from a flat to a rippled surface between $\vartheta = 55^\circ$ and $\vartheta = 58^\circ$, the body force needs to be modified. The crater function approach of Norris, Brenner, and Aziz [105] and Norris et al. [106] also includes mass redistribution as an integral part of the model. By obtaining the moments of the crater function from averaging over many impacts simulated by molecular dynamics (MD), they predict the transition from a flat to a rippled surface at $\vartheta_c = 40^\circ$ for 250 eV Ar^+ ion bombardment. The validity of their framework for the situation here can only be assessed if the MD are extended to higher ion energies and heavier ions.

Based on the ion induced solid flow model, Castro et al. [21] predict an intrinsic timescale τ that limits the description of the morphological evolution through a linear partial differential equation. It scales with ϑ as $\tau(\vartheta) \propto 1/\cos^2(2\vartheta)$, i.e. with increasing incidence angle ϑ shifts to smaller fluences F . The predicted ratio of the timescales for the experiments presented here is $\tau(63^\circ)/\tau(75^\circ) = 2.2$ which corresponds to a ratio of fluences $F(63^\circ)/F(75^\circ) = 3.8$. In fact, experimentally we find $F(63^\circ)/F(75^\circ) \approx 3$ in reasonable agreement with the prediction of the solid flow model (compare Fig. 5.6).

Next, the high fluence regime for $\vartheta = 63^\circ$ will be discussed. The saturation of the short wavelength mode observed at $F = 1.0 \times 10^{21}$ ions/m² (compare Fig. 5.5) is clearly a non-linear effect. A simple non-linear partial equation able to describe the saturation of one mode is the anisotropic Kuramoto-Sivashinsky equation (aKS equation)[34]

$$\partial_t h = S_x \partial_x^2 h + S_y \partial_y^2 h - D \nabla^4 h + \frac{\lambda_x}{2} (\partial_x h)^2 + \frac{\lambda_y}{2} (\partial_y h)^2. \quad (5.2)$$

Here S_x, S_y and D are the same coefficients as for equation (5.1). λ_x, λ_y incorporate the dependence of the erosion rate on the local incidence angle. For $S_x < S_y < 0$, the aKS equation predicts the growth of a parallel ripple mode at early times which will eventually saturate [70, 88, 110, 118]. Numerical simulations by Keller et al. [70] for $\lambda_x \gg \lambda_y > 0$ show the emergence of a perpendicular mode in qualitative agreement with the surface morphology in the high fluence regime observed here for $\vartheta = 63^\circ$.

The evolution in the $\vartheta = 75^\circ$ high fluence regime is qualitatively different from the one at $\vartheta = 63^\circ$. A roof-tile morphology forms which exhibits strong coarsening and disordering of the pattern. This behaviour is connected to non-local effects, especially

reflected ions hitting the sample again at distant locations. As partial differential equations (PDEs) are inherently local, they cannot describe non-local effects. Redeposition has recently been included into a new type of *non-local* continuum modeling resulting in a partial integro-differential equation for the surface evolution [11, 38], but the effect of reflected ions and the sputtering associated with them has so far been neglected. Their effect can be included in a similar way.

Indeed, for grazing incidence angles the overwhelming fraction of ions experiences only a sequence of small angle scattering at surface atoms, i.e. the projectiles do not penetrate the surface, but are reflected with little energy loss by the surface layer atoms [7]. The reflected ions may hit surface features in their path of flight and can thereby contribute substantially to sputtering [116]. Based on his observations for 10 keV Ar⁺ ion exposure of Ag crystals, Hauffe [60] proposed that sputtering through reflected ions is the origin of rapid coarsening (see chapter 2.3). The Hauffe mechanism has also been invoked to explain the strong coarsening observed for the Ge(001) morphology upon 1.2 keV Xe⁺ exposure with $\vartheta = 75^\circ$. [131] The same mechanism is considered here to be responsible for the rapid coarsening in the morphological evolution of Si(001) under $\vartheta = 75^\circ$ 2 keV Kr⁺ bombardment.

Ions hit the downwind face with a local incidence angle $\theta \geq 82^\circ$ (figure 5.6(d)). Based on TRIM.SP calculations, $\approx 80\%$ of the ions are reflected and predominantly scattered into grazing directions with a small angular spread. These ions hit the adjacent upwind face and enhance the erosion there. The additional flux of reflected ions onto a given upwind face is enhanced the stronger, the larger the feeding downwind face, as described in chapter 2.3. This coarsening mechanism prefers the formation of large downwind faces, but it does not select a specific structure size. Thus, the order of the surface is expected to decline with continued erosion, as observed.

To estimate the relevance of the Hauffe mechanism in the high fluence regime we calculated the flux ratio $r = \Phi_r/\Phi_p$ of ions reflected onto the upwind face to primary ions hitting it directly. Assuming specular reflection for simplicity, the flux ratio is $r = R(\theta_d) \cos(\theta_r)/\cos(\theta_u)$, where $R(\theta_d)$ is the ion reflectivity as function of the local incidence angle on the downwind face, $\theta_r = 180^\circ - \vartheta - \alpha_u - 2\alpha_d$ is the local incidence angle of reflected ions on the upwind face, $\theta_{d,u} = \vartheta \pm \alpha_{d,u}$ are the local incidence angles of the primary ion on the downwind and upwind faces and $\alpha_{d,u}$ are the slope angles of the downwind and upwind face. For $\vartheta = 63^\circ$, the reflectivity $R < 0.3$ at the downwind face leads to a flux enhancement $r < 0.01$ and the effect of reflected ions on the morphological evolution must be considered to be minor. For $\vartheta = 75^\circ$, the reflectivity of the downwind face is $R \approx 0.8$ in the high fluence regime. The resulting flux enhancement of $r \approx 0.6$ is substantial and certainly sufficient to trigger the observed coarsening.

The well defined faces observed in the high fluence regime for $\vartheta = 75^\circ$ suggest that gradient dependent sputtering might be relevant for this regime. Indeed, Carter, Colligon, and Nobes [19] showed that faces with local incidence angles of 0° , 90° , and θ_{\max} (the

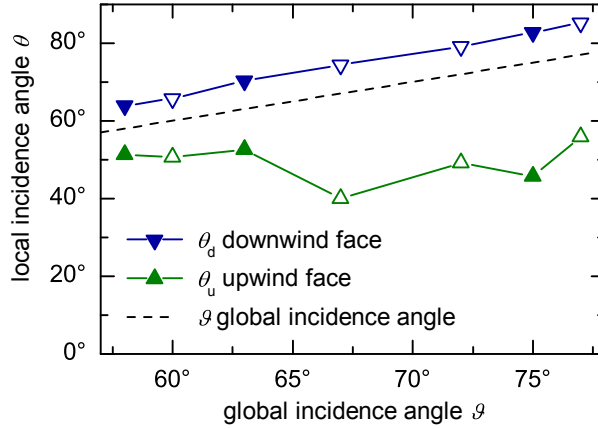


Figure 5.10.: Local incidence angle on downwind face θ_d and upwind face θ_u as function of global incidence angle ϑ . Open symbols: data taken from figure 4.4 of reference [79].

angle of the maximum sputtering yield) are the only stable ones if merely the dependence of the sputtering yield $Y(\theta)$ on θ is taken into account for modeling surface evolution. In striking contrast to these predictions, in the $\vartheta = 75^\circ$ high fluence regime, the local incidence angle on the upwind face is $\theta \approx 50^\circ$, far away from both, the maximum of the sputtering yield at $\theta = 72^\circ$, as calculated with TRIM.SP[41], and from $\theta = 0^\circ$. Likewise, the local incidence angle on the downwind face is $\theta \approx 82^\circ$, distinctly different from 90° . Consequently, the local incidence angles of the faces in the $\vartheta = 75^\circ$ high fluence regime cannot be explained by the theory of Carter, Colligon, and Nobes [19].

Carter [18] explained the formation of sawtooth profiles by grazing incidence ion bombardment with geometric shadowing. Later this mechanism was used by Gago et al. [52] for low energy and by Datta and Chini [37] for medium energy ions to explain the same morphology. Shadowing sets in when the steepest slope of the downwind face is parallel to the ion beam. Indeed, as visible in the height profile of Fig. 5.8(i) with the properly indicated ion beam direction, at the end of the 75° low fluence regime the downwind face occasionally reaches a local slope angle of 15° , making this part of the surface parallel to the ion beam. Therefore, instead of assuming the onset of ion reflection to be decisive for the transition to the high fluence regime, one might argue that the onset of geometric shadowing is the decisive effect.

In chapter 5.2 and 5.3 we found that $\alpha_d = 8^\circ$ for the high fluence regimes at both incidence angles $\vartheta = 63^\circ$ and $\vartheta = 75^\circ$. This seems to indicate that α_d is pinned to the flat surface orientation rather than to the ion beam direction. To analyze this in more detail, the local incidence angles θ_u , θ_d from the experiments presented here (filled symbols) and from the dissertation of Macko [79] (open symbols) are plotted as function of the global incidence angle ϑ in figure 5.10. The dashed line indicates the global incidence angle ϑ . Indeed, the local incidence angle on the downwind face evolves with a fixed angular separation of 8° with respect to ϑ for $63^\circ \leq \vartheta \leq 77^\circ$. This separation is the

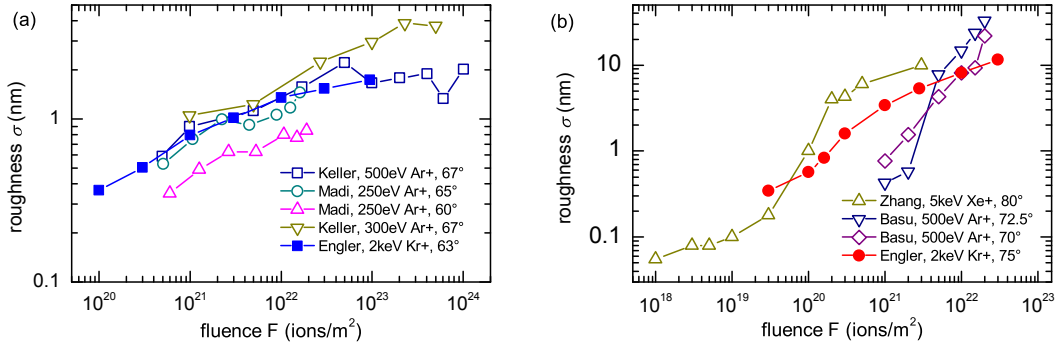


Figure 5.11.: Roughness σ as a function of ion fluence F for ion exposure of Si(001) under various ion beam conditions. (a) Experimental data by Keller et al. [71] and Madi, George, and Aziz [86] suitable for comparison to the $\vartheta = 63^\circ$ data of the present study in the ripple pattern range. (b) Experimental data by Basu, Datta, and Som [3] and Zhang et al. [144] suitable for comparison to the $\vartheta = 75^\circ$ data of the present study in the roof-tile range.

local slope α_d . Therefore, in this angular range there is a magic downwind surface slope, independent of the ion beam incidence angle ϑ . For smaller ϑ the separation is a little lower ($\approx 6^\circ$), possibly because pattern saturation is not yet reached. On the upwind face, the local incidence angle scatters. It is less well defined due to the broader angular distribution on this face (compare Fig. 5.4 and Fig. 5.8). Nevertheless, the local incidence angle apparently remains fixed at $\theta_u \approx 50^\circ$. This implies a simultaneous increase of the upwind surface slope α_u and ϑ . In conclusion, the upwind face is pinned to the ion beam direction, while the downwind face is pinned to the global surface orientation. This pinning pinned to the global surface orientation rather than the ion beam direction appears to be hardly compatible with the relevance of geometric shadowing.

As a last issue, one might hypothesize, that by prolonged ion exposure beyond the maximum fluence of $F = 9.5 \times 10^{22}$ ions/m² used in this study, it could be possible to transform the ripple pattern at $\vartheta = 63^\circ$ into a roof tile pattern. A rational basis for such a hypothesis could be seen in the fact that for both angular ranges the low fluence regime is similar, dominated by a parallel mode ripple pattern. However, the hypothesis appears unlikely to be valid, when considering that the key difference between the two high fluence regimes is ion reflection and the sputtering associated with it which leads to the formation of the roof-tile structure for $\vartheta = 75^\circ$. The stable local incidence angles at $\vartheta = 63^\circ$ (compare Fig. 5.6(d)) together with a negligible flux enhancement on the upwind face (a factor of 60 smaller as for the $\vartheta = 75^\circ$ case, according to our calculations) suggests the Hauffe mechanism to be largely inoperative at $\vartheta = 63^\circ$. On a more descriptive level, the wavelength λ , the parallel mode ripple pattern roughness σ_s , and the local incidence angles $\theta_{d/u}$ are stationary at the end of the investigated fluence range for $\vartheta = 63^\circ$. There is no indication that this behavior will change.

To obtain a quantitative insight on how well the results of various ion beam exposure experiments of Si(001) match and how strongly they depend on ion beam parameters,

5.4. Discussion

we collected data from literature [3, 21, 71, 86, 144] for the angular ranges of ripple and roof-tile pattern formation and display them in Fig. 5.11. As no two data sets represented in Fig. 5.11(a) and (b) agree in all parameters (incidence angle ϑ , ion species, ion energy), no perfect agreement can be expected between any of the experiments. As an additional note of caution, it should be remarked that all groups [3, 21, 71, 86, 144] conducted their erosion experiments for samples with a native oxide layer. Sputtering SiO_2 rather than Si at low fluences (up to a few 10^{19} ions/m²) may affect the initial stages of the morphological evolution.

We start with a discussion of Fig. 5.11(a), where roughness data is compared to our $\vartheta = 63^\circ$ sequence in the ripple pattern range. Despite some experimental scatter, it is obvious that the roughness data from Keller et al. [71] for 500 eV Ar^+ at $\vartheta = 67^\circ$ match surprisingly well to our measurement with 2 keV Kr^+ at $\vartheta = 63^\circ$. Moreover, Keller et al. [71] observed the same sequence of patterns as we did. First a parallel mode ripple pattern evolves. Then, simultaneously with the saturation of this mode, beyond a critical fluence a disordered perpendicular mode develops, which eventually dominates the roughness. Just the critical fluences for the onset of the disordered perpendicular mode are substantially higher for 300 eV and 500 eV Ar^+ exposure compared to 2 keV Kr^+ . The sequence of patterns observed by Castro et al. [21] for 500 eV Ar^+ at $\vartheta = 65^\circ$ is again identical to the one observed by us, but unfortunately the authors do not provide quantitative roughness data that could be represented in Fig. 5.11(a). Madi, George, and Aziz [86] vary the fluence of 250 eV Ar^+ ions only by a factor of 30. The roughness evolution at $\vartheta = 65^\circ$ matches quite well with our results for 2 keV Kr^+ at $\vartheta = 63^\circ$. However, apparently the roughness develops non-monotonic with ion fluence. No topographic images are shown and thus a straightforward comparison to our patterns is not possible.

In figure. 5.11(b) roughness data in the roof-tile pattern range is compared to our $\vartheta = 75^\circ$ sequence. The data set of Zhang et al. [144] for 5 keV Xe^+ at $\vartheta = 80^\circ$ displays a similar S-shaped roughness curve as our data for 2 keV Kr^+ at $\vartheta = 75^\circ$. The S-shape of the roughness curve is lesser pronounced for the data for 500 eV Ar^+ at $\vartheta = 72.5^\circ$ of Basu, Datta, and Som [3]. Specifically, also for 5 keV Xe^+ the low fluence regime may be fitted rather well through an exponential growth of the roughness, as for 2 keV Kr^+ . In both studies [3, 144] the sequence of the morphologies is qualitatively similar to our study at $\vartheta = 75^\circ$. Parallel mode ripples transform into a roof tile morphology with the tips of the roof tiles pointing into the ion beam direction. In all cases the evolution of the roof-tile pattern is accompanied by strong coarsening. The fluence of the transition from the low fluence ripple to the high fluence roof-tile pattern determined in our experiments almost agrees quantitatively with the fluence from the study of Zhang et al. [144]. Despite these similarities, figure 5.11(b) shows also notable differences in roughness evolution for the different data sets. Zhang et al. [144] measured surprisingly low roughnesses down to $\sigma = 0.06$ nm for very low fluences, where the sample morphology is possibly affected by

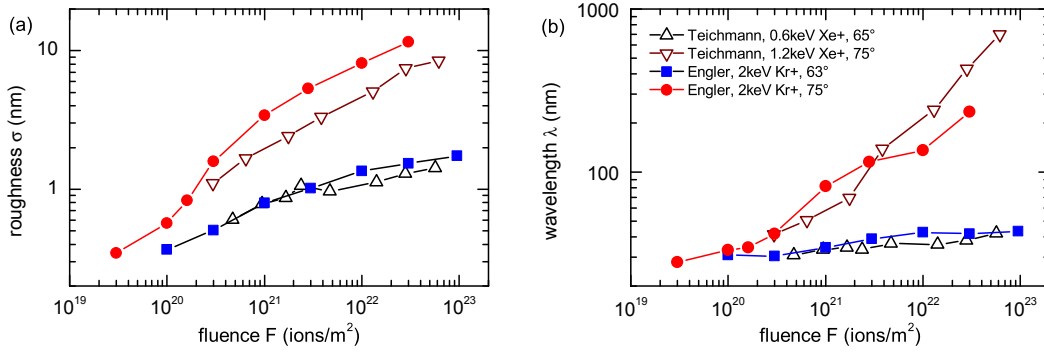


Figure 5.12.: Evolution of (a) roughness σ and (b) wavelength λ of ion beam induced patterns on Si and Ge (Teichmann et al. [131]) as function of fluence.

SiO₂. Although Basu, Datta, and Som [3] only vary the ion fluence by a factor of 20, their roughness increases for 500 eV Ar⁺ at $\vartheta = 72.5^\circ$ by a factor of ≈ 80 which is more than in our experiments, where the ion fluence is varied by a factor of 1000 and the roughness increased by a factor of ≈ 35 .

Recently, Teichmann et al. [131] demonstrated the entire absence of pattern formation on Ge(001) after low energy Ne⁺ or Ar⁺ exposure. This raises the question, whether Si and Ge behave entirely different under ion beam exposure due to differences in their material properties. Therefore we compare in figure 5.12(a) and (b) our data for the evolution of roughness and wavelength, respectively, with the corresponding data of Teichmann et al. [131] for 600 eV Xe⁺ at $\vartheta = 65^\circ$ and 1.2 keV Xe⁺ at $\vartheta = 75^\circ$. Their fluences are scaled by $\cos \vartheta$ as they were originally stated with respect to a plane perpendicular to the ion beam. For the ripple pattern range we have to compare the 600 eV Xe⁺ at $\vartheta = 65^\circ$ data set with our 2 keV Kr⁺ at $\vartheta = 63^\circ$ sequence. Figure 5.12 immediately tells that the evolution of roughness and of wavelength, especially its magnitude and constancy, are strikingly similar for both data sets. Also the morphological evolution, which can be seen in the AFM topographs shown by Teichmann et al. [131], is very similar. First a parallel ripple mode evolves and saturates, then beyond a critical fluence a disordered perpendicular mode develops on top of it, which eventually dominates the surface roughness. The disordered perpendicular mode develops at a fluence of $F \approx 2 \times 10^{21}$ ions/m² close to the fluence $F \approx 3 \times 10^{21}$ ions/m² observed here for Si. For the roof-tile range, Figure 5.12 compares the 1.2 keV Xe⁺ at $\vartheta = 75^\circ$ data set for Ge(001) with our 2 keV Kr⁺ at $\vartheta = 75^\circ$ sequence for Si(001). Both data sets display similar roughness and wavelength evolution, although the absolute numbers differ, not unexpectedly. Based on the AFM data of Teichmann et al. [131], we can conclude that the evolution is similar to the Si one, even quantitatively. The low fluence parallel ripple mode is followed by the evolution of a roof-tile structure, which is accompanied by strong coarsening and disordering. Finally, we note that also for Ge the smooth flat surface morphology for incidence angles ϑ below the onset of ripple pattern formation exists. Even the grazing

morphology with faint grooves in ion beam direction for grazing incidence beyond the roof-tile pattern is observed on Ge (compare Ref. [81] for Si).

We conclude that the angular ranges of ripple pattern and roof-tile pattern formation, as well as the regimes of low fluence and high fluence are a universal feature in ion beam erosion of Si and Ge surfaces.

Conclusions

The evolution of the morphology of Si(001) under 2 keV Kr⁺ ion bombardment is different at $\vartheta = 63^\circ$ in the ripple pattern range and at $\vartheta = 75^\circ$ in the roof-tile pattern range. At both incidence angles a low and a high fluence regime could be identified. While the low fluence regime is similar for both, the evolution in the high fluence range differs qualitatively.

The similar pattern evolution in the low fluence range may be approximated by a linear model for both incidence angles, as the ripple pattern wavelength is nearly fixed, the pattern order improves, and the surface roughness grows approximately exponentially.

For 63° an ordered parallel mode ripple pattern evolves in the low fluence regime. The ripple amplitude of this pattern saturates and the ripple shape gets stationary. In the high fluence regime, $F \geq 3 \times 10^{21}$ ions/m², the parallel mode ripples are saturated and a disordered long wavelength perpendicular mode evolves which eventually dominates the morphology and roughness of the surface. The saturation of the parallel mode ripples and the emergence of the perpendicular mode can be described by a non-linear model, like the anisotropic Kuramoto-Sivashinsky equation [34, 70].

Also for 75° an ordered parallel mode ripple pattern evolves in the low fluence regime. In the high fluence regime starting already at $F \approx 1 \times 10^{21}$ ions/m², the initial ripple pattern transforms rapidly into a roof-tile morphology of extended, flat downwind faces and short, steep upwind faces. In this high fluence regime the morphology exhibits strong coarsening, disordering, and roughening. The evolution of the roof-tile morphology cannot be modeled by PDEs, as non-local effects dominate here. Most ions impinging the downwind face are reflected and hit the adjacent upwind face, enhancing the erosion there. Although the details of the evolution are not understood yet, this non-local mechanism, known as Hauffe mechanism, causes the rapid coarsening and disordering.

Apparently, geometric shadowing is not responsible for the evolution of the roof-tile morphology, as the local incidence angle on the downwind face is always well below 90° in the high fluence regime. Unexpectedly, the downwind face's slope is fixed to $\alpha \approx 8^\circ$ in the roof-tile range, independent of the incidence angle ϑ . The upwind face in contrast is pinned to ion beam direction, i. e. the local incidence angle is always $\theta \approx 50^\circ$.

The different angular ranges of pattern formation, as well as different low fluence and high fluence regimes are not only universal for low energy ion beam erosion of Si, but also for Ge.

6. Pattern formation on crystalline Si(001)

The ion beam patterns observed on surfaces, which remain crystalline during ion bombardment, are different from the patterns observed on surfaces which amorphize during ion bombardment [24, 33, 67, 82, 92, 94, 116]. At elevated temperatures elemental semiconductors like Ge and Si do not amorphize during low energy noble gas ion bombardment unlike at room temperature [29, 72, 73, 79, 82, 107, 109]. On crystalline surfaces the Ehrlich-Schwoebel barrier at step edges introduces an additional instability mechanism (see chapter 2.4) [24]. This instability can lead to the formation of patterns under conditions where no pattern forms if the surface is amorphous [72, 73, 107]. For metal surfaces like Pt(111) which remain crystalline during ion bombardment this instability has been used to explain the observed patterns [24, 67, 94].

Studying the dependence of the surface morphology of Si(001) near the transition temperature, above which Si(001) is crystalline after ion bombardment, is essential to understand the pattern formation in the temperature regime for crystalline Si(001). Close above the transition temperature the roughness is maximal and strongly declines for higher temperatures. In this chapter the temperature dependence near the transition temperature for 2 keV Kr⁺ ions and the fluence dependence at the temperature of maximum roughening will be presented.

6.1. Temperature dependence

Figures 6.1 and 6.2 show Si(001) after 2 keV Kr⁺ normal incidence ion bombardment at elevated temperatures. For each temperature a 1.4 μm × 1.4 μm STM topograph is shown and below, a 45 nm × 45 nm detail image is shown, which is a linear combination of the original image and the Sobel filtered image (see chapter 3.5 for details). The insets display a LEED pattern of the surface. The arrows indicate the crystallographic directions in the STM images. The error of the temperature is ±10 K. For the first series of experiments (figure 6.1) an ion flux $\Phi = 4.8 \times 10^{17}$ ions/(s m²) and a fluence $F = 5 \times 10^{21}$ ions/m² was used. In this series, the temperature was measured with the old thermocouple (see chapter 3.2). After this series the thermocouple broke and has been replaced. With the new thermocouple the temperature dependence was measured using an ion flux $\Phi = 1.4 \times 10^{18}$ ions/(s m²) and a fluence $F = 4.7 \times 10^{21}$ ions/m² (figure 6.2).

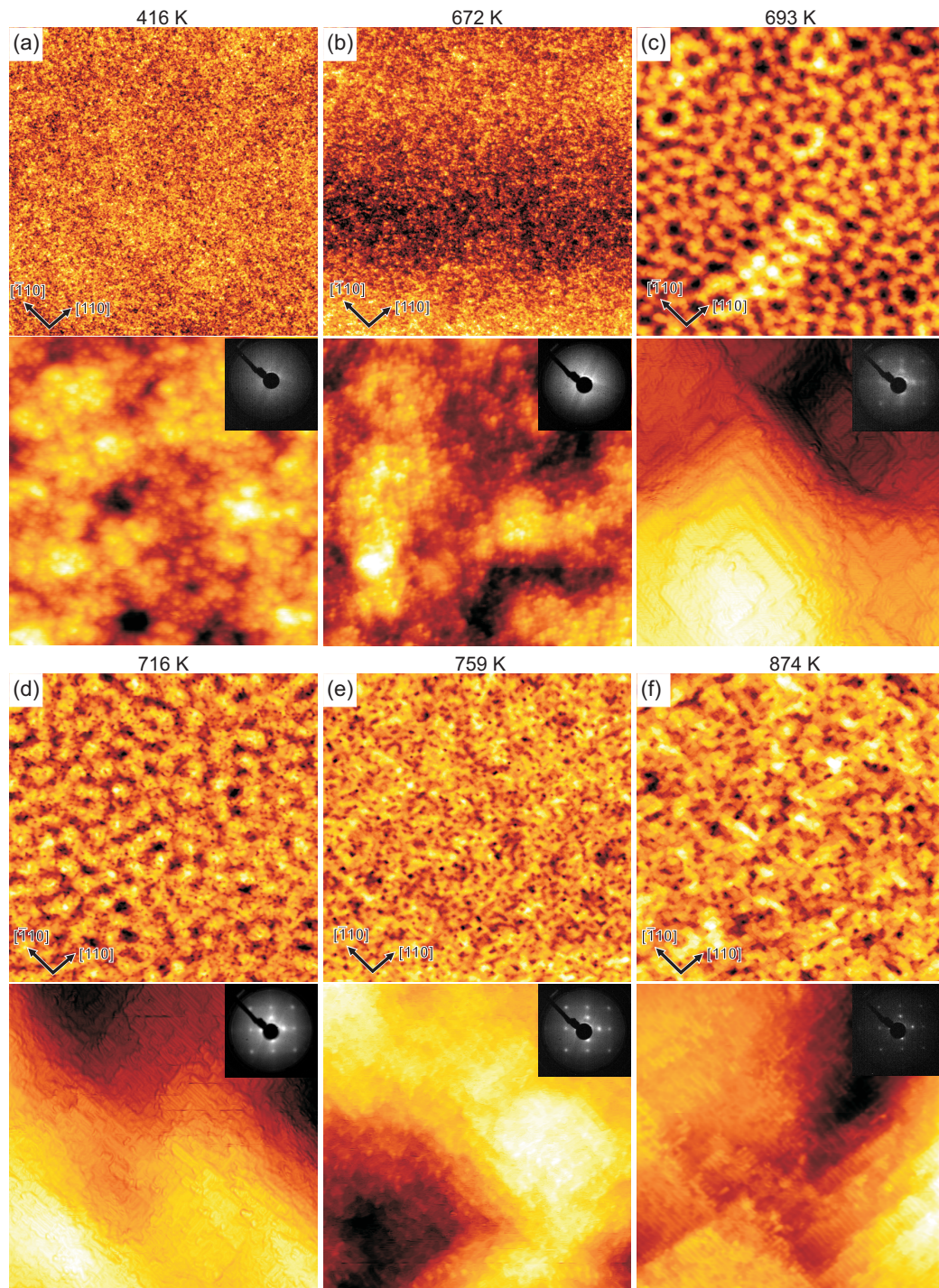


Figure 6.1.: Overview of temperature dependence measured with the old thermocouple. For each temperature a $1.4 \mu\text{m} \times 14 \mu\text{m}$ STM topograph is shown. The crystallographic directions are indicated by arrows. Below is a $45 \text{ nm} \times 45 \text{ nm}$ detail image, which is a linear combination of the topography and the Sobel filtered topography. The insets are LEED patterns at 66 eV electron energy. (a) 416 K, z-scale 1.5 nm, (b) 672 K, z-scale 1.5 nm, (c) 693 K, z-scale 17 nm, (d) 716 K, z-scale 8 nm, (e) 759 K, z-scale 3.7 nm, and (f) 874 K, z-scale 2.5 nm.

6.1. Temperature dependence

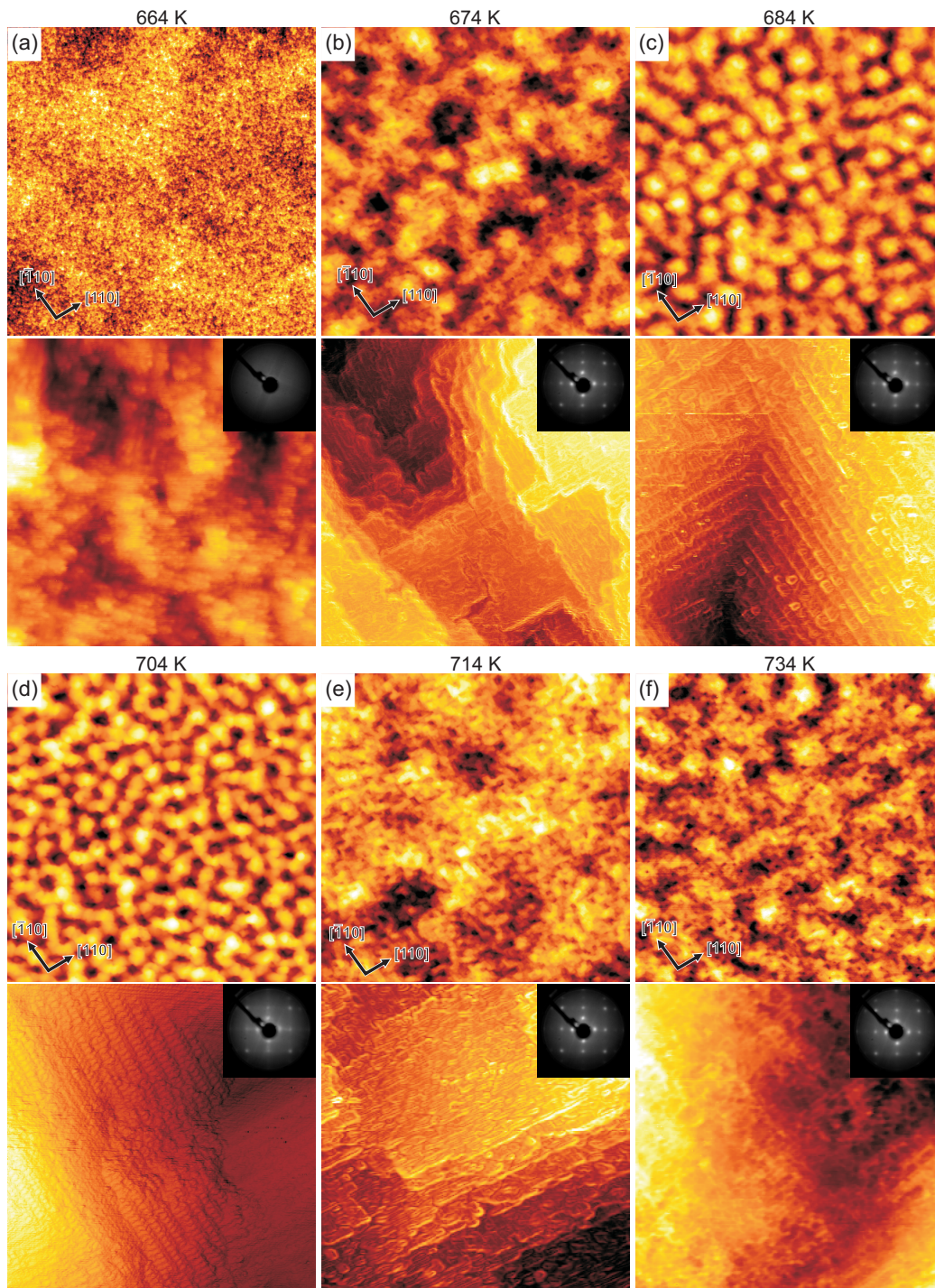


Figure 6.2.: Overview of temperature dependence measured with the new thermocouple. For each temperature a $1.4 \mu\text{m} \times 14 \mu\text{m}$ STM topograph is shown. The crystallographic directions are indicated by arrows. Below is a $45 \text{ nm} \times 45 \text{ nm}$ detail image, which is a linear combination of the topography and the Sobel filtered topography. The insets are LEED patterns at 66 eV electron energy. (a) 664 K, z-scale 1.3 nm, (b) 674 K, z-scale 6.4 nm, (c) 684 K, z-scale 9 nm, (d) 704 K, z-scale 16 nm, (e) 714 K, z-scale 3.4 nm, and (f) 734 K, z-scale 3.4 nm.

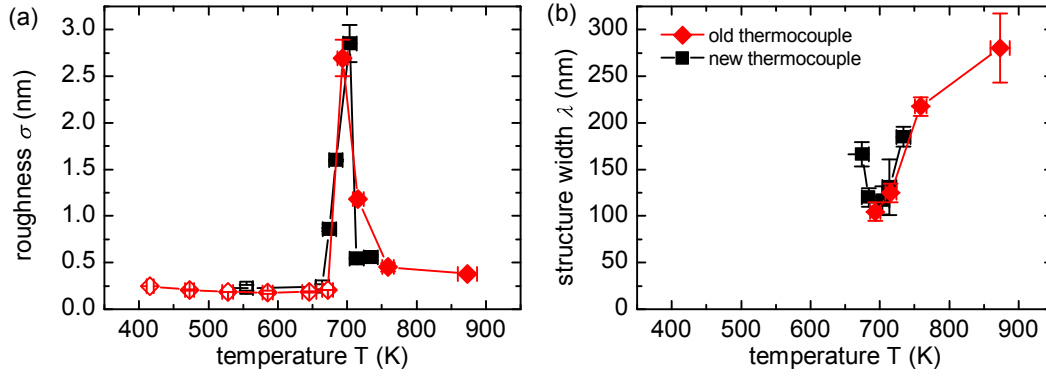


Figure 6.3.: Dependence of (a) roughness and (b) structure width on sample temperature during 2 keV Kr^+ ion bombardment. Data measured with both the old (red) and new (black) thermocouple are shown. Open symbols indicate amorphous and filled symbols crystalline surfaces.

In figure 6.3 the surface roughness σ and structure width λ are plotted as function of the temperature T during ion bombardment. Open symbols indicate amorphous and filled symbols crystalline surfaces. The values for both experiment series fit very good with the exception of the roughness at $T = 716$ K in the old and $T = 714$ K in new series.

There is a transition in the evolution of the surface during ion bombardment at $T = 674$ K. For temperatures below the surface (figures 6.1(a), (b), and 6.2(a)) is amorphous with a low roughness $\sigma \approx 0.2$ nm. While for $T \geq 674$ K the surface is crystalline with the characteristic 2×1 dimer reconstruction of Si(001), which can be seen in the LEED patterns and the detail STM images. The step edges visible in STM run predominantly along the $\langle 110 \rangle$ directions. Above the transition temperature the surface roughness increases dramatically with temperature as there is a sharp peak in surface roughness at $T \approx 700$ K with $\sigma = 2.8$ nm. This maximum of the surface roughness corresponds to a minimum of the structure width $\lambda = 120$ nm. With further increasing temperature the surface roughness decreases to $\sigma \approx 0.4$ nm for $T > 750$ K. The structure width increases with increasing temperature for $T > 700$ K to $\lambda = 280$ nm at $T = 874$ K.

In the temperature range from 684 K to 704 K, the surface exhibits a morphology of pyramidal mounds and pits. The surface has a short range order, but no long range order. The bases of these pyramids are oriented along the $\langle 110 \rangle$ directions. At 684 K the slopes of the mounds and pits have angles of 5° to 10° to the global surface plane, which can be seen by the broad peaks in the slope angle distributions (figure 6.9(c)). The steep slopes are composed of narrow, ≈ 2 nm wide terraces with dimer rows running perpendicular to the step edges separated by double steps of D_B type (see detail image of figures 6.2(c), (d)). At $T \approx 700$ K (figures 6.4(c), 6.9(d)) the angles of the slopes in $\langle 110 \rangle$ direction can be larger up to 15° to 25° while the peak between 6° and 10° is still present. At this temperature the slopes are not only composed of short terraces with double steps but also of step bunches (see detail images of figures 6.2(c) and 6.2(d)). The inclination of

6.1. Temperature dependence

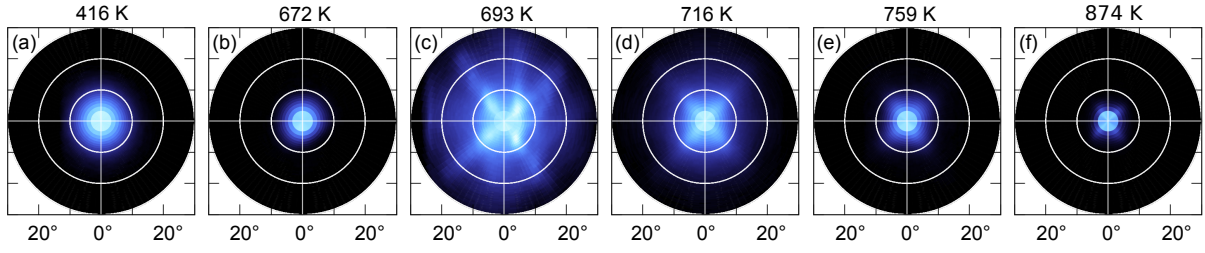


Figure 6.4.: Distribution of slope angles of series with old thermocouple (figure 6.1)

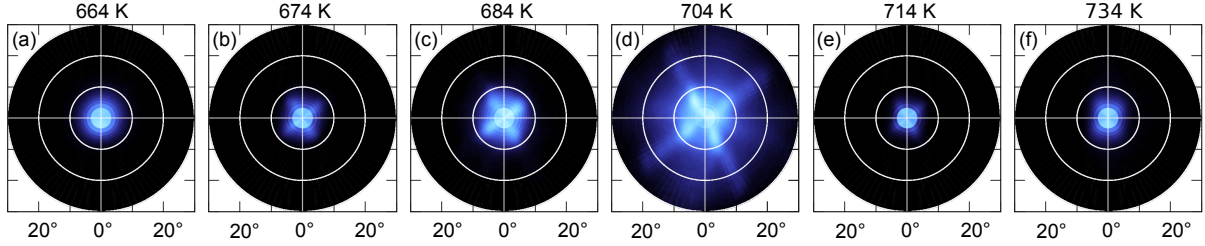


Figure 6.5.: Distribution of slope angles of series with new thermocouple (figure 6.2)

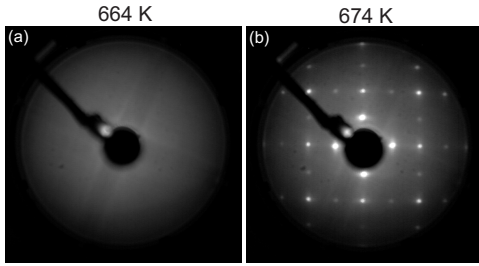


Figure 6.6.: LEED patterns at 66 eV electron energy after annealing of ion beam amorphized Si(001) for 30 min at (a) 664 K and (b) 674 K.

the step bunches is $\approx 20^\circ$. In addition to the slopes in $\langle 110 \rangle$ direction of the pyramids, slopes approximately in $\langle 100 \rangle$ direction can be seen in the slope distributions. These slopes correspond to short ridges between neighboring pyramids in figures 6.1(c) and 6.2(d). The morphology at $T \approx 715$ K differs between both experimental series. In the first series (figure 6.1(d)) the surface displays a pit and mound morphology with a roughness of $\sigma = 1.2$ nm. In the second series (figure 6.2(e)) the surface is flat with a roughness of $\sigma = 0.5$ nm. For higher temperatures the surface is flat with a roughness of $\sigma = 0.5$ nm.

To understand better why the surface is crystalline after sputtering at temperatures $T \geq 674$ K also annealing of Si(001) amorphized by ion bombardment at room temperature was studied with LEED (figure 6.6). For each annealing experiment a sample was amorphized with a fluence $F = 8.4 \times 10^{20}$ ions/m² of 2 keV Kr⁺ ions at $\vartheta = 30^\circ$ incidence angle. After ion bombardment the samples were annealed at (a) 664 K and (b) 674 K for 30 minutes. After annealing the LEED patterns were recorded. After annealing at 664 K the surface remains amorphous, while after annealing at 674 K the surface has recrystallized, which is shown by the sharp diffraction spots. The transition temperature above which the surface is crystalline in the sputtering experiments is in the range between

664 K and 674 K. The temperatures at which the surface remains crystalline during sputtering and the temperature at which an ion beam amorphized surface recrystallizes during annealing are the same.

6.2. Fluence dependence

At $T = 704$ K the pattern is most pronounced and the roughness is maximal. We chose this temperature for measuring the fluence dependence of the surface evolution, as the fastest evolution can be expected at this temperature.

Figure 6.7 shows the evolution of Si(001) during 2 keV Kr^+ ion bombardment at $T = 704$ K. For each fluence in the top row a $1.4 \mu\text{m} \times 1.4 \mu\text{m}$ STM topograph is shown. Below linear combinations of the topographies with Sobel filtered images are shown except for figure 6.7(a) where all images are topographies. The image size in the middle row is $180 \text{ nm} \times 180 \text{ nm}$ for figure 6.7(a)–(c), and $360 \text{ nm} \times 360 \text{ nm}$ for figure 6.7(d)–(e). In the bottom row, the image size is always $45 \text{ nm} \times 45 \text{ nm}$ to show details. The evolution of roughness σ and structure width λ is shown in figure 6.3.

The roughness increases monotonically with ion fluence, while the coarsening of the structure width is interrupted between 1.5×10^{20} ions/ m^2 and 7.5×10^{20} ions/ m^2 . During ion bombardment a mound and pit morphology evolves. For low fluences $F \leq 4.0 \times 10^{21}$ ions/ m^2 the surface exhibits short range but not long range order. At the lowest fluence $F = 3.0 \times 10^{19}$ ions/ m^2 (figure 6.7(a)), the pits and mounds are still extremely shallow with 0.4 nm to 0.5 nm depth or height, respectively. The surface roughness is still dominated by a long wavelength background with a corrugation of ≈ 2 nm. The surface slopes are composed of terraces with alternating dimer row orientation separated by S_A and S_B step edges.

At the fluence $F = 1.5 \times 10^{20}$ ions/ m^2 (figure 6.7(b)), the surface is already dominated by the pit and mound structure with 1 nm to 4 nm depth or height, respectively. Like at $F = 3.0 \times 10^{19}$ ions/ m^2 , the surface is composed of terraces with alternating dimer row orientation separated by S_A and S_B step edges. The pits and mounds have an approximately rectangular shape with the edges along the $\langle 110 \rangle$ directions.

At the fluence $F = 7.5 \times 10^{20}$ ions/ m^2 (figure 6.2(c)), the mounds and pits are pyramidal. The slopes are formed by double steps separated by ≈ 2 nm wide terraces with the dimer row perpendicular to the step edges. At $F = 4.7 \times 10^{21}$ ions/ m^2 (figure 6.7(d)), the pyramidal mounds are short range ordered. The edges of the pyramid bases are oriented along the $\langle 110 \rangle$ directions. Neighboring mounds are connected by ridges running 30° – 50° to the $\langle 110 \rangle$ directions. The slopes are mostly composed of double steps separated by ≈ 2 nm wide terraces. The steeper parts of the slopes are step bundles.

At the fluence $F = 2.5 \times 10^{22}$ ions/ m^2 (figure 6.7(e)), the surface is dominated by a network of ridges running 30° – 50° to the $\langle 110 \rangle$ directions. On top of the ridges there are pyramidal mounds with the bases oriented along the $\langle 110 \rangle$ directions. The height

6.2. Fluence dependence

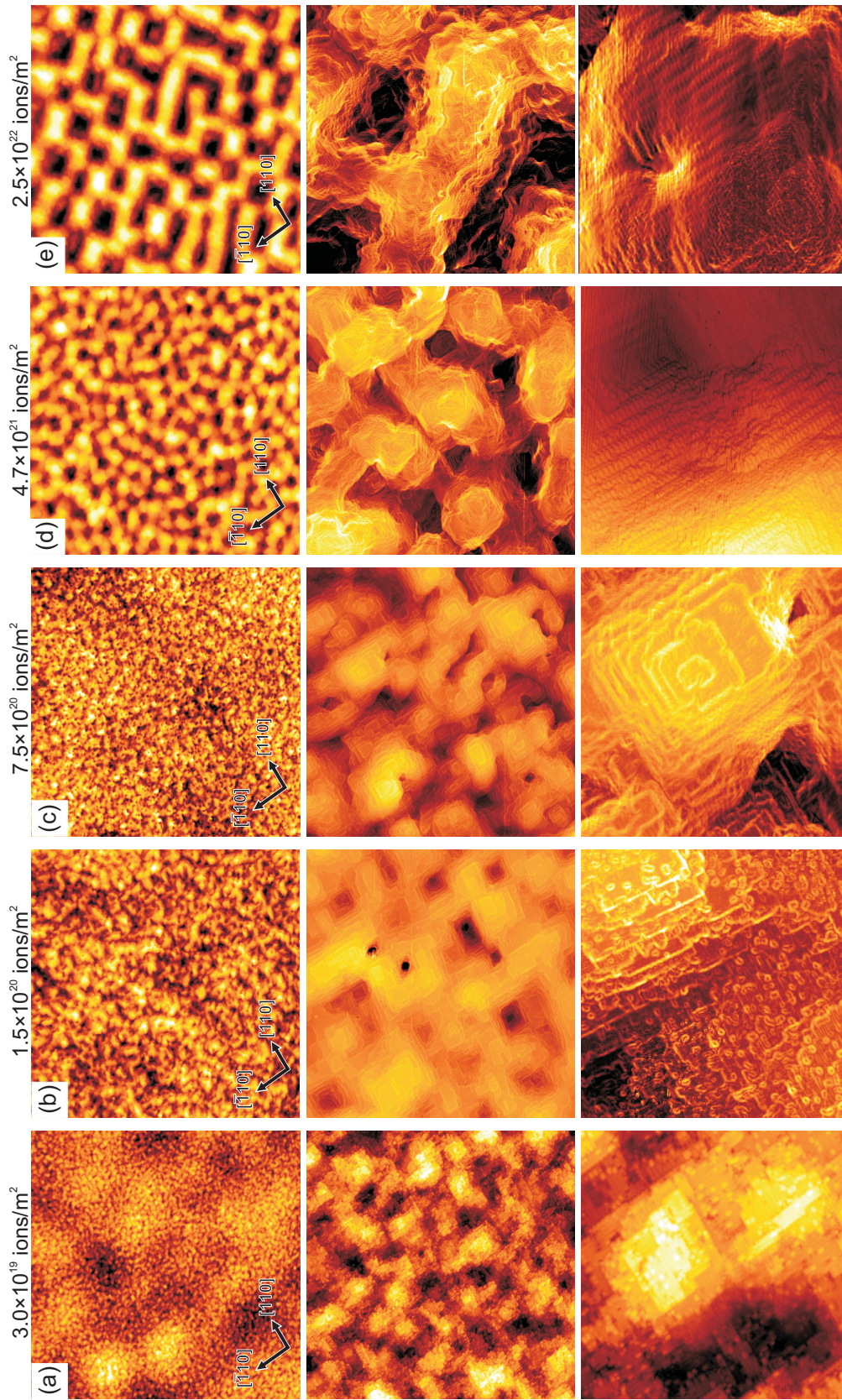


Figure 6.7.: Fluence dependence at $T = (704 \pm 10) \text{ K}$. For each fluence a $1.4 \mu\text{m} \times 1.4 \mu\text{m}$ STM topograph is shown. The z-scales are (a) 2.0 nm, (b) 2.3 nm, (c) 4.0 nm, (d) 16 nm, (e) 24 nm. The crystallographic directions are indicated by arrows. The fluences are shown above each column. The middle row displays (a)–(e) $180 \text{ nm} \times 180 \text{ nm}$ and (d)–(e) $360 \text{ nm} \times 360 \text{ nm}$ images. The bottom row 45 nm \times 45 nm images. For (a) all images are topographies. For (b)–(e) the images in the middle and bottom row are linear combinations of the topography and the Sobel filtered topography.

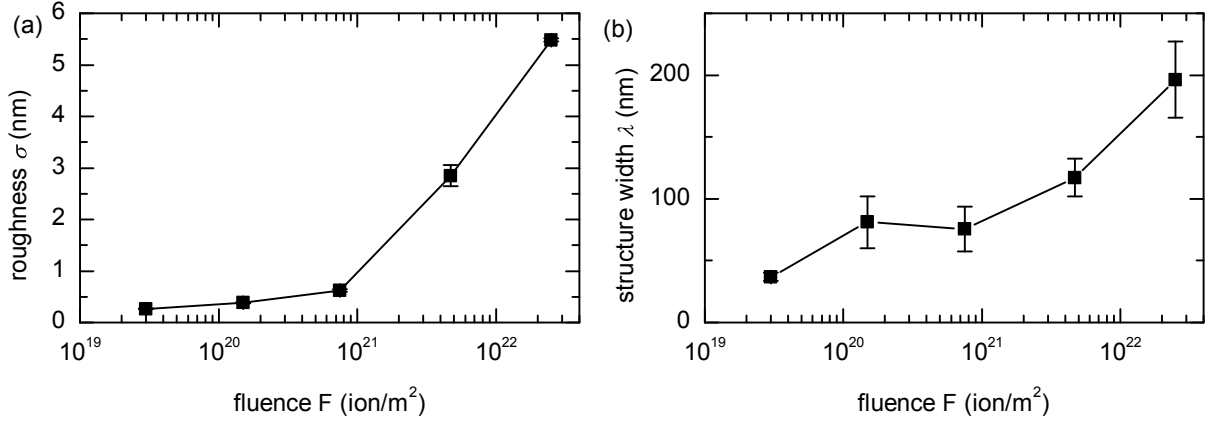


Figure 6.8.: Dependence of (a) roughness σ and (b) structure width λ on fluence at $T = (704 \pm 10)$ K.

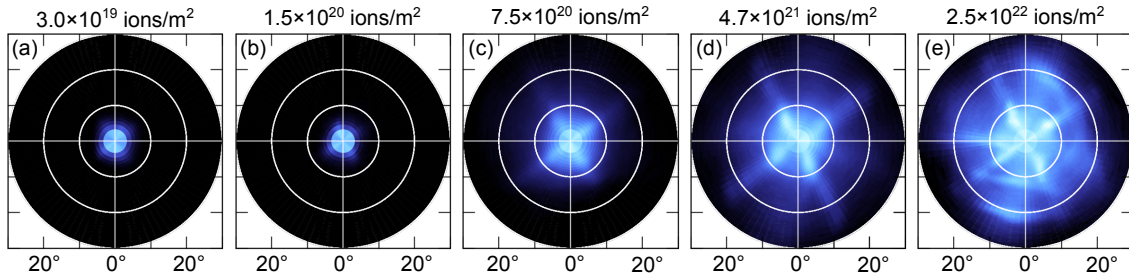


Figure 6.9.: Distribution of slope angles as function of the fluence at $T = (704 \pm 10)$ K.

difference between the valley and the ridges is ≈ 25 nm. On the $360 \text{ nm} \times 360 \text{ nm}$ image it can be seen that the step edges of the pyramids on top of the ridges are oriented along the $\langle 110 \rangle$ directions. The slopes of the ripple consist mostly of step bunches while the pyramids on top of the ridges also have double steps separated by ≈ 20 nm wide terraces.

Figure 6.9 shows the distributions of the slope angles as function of the ion fluence. For the low fluences $F \leq 1.5 \times 10^{20}$ ions/m^2 (figure 6.9(a)–(b)) the distribution is peaked at $\alpha = 0^\circ$ with small extensions in the $\langle 110 \rangle$ directions. At higher fluences (figure 6.9(c)–(e)) there are peaks in the $\langle 110 \rangle$ direction at $\alpha = 6^\circ$ to $\alpha = 8^\circ$. With increasing fluence the slopes in $\langle 110 \rangle$ direction get steeper, which can be seen by the extension from the peaks to larger slope angles. At the fluence $F = 4.7 \times 10^{21}$ ions/m^2 additional intensity near the $\langle 100 \rangle$ direction appears. With increasing fluence new peaks at $\alpha = 12^\circ$ and $\alpha = 20^\circ$ near the $\langle 100 \rangle$ directions evolve (figure 6.9(e)). These new peaks have a broad azimuth angle distribution.

6.3. Discussion

For crystalline surfaces, vacancies are expected to dominate the morphology evolution during ion bombardment. Due to sputtering more vacancies than adatoms are created on the surface. After recombination of the created defects vacancies remain which can diffuse until they annihilate at step edges or form immobile vacancy clusters on the terraces [67, 92, 94, 107].

Characteristic for Si(001) bombarded with ions at elevated temperatures is the transition from an amorphous surface to a crystalline surface above a critical temperature. In the flux range studied here, a flux dependence of the transition temperature cannot be established. For the time averaged ion flux $\Phi = 1.4 \times 10^{18}$ ions/(s m²) the transition is between 664 K and 674 K (compare figure 6.2), while for $\Phi = 4.8 \times 10^{17}$ ions/(s m²) the transition is between 672 K and 693 K (compare figure 6.1). This transition temperature coincides with the temperature required to recrystallize an ion beam amorphized surface by annealing for 30 min (compare figure 6.6). Likely, the surface has recrystallized before the start of ion bombardment for temperatures above 674 K, as the sample was held at constant temperature for 15 min to 60 min before ion bombardment (see chapter 3.3). The transition temperature was observed to be 520 K for Ge(100) under 1 keV Ar⁺ irradiation [107], and ≈ 670 K for Si(001) under 500 eV Ar⁺ irradiation with Mo co-deposition [109]. These results indicate that the transition temperature depends mainly on the substrate used and not on the ion beam parameters.

The roughness of Si(001) after ion bombardment as function of the temperature is peaked at $T \approx 700$ K, only 30 K above the transition from amorphous to crystalline. From the transition temperature to 700 K the surface roughness increases by more than a factor of 10 (compare figure 6.3(a)). For temperatures above 700 K the surface roughness decreases with temperature. For temperatures above 720 K the surface roughness σ is below 0.5 nm. That crystalline surfaces roughen only in a limited temperature range has already been observed for Ag(001) (200 K to 440 K), Ag(110) (180 K to 340 K) [33], Pt(111) (200 K to 500 K) [58] and Ge(001) (530 K to 700 K) [107]. For Si(001) this roughening range 674 K to 720 K is substantially narrower.

Pattern formation is driven by the Ehrlich-Schwoebel barrier. So the temperature dependence of the effective Ehrlich-Schwoebel current [133]

$$j_{\text{ES}} \propto D_{\text{S}} \left(1 - \exp\left(\frac{-E_{\text{ES}}}{k_{\text{B}}T}\right) \right) \quad (6.1)$$

has to be considered, which stems from the lower rate at which diffusing surface vacancies are incorporated into an ascending step compared to an descending step. Surface diffusion is a thermally activated process and $D_{\text{S}} \propto \exp(-E_{\text{D}}/(k_{\text{B}}T))$. Here E_{ES} and E_{D} are the Ehrlich-Schwoebel step edge barrier and the diffusion barrier, respectively. At temperatures just above transition from amorphous to crystalline the low diffusiv-

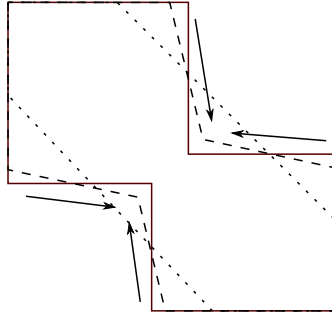


Figure 6.10.: Sketch of the pattern rotation for the case of two touching pyramids. The solid lines indicate the original shape of the pyramids. The dashed lines indicate the evolution of the edges. The ad-atom diffusion is indicated by the arrows.

ity D_S limits the destabilization due to the Ehrlich-Schwoebel current. With increasing temperature the Ehrlich-Schwoebel current is enhanced. At high temperatures the Ehrlich-Schwoebel barrier gets increasingly transparent with increasing temperature thus reducing the Ehrlich-Schwoebel current. So there is a temperature where the destabilization due to the Ehrlich-Schwoebel barrier has a maximum. The Ehrlich-Schwoebel current is $j_{ES} \propto \nabla h$ for small slopes [136]. For large slopes this approximation has to break down, as one cannot speak of step edges on a facet of a low index plane orientation. For these orientations the Ehrlich-Schwoebel current must vanish and these orientations are stable. Ou et al. [107] modeled the vanishing Ehrlich-Schwoebel current for a certain surface orientation by a third order polynomial in the surface slope $j_{ES,x/y} \propto (1 - \delta(\partial_{x/y}h)^2)\partial_{x/y}h$, where $1/\sqrt{\delta}$ is the selected surface slope.

For temperatures near 700 K the surface develops facets with slopes $\approx 8^\circ$. These facet orientations correspond to $\{1110\}$ facets. The facets are composed of ≈ 2 nm short terraces separated by D_B double steps, where the dimer rows are perpendicular to the step edge. The formation of D_B steps minimizes the free energy for short terraces [142]. A surface with only D_B steps is the observed equilibrium surface morphology of vicinal Si(001) surfaces with miscut angles larger than 6° [57, 139].

In the fluence dependent series, there are two fluence ranges where the morphology coarsens laterally: (a) $3 \times 10^{19} \text{ ions/m}^2 \leq F \leq 1.5 \times 10^{20} \text{ ions/m}^2$ and (b) $F > 7.5 \times 10^{20} \text{ ions/m}^2$. The coarsening in the low fluence range (a) might be caused by the short bombardment times of 22 s for $3 \times 10^{19} \text{ ions/m}^2$, which might be too short for the vacancy island to coalesce. At higher fluences there is enough time to develop a pattern with a stable structure width. Then the pattern amplitude increases with fluence without coarsening due to the Ehrlich-Schwoebel barrier. At the fluence $F = 7.5 \times 10^{20} \text{ ions/m}^2$ facets with slopes of 6° to 8° in the $\langle 110 \rangle$ directions (compare figure 6.9(c)) have evolved. Further growth of the pattern amplitude is associated with lateral coarsening in the fluence range (b). The peaks in the slope distribution in the $\langle 110 \rangle$ direction remain fixed, while small parts of the slopes get steeper.

An interesting observation is that the surface morphology changes from a surface with

6.3. Discussion

pyramidal mounds and pits with edges in $\langle 110 \rangle$ directions at $F \leq 4.7 \times 10^{21}$ ions/m² to a surface morphology of ridges and valleys, which are approximately parallel to the $\langle 100 \rangle$ directions, at $F = 2.5 \times 10^{22}$ ions/m². This change corresponds to a coarsening of the pattern (compare figure 6.8(b)). During coarsening neighbouring pyramidal mounds eventually touch. Although there is no long range order, it can be seen in figure 6.7(d) that the pyramids touch at their corners. Figure 6.10 sketches how the rotation of the pattern happens at the example of two touching pyramids. When two pyramids touch at their corners the chemical potential of atoms at corners touching another pyramid is lower than at the other corners. This leads to diffusion of atoms along the step edges to the site where the pyramids touch. The diffusing atoms lead to the formation of ridges. Diffusion parallel to the step edge is enhanced for atoms bound to a D_B step compared to atoms on the terrace. The activation energies are 0.38 eV and 0.76 eV for atoms bound to a D_B step and on the terrace, respectively [117]. For pyramidal pits, vacancies diffuse to sites where two pits touch leading to the formation of valleys. Both diffusion processes lead to formation ridges and valleys oriented approximately along the $\langle 100 \rangle$ directions. The formation of ridges and valleys can also be explained with an entropic argument. The ridges are rough in the sense that the step edges at the ridge slopes are alternating short step edges parallel to the $[110]$ and $[1\bar{1}0]$ directions, respectively, as seen in figure 6.7(e). The entropy of the rough ridge is larger than of two touching pyramids. The broad distribution of ridge directions can be understood by taking into account that the surface at 4.7×10^{20} ions/m² is only short range ordered. The distribution of directions between neighbouring pyramids is broad. This leads to the large spread in ridge directions in figure 6.7(e).

The pyramids on top of the ridges at $F = 2.5 \times 10^{22}$ ions/m² (figure 6.7(e)) are reminders of the pyramids at lower fluences. As they are higher than the ridges, there is no step edge running to a second pyramid, so the mechanism discussed above is not operative and the edges of the pyramids stay parallel to the $\langle 110 \rangle$ directions.

Conclusions

We observed the transition, above which Si is crystalline after 2 keV ion bombardment, at 674 K. Below Si amorphizes under ion bombardment and the surface remains flat. Above there is a narrow temperature range from 674 K to 720 K where the surface roughens strongly and a mound and pit morphology oriented along the $\langle 110 \rangle$ directions develops. The roughness as function of temperature has a pronounced maximum at 700 K. The crystallinity of the surface enables an additional mechanism for destabilizing the surface. The probability for incorporating vacancies into ascending step edges is lower than for incorporating into descending step edges, due to the Ehrlich-Schwoebel barrier. This effect induces an effective uphill mass current when vacancies are constantly produced by ion bombardment. The pattern developing near 700 K is short range ordered.

At $T \approx 700$ K first a pattern of pyramidal mounds and pits evolves. This pattern

coarsens with ion fluence once developed. For high fluences the morphology turns into a ridge and valley morphology where the orientation is rotated $\approx 45^\circ$ to the $\langle 110 \rangle$ directions. This pattern rotation is caused by coalescence of neighbouring mound and pits and diffusion along the step edges.

Ion beam pattern formation at elevated temperatures, where Si remains crystalline, is a method to produce patterns oriented along the crystallographic directions of the substrate.

7. Summary

In this thesis, ion beam pattern formation was studied under different conditions. Different types of patterns can be produced with ion beam pattern formation: e. g. ripples, dots, roof-tiles, pyramidal pits and mounds, or ridges and valleys.

Ion beam pattern formation at room temperature with simultaneous deposition of metals was analyzed in chapter 4. A metal must form a silicide to induce pattern formation by co-deposition during ion bombardment. Comparing pairs of metals with similar nuclear charge and mass, namely Ag–Pd and Pb–Ir, showed that the silicide forming metals Pd and Ir induce pattern formation, while non-silicide forming metals do not. This also showed that differences in collision kinetics are not responsible for pattern formation, as the pair Pb–Ir has almost twice the atomic mass than the pair Ag–Pd. Combining the results presented here with literature (see figure 4.19), shows that the stronger the tendency to silicide formation, i. e. the silicide contains less metal and the enthalpy of formation is larger, the stronger is the induced pattern formation. The formation of a silicide can reduce the erosion speed of the surface significantly, thus transforming chemical patterns into height differences.

The formation of clusters after exposing the Ag sputter co-deposition sample to air underlines the importance of in-situ measurements for understanding ion beam pattern formation.

Silicide formation of the deposited metal is necessary for metal induced ion beam pattern formation, however this is not sufficient. The metal to ion flux ratio needs to be in a certain range depending on the metal. For too low flux ratios the metal concentration in the surface near layer is too low for silicide formation. While too high flux ratios can suppress pattern formation as the Fe co-evaporation experiments (figure 4.17) show. For high flux ratios a metal concentration large enough to form a closed silicide layer builds up before a morphological pattern evolves. The deposition geometry is another important parameter for pattern formation. The larger the angle between metal flux and ion flux the stronger is the pattern formation (figure 4.18).

Neither mechanism proposed for silicide induced pattern formation, based on a geometrical instability or on phase separation, respectively, can explain all observed phenomena on their own. Instead one has to realize that both mechanisms can amplify each other.

Sputter co-deposition is useful as a quick test whether a metal can induce pattern formation. For a detailed analysis of the mechanisms, co-evaporation experiments provide more controlled conditions which ease the analysis of the data.

Ion beam pattern formation at room temperature without impurities was studied in

chapter 5. Patterns evolve for ion incidence angles larger than a critical angle between 55° and 58° . Between 58° and 63° a ripple pattern evolves. Amplitude and quality of the ripple pattern increase gradually with the incidence angle. At $\vartheta = 63^\circ$ the pattern is best developed.

The evolution of the pattern with increasing fluence was studied at the incidence angles $\vartheta = 63^\circ$ and $\vartheta = 75^\circ$ in the ripple and roof-tile pattern range, respectively. Two fluence regimes can be distinguished for both incidence angles (compare tables 5.1 and 5.2). The transition from the low fluence regime to the high fluence regime is gradual. The low fluence regime is similar for both incidence angles. A ripple pattern with wave vector parallel to the ion beam direction evolves, which exhibits only little lateral coarsening. The pattern evolution in this regime can be approximated by a linear model. In the high fluence regime the surface evolution can only be described by taking non-linear effects into account. The pattern evolution differs qualitatively for both incidence angles in the high fluence regime. At $\vartheta = 63^\circ$ the parallel ripple mode saturates and a disordered perpendicular mode emerges. This perpendicular mode eventually dominates the surface roughness. For $\vartheta = 75^\circ$ the surface develops a roof-tile pattern with well defined downwind faces. The ions hit the downwind faces at an grazing local incidence angle $\theta \approx 82^\circ$. Thus, a large portion of the incident ions are scattered onto the next upwind face. This non-local effect proposed by Hauffe [60] leads to strong coarsening and disordering of the surface.

By comparing with literature, we can conclude that different angular ranges and the existence of a low and high fluence regime are universal for ion beam pattern formation of Si with different ion species and energy, as well as for Ge.

Ion beam pattern formation at elevated temperatures, where Si remains crystalline, was studied in chapter 6. For 2 keV Kr^+ ions the temperature above which Si remains crystalline is $T = (674 \pm 10)$ K. In a narrow temperature range from the transition temperature to 720 K the surface roughens and develops a pit and mound morphology. Near 700 K the pits and mounds are pyramidal, surface roughness is maximal and facets with well defined slopes develop.

The fluence dependence of pattern formation was studied at $T = (704 \pm 10)$ K. For fluences below 7.5×10^{20} ions/m² the surface develops a pit and mound morphology with the edges parallel to the $\langle 110 \rangle$ directions. The pits and mounds are pyramidal at $F = 7.5 \times 10^{20}$ ions/m². With increasing fluence the pits and mounds coarsen. This coarsening leads to the formation of ridges and valleys which are $\approx 45^\circ$ rotated to the $\langle 110 \rangle$ directions. The rotation of the ridges and valleys is caused by diffusion along the step edges.

8. Outlook

This thesis contributes to a better understanding of ion beam pattern formation. Nevertheless it raises new questions worth investigating.

Although Ag and Pb co-deposition do not induce pattern formation under the conditions studied here, it is worth investigating if they may induce pattern formation under extreme conditions, like very high metal fluxes, a large angle α between ion beam and metal flux, and an ion incidence angle ϑ close to the critical angle, above which pattern formation occurs in absence of impurities.

Metals forming disilicides or trisilicides are good candidates for testing on pattern formation. They will likely induce pattern formation. Testing metals, which form these silicides and are relevant for applications, like Co [66] for their ability to induce pattern formation, can be rewarding and open routes to produce nano-structured silicide films.

From a more fundamental point of view in-vivo studies of both surface morphology and composition modulation are desirable. These studies could provide insight in how exactly morphology and chemical composition are coupled. In-vivo studies of morphological evolution have been performed already with microscopic [2, 55] and X-ray scattering [6, 108, 109] techniques.

Non-local effects like reflected ions hitting the sample again at distant locations need further attention. The effect of reflected ions needs to be included into theoretical models like the effect of redeposited atoms [38]. As input parameters the angular and energetic distributions of the reflected ions are needed. Measuring these distributions as function of the incidence angle will aid the theoretical modelling.

Over a broad range of incidence angles the upwind faces are fixed to the ion beam, i. e. the local incidence angle is fixed at $\theta_u \approx 50^\circ$, while at the downwind face the slope $\alpha_d \approx 8^\circ$ is fixed. More fluence dependent studies at different angles and at larger fluences would show if this is an effect of the limited fluence. However we expect the slope angles to be stable, based on the experiments presented here. Also experiments with different ion species and energy can show if this is an universal result.

Ion bombardment at temperatures, at which Si remains crystalline, produces patterns oriented to the crystallographic directions for normal incidence. Substrates with a symmetry different from Si(001) should yield patterns corresponding to their symmetry. It is also interesting if the patterns are oriented with the crystallographic direction for all incidence angles or if for oblique incidence the pattern is oriented with the ion beam.

A. Numerical modelling of sputter co-deposition fluxes

For numerical modelling a rectangular target with width W , height H , and height H_0 of the lower edge was used (figure A.1). The target is divided into rectangular surface elements $\Delta A_t(y_k, z_l)$ centered at $(x = 0, y_k, z_l)$ with width Δy and height Δz . The flux Φ on a target surface element $\Delta A_s(x, y)$ centered at $(x, y, z = 0)$ is calculated by summing the fluxes $\Phi_{k,l}$ from all target surface elements $\Delta A_t(y_k, z_l)$. The substrate surface element $\Delta A_s(x, y)$ covers the solid angle

$$\Omega_{k,l}(x, y) \approx \frac{\Delta A_s(x, y) \cos \theta_s}{d_{k,l}^2} \quad (\text{A.1})$$

seen from the center of $\Delta A_t(y_k, z_l)$. Here $d_{k,l} = \sqrt{x^2 + (y - y_k)^2 + z_l^2}$ is the distance between the target and substrate surface element and $\theta_s = \arccos(z_l/d_{k,l})$ is the local incidence angle.

With the differential yield $dY/d\Omega(\theta_t, \varphi_t)$ and the ion flux Φ_t onto the target the flux

$$\Phi_{k,l} \approx \Phi_t \Omega_{k,l}(x, y) \frac{\Delta A_t(y_k, z_l)}{\Delta A_s(x, y)} \frac{dY(\theta_t, \varphi_t)}{d\Omega} \quad (\text{A.2})$$

onto the substrate can be calculated. The emission direction is given by the polar angle $\theta_t = \arccos(x/d_{k,l})$ with respect to the target normal and the polar angle $\varphi_t = \arctan((y_k - y)/z_l)$ with respect to the negative z -axis.

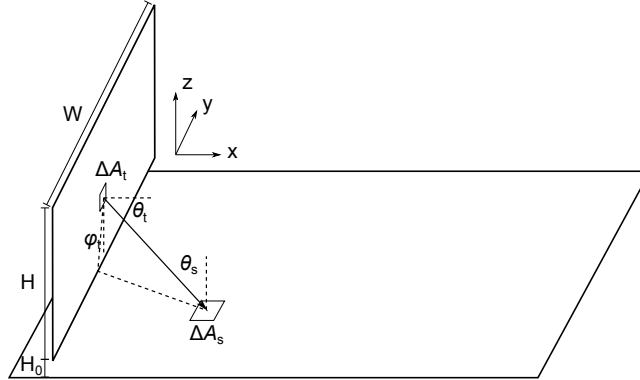


Figure A.1.: Sketch of sputter co-deposition

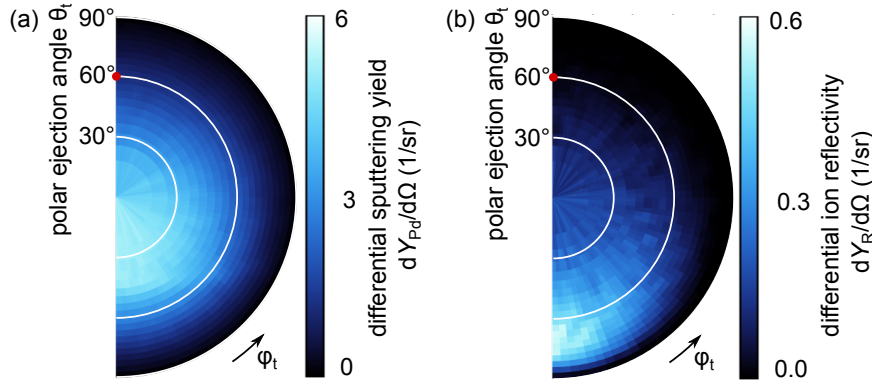


Figure A.2.: Differential Pd sputtering yield $dY_{\text{Pd}}/d\Omega$ (a) and ion reflectivity $dY_{\text{R}}/d\Omega$ (b) for 2 keV Kr^+ ions at 60° incidence angle with respect to the target normal. The direction of the incident ion beam is indicated by a red dot.

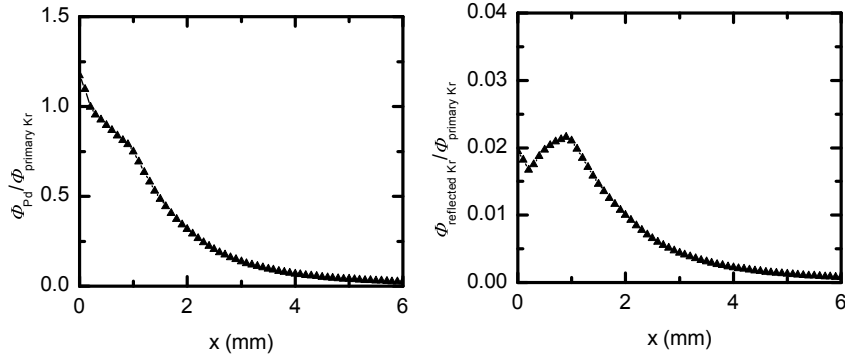


Figure A.3.: Relative Pd flux $\Phi_{\text{Pd}}/\Phi_{\text{primary Kr}}$ (a) and secondary Kr^+ flux $\Phi_{\text{reflected Kr}}/\Phi_{\text{primary Kr}}$ (b) as function of the distance to the target x .

TRIM.SP outputs the number of atoms sputtered and ions reflected into the different direction as 2d histograms $N_{n,m}$. The limits of polar angle intervals $[\theta_n, \theta_{n+1})$ are given by $\theta_n = \arccos(1 - n/20)$ with $n = 0, \dots, 20$. The width of the azimuth angle intervals $[\varphi_m, \varphi_{m+1})$ is 3° . The solid angle covered by one bin of the histogram is $\Omega = 2.62 \text{ msr}$. For N ion impacts simulated with TRIM.SP the differential yield is given by

$$\frac{dY(\theta, \varphi)}{d\Omega} \approx \frac{N_{n,m}}{N\Omega} \quad \text{with } \theta \in [\theta_n, \theta_{n+1}) \text{ and } \varphi \in [\varphi_m, \varphi_{m+1}). \quad (\text{A.3})$$

Figure A.2 shows the differential Pd sputtering yield $dY_{\text{Pd}}/d\Omega$ (a) and ion reflectivity $dY_{\text{R}}/d\Omega$ (b) for 2 keV Kr^+ ions at 60° incidence angle with respect to the target normal. Figure A.3 shows the simulated sputtered Pd $\Phi_{\text{Pd}}/\Phi_{\text{primary Kr}}$ and reflected ion $\Phi_{\text{reflected Kr}}/\Phi_{\text{primary Kr}}$ fluxes along a line parallel to the x-axis through the middle of the target. For this simulation, a target with $W = 6 \text{ mm}$, $H = 1.2 \text{ mm}$, and $H_0 = 0.2 \text{ mm}$ was used. H_0 was chosen to approximate the effect of the bending of the target. The fluxes are normalized to the primary ion flux $\Phi_{\text{primary Kr}}$ onto the substrate surface.

Bibliography

- [1] T. L. Alford, E. J. Jaquez, N. D. Theodore, S. W. Russell, M. Diale, D. Adams, and S. Anders: “Influence of interfacial copper on the room temperature oxidation of silicon”. *J. Appl. Phys.* **79.4** (1996), 2074–2078. DOI: 10.1063/1.361064.
- [2] P. F. A. Alkemade: “Propulsion of Ripples on Glass by Ion Bombardment”. *Phys. Rev. Lett.* **96** (2006), 107602. DOI: 10.1103/PhysRevLett.96.107602.
- [3] T. Basu, D. Datta, and T. Som: “Transition from ripples to faceted structures under low-energy argon ion bombardment of silicon: understanding the role of shadowing and sputtering”. *Nanoscale Res. Lett.* **8.1** (2013), 289. DOI: 10.1186/1556-276X-8-289.
- [4] P. Bedrossian and T. Klitsner: “Anisotropic vacancy kinetics and single-domain stabilization on Si(100)-2×1”. *Phys. Rev. Lett.* **68.5** (1992), 646–649. DOI: 10.1103/PhysRevLett.68.646.
- [5] J. P. Biersack and W. Eckstein: “Sputtering studies with the Monte Carlo Program TRIM.SP”. *Appl. Phys. A: Mater. Sci. Process.* **34.2** (1984), 73–94. DOI: 10.1007/BF00614759.
- [6] O. Bikondoa, D. Carbone, V. Chamard, and T. H. Metzger: “Ageing dynamics of ion bombardment induced self-organization processes”. *Sci. Rep.* **3** (May 2013), 1850. DOI: 10.1038/srep01850.
- [7] A. Boers: “Multiple ion scattering”. *Surf. Sci.* **63** (1977), 475–500. DOI: 10.1016/0039-6028(77)90360-0.
- [8] R. M. Bradley: “Exact Linear Dispersion Relation for the Sigmund Model of Ion Sputtering”. *Phys. Rev. B* **84** (2011), 075413. DOI: 10.1103/PhysRevB.84.075413.
- [9] R. M. Bradley: “Nanoscale patterns produced by ion erosion of a solid with codeposition of impurities: The crucial effect of compound formation”. *Phys. Rev. B* **87** (20 May 2013), 205408. DOI: 10.1103/PhysRevB.87.205408.
- [10] R. M. Bradley: “Producing ripple topographies by ion bombardment with codeposition of impurities: A curvature-dependent sputter yield is not required”. *Phys. Rev. B* **85** (2012), 115419. DOI: 10.1103/PhysRevB.85.115419.
- [11] R. M. Bradley: “Redeposition of sputtered material is a nonlinear effect”. *Phys. Rev. B* **83.7** (2011), 075404. DOI: 10.1103/PhysRevB.83.075404.

- [12] R. M. Bradley: “Surface instability of binary compounds caused by sputter yield amplification”. *J. Appl. Phys.* **111.11**, 114305 (2012), 114305. DOI: 10.1063/1.4724342.
- [13] R. M. Bradley: “Theory of nanodot and sputter cone arrays produced by ion sputtering with concurrent deposition of impurities”. *Phys. Rev. B* **83.19** (2011), 195410. DOI: 10.1103/PhysRevB.83.195410.
- [14] R. M. Bradley and J. M. E. Harper: “Theory of ripple topography induced by ion-bombardment”. *J. Vac. Sci. Technol. A* **6.4** (1988), 2390–2395. DOI: 10.1116/1.575561.
- [15] R. M. Bradley and P. D. Shipman: “A surface layer of altered composition can play a key role in nanoscale pattern formation induced by ion bombardment”. *Appl. Surf. Sci.* **258.9** (2012), 4161–4170. DOI: 10.1016/j.apsusc.2011.07.003.
- [16] J. W. Cahn: “On spinodal decomposition”. *Acta Metall.* **9.9** (1961), 795–801. DOI: 10.1016/0001-6160(61)90182-1.
- [17] J. W. Cahn and J. E. Hilliard: “Free Energy of a Nonuniform System. I. Interfacial Free Energy”. *J. Chem. Phys.* **28.2** (1958), 258–267. DOI: 10.1063/1.1744102.
- [18] G. Carter: “The effects of surface ripples on sputtering erosion rates and secondary ion emission yields”. *J. Appl. Phys.* **85.1** (1999), 455–459. DOI: 10.1063/1.369408.
- [19] G. Carter, J. S. Colligon, and M. J. Nobes: “The equilibrium topography of sputtered amorphous solids II”. *J. Mater. Sci.* **6.2** (1971), 115–117. DOI: 10.1007/BF00550340.
- [20] G. Carter and V. Vishnyakov: “Roughening and ripple instabilities on ion-bombarded Si”. *Phys. Rev. B* **54.24** (1996), 17647–17653. DOI: 10.1103/PhysRevB.54.17647.
- [21] M. Castro, R. Gago, L. Vázquez, J. Muñoz-García, and R. Cuerno: “Stress-induced solid flow drives surface nanopatterning of silicon by ion-beam irradiation”. *Phys. Rev. B* **86** (2012), 214107. DOI: 10.1103/PhysRevB.86.214107.
- [22] M. Castro and R. Cuerno: “Hydrodynamic approach to surface pattern formation by ion beams”. *Appl. Surf. Sci.* **258.9** (2012), 4171–4178. DOI: 10.1016/j.apsusc.2011.09.008.
- [23] M. Castro, R. Cuerno, L. Vázquez, and R. Gago: “Self-Organized Ordering of Nanostructures Produced by Ion-Beam Sputtering”. *Phys. Rev. Lett.* **94.1** (2005), 016102. DOI: 10.1103/PhysRevLett.94.016102.
- [24] W. L. Chan and E. Chason: “Making waves: Kinetic processes controlling surface evolution during low energy ion sputtering”. English. *J. Appl. Phys.* **101.12** (2007), 121301. DOI: 10.1063/1.2749198.

Bibliography

- [25] M. Chase Jr., C. A. Davies, J. Downey Jr., D. Frurip, R. McDonald, and A. N. Syverud, eds.: *NIST JANAF THERMOCHEMICAL TABLES*. U.S. Department of Commerce, 1985. URL: <http://kinetics.nist.gov/janaf/> (visited on Aug. 2, 2012).
- [26] E. Chason, T. M. Mayer, B. K. Kellerman, D. T. McIlroy, and A. J. Howard: “Roughening instability and evolution of the Ge(001) surface during ion sputtering”. *Phys. Rev. Lett.* **72.19** (1994), 3040–3043. DOI: 10.1103/PhysRevLett.72.3040.
- [27] C. J. Chen: *Introduction to Scanning Tunneling Microscopy*. Oxford Series in Optical and Imaging Sciences. New York and Oxford: Oxford University Press, 1993.
- [28] D. Cherns: “The surface structure of (111) gold films sputtered in the high voltage electron microscope A theoretical model”. *Philosophical Magazine* **36.6** (1977), 1429–1444. DOI: 10.1080/14786437708238526. eprint: <http://dx.doi.org/10.1080/14786437708238526>.
- [29] S. J. Chey, J. E. Van Nostrand, and D. G. Cahill: “Surface morphology of Ge(001) during etching by low-energy ions”. *Phys. Rev. B* **52** (23 1995), 16696–16701. DOI: 10.1103/PhysRevB.52.16696.
- [30] R. Collins, T. Marsh, and J. Jimenez-Rodriguez: “The diffusion approximation in atomic mixing”. *Nucl. Instrum. Meth. Phys. Res.* **209–210, Part 1** (1983), 147–156. DOI: 10.1016/0167-5087(83)90793-7.
- [31] M. Cornejo, B. Ziberi, C. Meinecke, and F. Frost: “Formation of two ripple modes on Si by ion erosion with simultaneous Fe incorporation”. *Appl. Surf. Sci.* **257.20** (2011), 8659–8664. DOI: 10.1016/j.apsusc.2011.05.044.
- [32] M. Cornejo, B. Ziberi, C. Meinecke, D. Hirsch, J. Gerlach, T. H”oche, F. Frost, and B. Rauschenbach: “Self-organized patterning on Si(001) by ion sputtering with simultaneous metal incorporation”. *Appl. Phys. A: Mater. Sci. Process.* **102** (2011), 593–599. DOI: 10.1007/s00339-011-6246-y.
- [33] G. Costantini, S. Rusponi, F. B. de Mongeot, C. Boragno, and U. Valbusa: “Periodic structures induced by normal-incidence sputtering on Ag(110) and Ag(001): flux and temperature dependence”. *J. Phys.: Condens. Matter* **13.26** (2001), 5875. URL: <http://stacks.iop.org/0953-8984/13/i=26/a=303>.
- [34] R. Cuerno and A.-L. Barabási: “Dynamic Scaling of Ion-Sputtered Surfaces”. *Phys. Rev. Lett.* **74.23** (1995), 4746–4749. DOI: 10.1103/PhysRevLett.74.4746.
- [35] P.-E. Danielsson: “Generalized and Seperable Sobel Operators”. In: *Machine vision for three-dimensional scenes*. Ed. by H. Freeman. Academic Press, 1990, pp. 347–380.

- [36] D. Datta, S. Mondal, and S. Bhattacharyya: “Growth process of GaAs ripples as a function of incident Ar-ion dose”. *Appl. Surf. Sci.* **258.9** (2012). International Conference on Ion-beam Induced Nanopatterning of Materials (IINM-2011), 4152–4155. DOI: 10.1016/j.apsusc.2011.10.017.
- [37] D. P. Datta and T. K. Chini: “Coarsening of ion-beam-induced surface ripple in Si: Nonlinear effect vs. geometrical shadowing”. *Phys. Rev. B* **76.7** (2007), 075323. DOI: 10.1103/PhysRevB.76.075323.
- [38] C. Diddens and S. J. Linz: “Redeposition during ion-beam erosion can stabilize well-ordered nanostructures”. *EPL (Europhysics Letters)* **104.1** (2013), 17010. URL: <http://stacks.iop.org/0295-5075/104/i=1/a=17010>.
- [39] L. R. Doolittle: “Algorithms for the rapid simulation of Rutherford backscattering spectra”. *Nucl. Instrum. Methods Phys. Res., Sect. B* **9.3** (1985), 344–351. DOI: 10.1016/0168-583X(85)90762-1.
- [40] P. Eaton and P. West: *Atomic Force Microscopy*. Oxford: Oxford University Press, 2010. DOI: 10.1093/acprof:oso/9780199570454.001.0001.
- [41] W. Eckstein: “Backscattering and sputtering with the monte-carlo program TRIM.SP”. *Radiat. Eff. Defects Solids* **130.1** (1994), 239–250. DOI: 10.1080/10420159408219787.
- [42] W. Eckstein and J. P. Biersack: “Computer simulation of two-component target sputtering”. *Appl. Phys. A: Mater. Sci. Process.* **37.2** (1985), 95–108. DOI: 10.1007/BF00618859.
- [43] G. Ehrlich and F. G. Hudda: “Atomic View of Surface Self-Diffusion: Tungsten on Tungsten”. *J. Chem. Phys.* **44.3** (1966), 1039–1049. DOI: 10.1063/1.1726787.
- [44] M. Engler, F. Frost, S. Müller, S. Macko, M. Will, R. Feder, D. Spemann, R. Hübner, S. Facsko, and T. Michely: “Silicide induced ion beam patterning of Si(001)”. *Nanotechnology* **25.11** (2014), 115303. DOI: 10.1088/0957-4484/25/11/115303.
- [45] M. Engler, S. Macko, F. Frost, and T. Michely: “Evolution of ion beam Induced patterns on Si(001)”. *Phys. Rev. B* **89** (2014), 245412. DOI: 10.1103/PhysRevB.89.245412.
- [46] S. Facsko, T. Dekorsy, C. Koerdt, C. Trappe, H. Kurz, A. Vogt, and H. L. Hartnagel: “Formation of Ordered Nanoscale Semiconductor Dots by Ion Sputtering”. *Science* **285.5433** (1999), 1551–1553. DOI: 10.1126/science.285.5433.1551.
- [47] D. Flamm, F. Frost, and D. Hirsch: “Evolution of surface topography of fused silica by ion beam sputtering”. *Appl. Surf. Sci.* **179.1-4** (2001). 11th Conference on Applied Surface Science, 95–101. DOI: 10.1016/S0169-4332(01)00269-0.

Bibliography

- [48] D. F. Förster: “EuO and Eu on metal crystals and graphene: interface effects and epitaxial films”. PhD thesis. Cologne: Universität zu Köln, 2011. URN: urn:nbn:de:hbz:38-45235.
- [49] H. Fouckhardt, I. Steingoetter, M. Brinkmann, M. Hagemann, H. Zarschizky, and L. Zschiedrich: “nm- and μm -Scale Surface Roughness on Glass with Specific Optical Scattering Characteristics on Demand”. *Advances in OptoElectronics* **2007** (2007), 27316. DOI: 10.1155/2007/27316.
- [50] J. Frenkel: “On the Electrical Resistance of Contacts between Solid Conductors”. *Phys. Rev.* **36** (1930), 1604–1618. DOI: 10.1103/PhysRev.36.1604.
- [51] F. Frost, A. Schindler, and F. Bigl: “Roughness Evolution of Ion Sputtered Rotating InP Surfaces: Pattern Formation and Scaling Laws”. *Phys. Rev. Lett.* **85** (2000), 4116–4119. DOI: 10.1103/PhysRevLett.85.4116.
- [52] R. Gago, L. Vázquez, R. Cuerno, M. Varela, C. Ballesteros, and J. M. Albella: “Nanopatterning of silicon surfaces by low-energy ion-beam sputtering: dependence on the angle of ion incidence”. *Nanotechnology* **13.3** (2002), 304. DOI: 10.1088/0957-4484/13/3/313.
- [53] R. Gago, L. Vázquez, O. Plantevin, J. A. Sánchez-García, M. Varela, M. C. Ballesteros, J. M. Albella, and T. H. Metzger: “Temperature influence on the production of nanodot patterns by ion beam sputtering of Si(001)”. *Phys. Rev. B* **73.15** (2006), 155414. DOI: 10.1103/PhysRevB.73.155414.
- [54] H. Gnaser: *Low-Energy Ion Radiation of Solid Surfaces*. Springer Tracts in Modern Physics **146**. Berlin and Heidelberg: Springer, 1999. DOI: 10.1007/BFb0110693.
- [55] S. Habenicht, K. P. Lieb, J. Koch, and A. D. Wieck: “Ripple propagation and velocity dispersion on ion-beam-eroded silicon surfaces”. *Phys. Rev. B* **65** (2002), 115327. DOI: 10.1103/PhysRevB.65.115327.
- [56] R. J. Hamers, R. M. Tromp, and J. E. Demuth: “Scanning tunneling microscopy of Si(001)”. *Phys. Rev. B* **34** (1986), 5343–5357. DOI: 10.1103/PhysRevB.34.5343.
- [57] M. Hanbücken, B. Röttger, and H. Neddermeyer: “Scanning tunneling microscopy on concave-shaped Si(100) substrates”. *Surf. Sci.* **331–333, Part B** (1995). Proceedings of the 14th European Conference on Surface Science, 1028–1032. DOI: 10.1016/0039-6028(95)00130-1.
- [58] H. Hansen, A. Redinger, S. Messlinger, G. Stoian, Y. Rosandi, H. M. Urbassek, U. Linke, and T. Michely: “Mechanisms of pattern formation in grazing-incidence ion bombardment of Pt(111)”. *Phys. Rev. B* **73** (2006), 235414. DOI: 10.1103/PhysRevB.73.235414.
- [59] W. Hauffe: “Development of the surface topography on polycrystalline metals by ion bombardment investigated by scanning electron microscopy”. *phys. stat. sol. (a)* **4.1** (1971), 111–120. DOI: 10.1002/pssa.2210040112.

- [60] W. Hauße: “Faceting mechanism in the sputtering process”. *phys. stat. sol. (a)* **35.2** (1976), K93–K96. DOI: 10.1002/pssa.2210350246.
- [61] C. Herring: “Effect of Change of Scale on Sintering Phenomena”. *J. Appl. Phys.* **21.4** (1950), 301–303. DOI: 10.1063/1.1699658.
- [62] H. Hofsäss, K. Zhang, A. Pape, O. Bobes, and M. Brötzmann: “The role of phase separation for self-organized surface pattern formation by ion beam erosion and metal atom co-deposition”. *Appl. Phys. A: Mater. Sci. Process.* **111** (2012), 653–664. DOI: 10.1007/s00339-012-7285-8.
- [63] H. Hofsäss and K. Zhang: “Fundamentals of surfactant sputtering”. *Nucl. Instrum. Methods Phys. Res., Sect. B* **267.16** (2009). Proceedings of the 23rd International Conference on Atomic Collisions in Solids, 2731–2734. DOI: 10.1016/j.nimb.2009.05.028.
- [64] H. Hofsäss and K. Zhang: “Surfactant sputtering”. *Appl. Phys. A: Mater. Sci. Process.* **92** (2008), 517–524. DOI: 10.1007/s00339-008-4678-9.
- [65] I. Horcas, R. Fernandez, J. M. Gomez-Rodriguez, J. Colchero, J. Gomez-Herrero, and A. M. Baro: “WSXM: A software for scanning probe microscopy and a tool for nanotechnology”. *Rev. Sci. Instrum.* **78.1** (2007), 013705. DOI: 10.1063/1.2432410.
- [66] K. Ishida, T. Nishizawa, and M. Schlesinger: “The Co-Si (Cobalt-Silicon) system”. English. *J. Phase Equil.* **12.5** (1991), 578–586. DOI: 10.1007/BF02645074.
- [67] M. Kalff, G. Comsa, and T. Michely: “Temperature dependent morphological evolution of Pt(111) by ion erosion: destabilization, phase coexistence and coarsening”. *Surf. Sci.* **486.1–2** (2001), 103–135. DOI: 10.1016/S0039-6028(01)01015-9.
- [68] A. Keller, R. Cuerno, S. Facsko, and W. Möller: “Anisotropic scaling of ripple morphologies on high-fluence sputtered silicon”. *Phys. Rev. B* **79.11** (2009), 115437. DOI: 10.1103/PhysRevB.79.115437.
- [69] A. Keller, S. Facsko, and W. Möller: “The morphology of amorphous SiO₂ surfaces during low energy ion sputtering”. *J. Phys.: Condens. Matter* **21.49** (2009), 495305. URL: <http://stacks.iop.org/0953-8984/21/i=49/a=495305>.
- [70] A. Keller, M. Nicoli, S. Facsko, and R. Cuerno: “Dynamic effects induced by renormalization in anisotropic pattern forming systems”. *Phys. Rev. E* **84** (2011), 015202. DOI: 10.1103/PhysRevE.84.015202.
- [71] A. Keller, S. Roßbach, S. Facsko, and W. Möller: “Simultaneous formation of two ripple modes on ion sputtered silicon”. *Nanotechnology* **19.13** (2008), 135303. URL: <http://stacks.iop.org/0957-4484/19/i=13/a=135303>.

Bibliography

- [72] J. Kim, D. G. Cahill, and R. S. Averback: “Surface morphology of Ge(111) during etching by keV ions”. *Phys. Rev. B* **67** (Jan. 2003), 045404. DOI: 10.1103/PhysRevB.67.045404.
- [73] J. Kim, J.-Y. Ji, J. Kline, J. Tucker, and T.-C. Shen: “The role of antiphase boundaries during ion sputtering and solid phase epitaxy of Si(001)”. *Surf. Sci.* **538.3** (2003), L471–L476. DOI: 10.1016/S0039-6028(03)00730-1.
- [74] K. Kong, H. W. Yeom, D. Ahn, H. Yi, and B. D. Yu: “Ab initio study of adsorption and diffusion of Ag atoms on a Si(001) surface”. *Phys. Rev. B* **67** (June 2003), 235328. DOI: 10.1103/PhysRevB.67.235328.
- [75] J. Krug, M. Plischke, and M. Siegert: “Surface diffusion currents and the universality classes of growth”. *Phys. Rev. Lett.* **70** (1993), 3271–3274. DOI: 10.1103/PhysRevLett.70.3271.
- [76] L. D. Landau and E. M. Lifschitz: *Lehrbuch der theoretischen Physik*. Vol. 1: *Mechanik*. 14th ed. Harri Deutsch, 1997.
- [77] G. Lewis, M. Nobes, G. Carter, and J. Whitton: “The mechanisms of etch pit and ripple structure formation on ion bombarded Si and other amorphous solids”. *Nucl. Instrum. Meth.* **170.1-3** (1980), 363–369. DOI: 10.1016/0029-554X(80)91041-1.
- [78] M. O. Liedke, B. Liedke, A. Keller, B. Hillebrands, A. Mücklich, S. Facsko, and J. Fassbender: “Induced anisotropies in exchange-coupled systems on rippled substrates”. *Phys. Rev. B* **75.22** (2007), 220407. DOI: 10.1103/PhysRevB.75.220407.
- [79] S. Macko: “Mechanisms and Manipulation of Ion Beam Pattern Formation on Si(001)”. PhD thesis. Universität zu Köln, 2011. URN: urn:nbn:de:hbz:38-44805.
- [80] S. Macko, F. Frost, M. Engler, D. Hirsch, T. Höche, J. Grenzer, and T. Michely: “Phenomenology of iron-assisted ion beam pattern formation on Si(001)”. *New. J. Phys.* **13.7** (2011), 073017. DOI: 10.1088/1367-2630/13/7/073017.
- [81] S. Macko, F. Frost, B. Ziberi, D. F. Förster, and T. Michely: “Is keV ion induced pattern formation on Si(001) caused by metal impurities?” *Nanotechnology* **21.8** (2010), 085301. DOI: 10.1088/0957-4484/21/8/085301.
- [82] S. Macko, J. Grenzer, F. Frost, M. Engler, D. Hirsch, M. Fritzsche, A. Mücklich, and T. Michely: “Iron-assisted ion beam patterning of Si(001) in the crystalline regime”. *New. J. Phys.* **14.7** (2012), 073003. DOI: 10.1088/1367-2630/14/7/073003.
- [83] C. S. Madi, E. Anzenberg, K. F. Ludwig, and M. J. Aziz: “Mass Redistribution Causes the Structural Richness of Ion-Irradiated Surfaces”. *Phys. Rev. Lett.* **106.6** (2011), 066101. DOI: 10.1103/PhysRevLett.106.066101.

- [84] C. S. Madi and M. J. Aziz: “Multiple scattering causes the low energy–low angle constant wavelength topographical instability of argon ion bombarded silicon surfaces”. *Appl. Surf. Sci.* **258.9** (2012), 4112–4115. DOI: 10.1016/j.apsusc.2011.07.143.
- [85] C. S. Madi, B. Davidovitch, H. B. George, S. A. Norris, M. P. Brenner, and M. J. Aziz: “Multiple Bifurcation Types and the Linear Dynamics of Ion Sputtered Surfaces”. *Phys. Rev. Lett.* **101.24** (2008), 246102. DOI: 10.1103/PhysRevLett.101.246102.
- [86] C. S. Madi, H. B. George, and M. J. Aziz: “Linear stability and instability patterns in ion-sputtered silicon”. *J. Phys.: Condens. Matter* **21.22** (2009), 224010. DOI: 10.1088/0953-8984/21/22/224010.
- [87] M. A. Makeev and A.-L. Barabasi: “Ion-induced effective surface diffusion in ion sputtering”. *Appl. Phys. Lett.* **71.19** (1997), 2800–2802. DOI: 10.1063/1.120140.
- [88] M. A. Makeev, R. Cuerno, and A.-L. Barabási: “Morphology of ion-sputtered surfaces”. *Nucl. Instrum. Methods Phys. Res., Sect. B* **197.3–4** (2002), 185–227. DOI: 10.1016/S0168-583X(02)01436-2.
- [89] N. Masoud, D.-E. Arafah, and K. Becker: “Ion mixing in Ag-films on Si-substrates induced by a high fluence $^{40}\text{Ar}^+$ beam with a flux of $0.2 \mu\text{A}/\text{cm}^2$ ”. *Nucl. Instrum. Methods Phys. Res., Sect. B* **198.1-2** (2002), 64–72. DOI: 10.1016/S0168-583X(02)01515-X.
- [90] N. Matsunami and H. Hosono: “Colloid formation effects on depth profile of implanted Ag in SiO_2 glass”. *Appl. Phys. Lett.* **63.15** (1993), 2050–2052. DOI: 10.1063/1.110588.
- [91] M. Mayer: “Rutherford Backscattering Spectrometry (RBS)”. In: *Nuclear Physics and Data for Material Analysis*. Ed. by N. Paver. Vol. 22. ICTP Lecture Notes Series. Trieste, 2008, pp. 55–80. URL: <http://publications.ictp.it/lms/vol22.html>.
- [92] T. Michely and G. Comsa: “Temperature dependence of the sputtering morphology of Pt(111)”. *Surf. Sci.* **256.3** (1991), 217–226. DOI: 10.1016/0039-6028(91)90865-P.
- [93] T. Michely, M. Kaiser, and M. J. Rost: “Plug “n” play scanning probe microscopy”. *Rev. Sci. Instrum.* **71.12** (2000), 4461–4467. DOI: 10.1063/1.1322587.
- [94] T. Michely, M. Kalff, G. Comsa, M. Strobel, and K.-H. Heinig: “Step Edge Diffusion and Step Atom Detachment in Surface Evolution: Ion Erosion of Pt(111)”. *Phys. Rev. Lett.* **86** (2001), 2589–2592. DOI: 10.1103/PhysRevLett.86.2589.
- [95] Y. W. Mo, J. Kleiner, M. B. Webb, and M. G. Lagally: “Activation energy for surface diffusion of Si on Si(001): A scanning-tunneling-microscopy study”. *Phys. Rev. Lett.* **66.15** (1991), 1998–2001. DOI: 10.1103/PhysRevLett.66.1998.

Bibliography

- [96] E. G. Moroni, W. Wolf, J. Hafner, and R. Podloucky: “Cohesive, structural, and electronic properties of Fe-Si compounds”. *Phys. Rev. B* **59.20** (1999), 12860–12871. DOI: 10.1103/PhysRevB.59.12860.
- [97] W. W. Mullins: “Theory of Thermal Grooving”. *J. Appl. Phys.* **28.3** (1957), 333–339. DOI: 10.1063/1.1722742.
- [98] W. W. Mullins: “Flattening of a Nearly Plane Solid Surface due to Capillarity”. *J. Appl. Phys.* **30.1** (1959), 77–83. DOI: 10.1063/1.1734979.
- [99] M. Nastasi, J. W. Mayer, and J. K. Hirvonen: *Ion-Solid Interactions: Fundamentals and Applications*. Ed. by D. R. Clarke, S. Suresh, and I. M. Ward. Cambridge Solid State Science Series. Cambridge: Cambridge University Press, 1996.
- [100] M. Navez, C. Sella, and D. Chaperot: “Étude de l’attaque du verre par bombardement ionique”. French. *Comptes Rendus Hebdomadaires des Seances de l’Academie des Sciences* **254.2** (1962), 240.
- [101] D. Nečas and P. Klapetek: “Gwyddion: an open-source software for SPM data analysis”. *Cent. Eur. J. Phys.* **10** (2012), 181–188. DOI: 10.2478/s11534-011-0096-2.
D. Nečas and P. Klapetek: *Gwyddion*. URL: <http://gwyddion.net/>.
- [102] M. J. Nobes, J. S. Colligon, and G. Carter: “The Equilibrium Topography of Sputtered Amorphous Solids”. *J. Mater. Sci.* **4.8** (1969), 730–733. DOI: 10.1007/BF00742430.
- [103] K. Nordlund, M. Ghaly, R. S. Averback, M. Caturla, T. Diaz de la Rubia, and J. Tarus: “Defect production in collision cascades in elemental semiconductors and fcc metals”. *Phys. Rev. B* **57** (13 1998), 7556–7570. DOI: 10.1103/PhysRevB.57.7556.
- [104] S. A. Norris: “Ion-assisted phase separation in compound films: An alternate route to ordered nanostructures”. *J. Appl. Phys.* **114.20**, 204303 (2013), 204303. DOI: 10.1063/1.4833551. arXiv: 1205.6834v2.
- [105] S. A. Norris, M. P. Brenner, and M. J. Aziz: “From crater functions to partial differential equations: a new approach to ion bombardment induced nonequilibrium pattern formation”. *J. Phys.: Condens. Matter* **21.22** (2009), 224017. DOI: 10.1088/0953-8984/21/22/224017.
- [106] S. A. Norris, J. Samela, L. Bukonte, M. Backman, F. Djurabekova, K. Nordlund, C. S. Madi, M. P. Brenner, and M. J. Aziz: “Molecular dynamics of single-particle impacts predicts phase diagrams for large scale pattern formation”. *Nat. Comm.* **2** (2011), 276. DOI: 10.1038/ncomms1280.
- [107] X. Ou, A. Keller, M. Helm, J. Fassbender, and S. Facsko: “Reverse Epitaxy of Ge: Ordered and Faceted Surface Patterns”. *Phys. Rev. Lett.* **111** (2013), 016101. DOI: 10.1103/PhysRevLett.111.016101.

- [108] G. Ozaydin, A. S. Ozcan, Y. Wang, K. F. Ludwig, H. Zhou, R. L. Headrick, and D. P. Siddons: “Real-time x-ray studies of Mo-seeded Si nanodot formation during ion bombardment”. *Appl. Phys. Lett.* **87.16**, 163104 (2005), 163104. DOI: 10.1063/1.2099521.
- [109] G. Ozaydin-Ince and K. F. Ludwig Jr: “In situ x-ray studies of native and Mo-seeded surface nanostructuring during ion bombardment of Si(100)”. *J. Phys.: Condens. Matter* **21.22** (2009), 224008. DOI: 10.1088/0953-8984/21/22/224008.
- [110] S. Park, B. Kahng, H. Jeong, and A.-L. Barabási: “Dynamics of Ripple Formation in Sputter Erosion: Nonlinear Phenomena”. *Phys. Rev. Lett.* **83** (1999), 3486–3489. DOI: 10.1103/PhysRevLett.83.3486.
- [111] B. Poelsema, R. Kunkel, L. K. Verheij, and G. Comsa: “Mechanisms for annealing of ion-bombardment-induced defects on Pt(111)”. *Phys. Rev. B* **41** (16 June 1990), 11609–11611. DOI: 10.1103/PhysRevB.41.11609.
- [112] B. Poelsema, L. K. Verheij, and G. Comsa: “”Two-Layer” Behavior of the Pt(111) Surface during Low-Energy Ar⁺-Ion Sputtering at High Temperatures”. *Phys. Rev. Lett.* **53** (26 Dec. 1984), 2500–2503. DOI: 10.1103/PhysRevLett.53.2500.
- [113] C. Polop, C. Rosiepen, S. Bleikamp, R. Drese, J. Mayer, A. Dimyati, and T. Michely: “The STM view of the initial stages of polycrystalline Ag film formation”. *New. J. Phys.* **9.3** (2007), 74. URL: <http://stacks.iop.org/1367-2630/9/i=3/a=074>.
- [114] B. Predel: “Ag-Si (Silver-Silicon)”. In: *Landolt-Börnstein - Group IV Physical Chemistry*. Ed. by O. Madelung. Vol. 5a. SpringerMaterials - The Landolt-Börnstein Database (<http://www.springermaterials.com>), 1991. DOI: 10.1007/10000866_68.
- B. Predel: “C-Si (Carbon-Silicon)”. In: *Landolt-Börnstein - Group IV Physical Chemistry Numerical Data and Functional Relationships in Science and Technology*. Ed. by O. Madelung. Vol. 5b: B-Ba – C-Zr. SpringerMaterials, 1992. DOI: 10.1007/10040476_664.
- B. Predel: “Cu-Si (Copper-Silicon)”. In: *Landolt-Börnstein - Group IV Physical Chemistry Numerical Data and Functional Relationships in Science and Technology*. Ed. by O. Madelung. Vol. 5d: Cr-Cs – Cu-Zr. SpringerMaterials, 1994. DOI: 10.1007/10086090_1117.
- B. Predel: “Fe-Si (Iron-Silicon)”. In: *Landolt-Börnstein - Group IV Physical Chemistry Numerical Data and Functional Relationships in Science and Technology*. Ed. by O. Madelung. Vol. 5e: Dy-Er – Fr-Mo. SpringerMaterials, 1995. DOI: 10.1007/10474837_1340.
- B. Predel: “Ir-Si (Iridium-Silicon)”. In: *Landolt-Börnstein - Group IV Physical Chemistry Numerical Data and Functional Relationships in Science and Technology*. Ed. by O. Madelung. Vol. 5G: Hg-Ho – La-Zr. SpringerMaterials, 1997. DOI:

- 10.1007/10506626_1811.
- B. Predel: “Mo-Si (Molybdenum-Silicon)”. In: *Landolt-Börnstein - Group IV Physical Chemistry Numerical Data and Functional Relationships in Science and Technology*. Ed. by O. Madelung. Vol. 5H: Li-Mg – Nd-Zr. SpringerMaterials, 1997. DOI: 10.1007/10522884_2097.
- B. Predel: “Ni-Si (Nickel-Silicon)”. In: *Landolt-Börnstein - Group IV Physical Chemistry Numerical Data and Functional Relationships in Science and Technology*. Ed. by O. Madelung. Vol. 5I: Ni-Np – Pt-Zr. SpringerMaterials, 1998. DOI: 10.1007/10542753_2263.
- B. Predel: “Pb-Si (Lead-Silicon)”. In: *Landolt-Börnstein - Group IV Physical Chemistry Numerical Data and Functional Relationships in Science and Technology*. Ed. by O. Madelung. Vol. 5I: Ni-Np – Pt-Zr. SpringerMaterials, 1998. DOI: 10.1007/10542753_2417.
- B. Predel: “Pd-Si (Palladium-Silicon)”. In: *Landolt-Börnstein - Group IV Physical Chemistry Numerical Data and Functional Relationships in Science and Technology*. Ed. by O. Madelung. Vol. 5I: Ni-Np – Pt-Zr. SpringerMaterials, 1998. DOI: 10.1007/10542753_2445.
- B. Predel: “Si-W (Silicon-Tungsten)”. In: *Landolt-Börnstein - Group IV Physical Chemistry Numerical Data and Functional Relationships in Science and Technology*. Ed. by O. Madelung. Vol. 5 J: Pu-Re – Zn-Zr. SpringerMaterials, 1998. DOI: 10.1007/10551312_2742.
- [115] J. Punzel and W. Hauffe: “Development of relief structures on Si surfaces by ion bombardment”. *Phys. Status Solidi A* **14.2** (1972), K97–K99. DOI: 10.1002/pssa.2210140241.
- [116] A. Redinger, Y. Rosandi, H. M. Urbassek, and T. Michely: “Step-edge sputtering through grazing incidence ions investigated by scanning tunneling microscopy and molecular dynamics simulations”. *Phys. Rev. B* **77** (2008), 195436. DOI: 10.1103/PhysRevB.77.195436.
- [117] C. Roland and G. H. Gilmer: “Epitaxy on surfaces vicinal to Si(001). II. Growth properties of Si(001) steps”. *Phys. Rev. B* **46** (1992), 13437–13451. DOI: 10.1103/PhysRevB.46.13437.
- [118] M. Rost and J. Krug: “Anisotropic Kuramoto-Sivashinsky Equation for Surface Growth and Erosion”. *Phys. Rev. Lett.* **75.21** (1995), 3894–3897. DOI: 10.1103/PhysRevLett.75.3894.
- [119] S. Rusponi, G. Costantini, C. Boragno, and U. Valbusa: “Ripple Wave Vector Rotation in Anisotropic Crystal Sputtering”. *Phys. Rev. Lett.* **81** (1998), 2735–2738. DOI: 10.1103/PhysRevLett.81.2735.

- [120] S. Rusponi, G. Costantini, C. Boragno, and U. Valbusa: “Scaling Laws of the Ripple Morphology on Cu(110)”. *Phys. Rev. Lett.* **81.19** (1998), 4184–4187. DOI: 10.1103/PhysRevLett.81.4184.
- [121] J. A. Sánchez-García, L. Vázquez, R. Gago, A. Redondo-Cubero, J. M. Albella, and Z. Czigány: “Tuning the surface morphology in self-organized ion beam nanopatterning of Si(001) via metal incorporation: from holes to dots”. *Nanotechnology* **19.35** (2008), 355306. DOI: 10.1088/0957-4484/19/35/355306.
- [122] R. L. Schwoebel and E. J. Shipsey: “Step Motion on Crystal Surfaces”. *J. Appl. Phys.* **37.10** (1966), 3682–3686. DOI: 10.1063/1.1707904.
- [123] V. B. Shenoy, W. L. Chan, and E. Chason: “Compositionally Modulated Ripples Induced by Sputtering of Alloy Surfaces”. *Phys. Rev. Lett.* **98.25** (2007), 256101. DOI: 10.1103/PhysRevLett.98.256101.
- [124] P. D. Shipman and R. M. Bradley: “Theory of nanoscale pattern formation induced by normal-incidence ion bombardment of binary compounds”. *Phys. Rev. B* **84** (2011), 085420. DOI: 10.1103/PhysRevB.84.085420.
- [125] M. Siegert and M. Plischke: “Slope Selection and Coarsening in Molecular Beam Epitaxy”. *Phys. Rev. Lett.* **73** (1994), 1517–1520. DOI: 10.1103/PhysRevLett.73.1517.
- [126] P. Sigmund: “A mechanism of surface micro-roughening by ion bombardment”. *J. Mater. Sci.* **8.11** (1973), 1545–1553. DOI: 10.1007/BF00754888.
- [127] R. M. Smart and F. P. Glasser: “Compound Formation and Phase Equilibria in the System PbO-SiO₂”. *J. Am. Ceram. Soc.* **57.9** (1974), 378–382. DOI: 10.1111/j.1151-2916.1974.tb11416.x.
- [128] P. Stadelmann: “EMS – a software package for electron diffraction analysis and HREM image simulation in materials science”. *Ultramicroscopy* **21.2** (1987), 131–145. DOI: 10.1016/0304-3991(87)90080-5.
- [129] A. Stewart and M. Thompson: “Microtopography of surfaces eroded by ion-bombardment”. English. *J. Mater. Sci.* **4.1** (1969), 56–60. DOI: 10.1007/BF00555048.
- [130] C. Teichert, C. Hofer, and G. Hlawacek: “Self-organization of Nanostructures in Inorganic and Organic Semiconductor Systems”. *Adv. Eng. Mater.* **8.11** (2006), 1057–1065. DOI: 10.1002/adem.200600142.
- [131] M. Teichmann, J. Lorbeer, B. Ziberi, F. Frost, and B. Rauschenbach: “Pattern formation on Ge by low energy ion beam erosion”. *New. J. Phys.* **15.10** (2013), 103029. DOI: 10.1088/1367-2630/15/10/103029.

Bibliography

- [132] J. Tersoff and D. R. Hamann: “Theory and Application for the Scanning Tunneling Microscope”. *Phys. Rev. Lett.* **50** (25 June 1983), 1998–2001. DOI: 10.1103/PhysRevLett.50.1998.
- [133] T. Tiedje and A. Ballestad: “Atomistic basis for continuum growth equation: Description of morphological evolution of GaAs during molecular beam epitaxy”. *Thin Solid Films* **516.12** (2008), 3705–3728. DOI: 10.1016/j.tsf.2007.11.015.
- [134] R. M. Tromp, R. J. Hamers, and J. E. Demuth: “Si(001) Dimer Structure Observed with Scanning Tunneling Microscopy”. *Phys. Rev. Lett.* **55.12** (1985), 1303–1306. DOI: 10.1103/PhysRevLett.55.1303.
- [135] C. C. Umbach, R. L. Headrick, and K.-C. Chang: “Spontaneous Nanoscale Corrugation of Ion-Eroded SiO₂: The Role of Ion-Irradiation-Enhanced Viscous Flow”. *Phys. Rev. Lett.* **87.24** (2001), 246104. DOI: 10.1103/PhysRevLett.87.246104.
- [136] J. Villain: “Continuum models of crystal growth from atomic beams with and without desorption”. *J. Phys. I France* **1.1** (1991), 19–42. DOI: 10.1051/jp1:1991114.
- [137] J. Völlner, B. Ziberi, F. Frost, and B. Rauschenbach: “Topography evolution mechanism on fused silica during low-energy ion beam sputtering”. *J. Appl. Phys.* **109.4** (2011), 043501. DOI: 10.1063/1.3549170.
- [138] H. Watanabe and M. Ichikawa: “Anisotropic kinetics of vacancy diffusion and annihilation on Si(001) surfaces studied by scanning reflection electron microscopy”. *Phys. Rev. B* **55** (1997), 9699–9705. DOI: 10.1103/PhysRevB.55.9699.
- [139] M. Webb: “Strain effects on Si(001)”. *Surf. Sci.* **299–300** (1994), 454–468. DOI: 10.1016/0039-6028(94)90675-0.
- [140] W. D. Wilson, L. G. Haggmark, and J. P. Biersack: “Calculations of nuclear stopping, ranges, and straggling in the low-energy region”. *Phys. Rev. B* **15.5** (1977), 2458–2468. DOI: 10.1103/PhysRevB.15.2458.
- [141] M. Winter: *WebElements: the periodic table on the web*. URL: <http://www.webelements.com/> (visited on Mar. 6, 2014).
- [142] H. J. W. Zandvliet: “Energetics of Si(001)”. *Rev. Mod. Phys.* **72** (2 Apr. 2000), 593–602. DOI: 10.1103/RevModPhys.72.593.
- [143] K. Zhang, M. Brotzmann, and H. Hofsass: “Sharp transition from ripple patterns to a flat surface for ion beam erosion of Si with simultaneous co-deposition of iron”. *AIP Advances* **2.3**, 032123 (2012), 032123. DOI: 10.1063/1.4739843.

- [144] K. Zhang, H. Hofsäss, F. Rotter, M. Uhrmacher, C. Ronning, and J. Krauser: “Morphology of Si surfaces sputter-eroded by low-energy Xe-ions at glancing incident angle”. *Surf. Coat. Technol.* **203.17-18** (2009). SMMIB-15, 15th International Conference on Surface Modification of Materials by Ion Beams, 2395–2398. DOI: 10.1016/j.surfcoat.2009.02.105.
- [145] K. Zhang, F. Rotter, M. Uhrmacher, C. Ronning, J. Krauser, and H. Hofsäss: “Ion induced nanoscale surface ripples on ferromagnetic films with correlated magnetic texture”. *New. J. Phys.* **9.2** (2007), 29. URL: <http://stacks.iop.org/1367-2630/9/i=2/a=029>.
- [146] K. Zhang, M. Uhrmacher, H. Hofsäss, and J. Krauser: “Magnetic texturing of ferromagnetic thin films by sputtering induced ripple formation”. *J. Appl. Phys.* **103.8**, 083507 (2008), 083507. DOI: 10.1063/1.2905324.
- [147] K. Zhang, M. Brötzmann, and H. Hofsäss: “Surfactant-driven self-organized surface patterns by ion beam erosion”. *New. J. Phys.* **13.1** (2011), 013033. DOI: 10.1088/1367-2630/13/1/013033.
- [148] Y. Zhang, J. R. G. Evans, and S. Yang: “Corrected Values for Boiling Points and Enthalpies of Vaporization of Elements in Handbooks”. *J. Chem. Eng. Data* **56.2** (2011), 328–337. DOI: 10.1021/je1011086.
- [149] J. Zhou, S. Facsko, M. Lu, and W. Möller: “Nanopatterning of Si surfaces by normal incident ion erosion: Influence of iron incorporation on surface morphology evolution”. *J. Appl. Phys.* **109** (2011), 104315. DOI: 10.1063/1.3585796.
- [150] J. Zhou and M. Lu: “Mechanism of Fe impurity motivated ion-nanopatterning of Si (100) surfaces”. *Phys. Rev. B* **82.12** (2010), 125404. DOI: 10.1103/PhysRevB.82.125404.
- [151] B. Ziberi, M. Cornejo, F. Frost, and B. Rauschenbach: “Highly ordered nanopatterns on Ge and Si surfaces by ion beam sputtering”. *J. Phys.: Condens. Matter* **21.22** (2009), 224003. DOI: 10.1088/0953-8984/21/22/224003.
- [152] B. Ziberi, F. Frost, T. Höche, and B. Rauschenbach: “Ripple pattern formation on silicon surfaces by low-energy ion-beam erosion: Experiment and theory”. *Phys. Rev. B* **72.23** (2005), 235310. DOI: 10.1103/PhysRevB.72.235310.

Acknowledgements

I would like to thank all the people who contributed to this thesis. Many people helped me to finish this thesis in many different ways.

First I would like to thank Thomas Michely for supervising my dissertation project. He always found some time to discuss problems and new ideas.

I would like to thank Stephan Schlemmer as referee of this thesis.

For performing AFM measurements of my samples and giving me the opportunity to do AFM measurements myself at the Leibniz Institute of Surface Modification (IOM) in Leipzig, I want to thank Frank Frost. Also discussing our results with him was very inspiring.

I want to thank Sven Müller and Moritz Will contributed to this thesis with many measurements on pattern formation with metal co-deposition during their diploma and bachelor thesis, respectively. Sven Müller helped with proofreading of the manuscript.

The RBS measurements were performed by René Feder and Daniel Spemann at the LIPSION lab of the Leipzig University. They extracted the metal area densities from the measured spectra. René Hübner did the TEM measurement at the Helmholtz-Zentrum Dresden Rossendorf. He help with interpreting the TEM images and identified the Pd₃Si crystalites. The SEM images were taken by Dietmar Hirsch at the IOM.

Sven Macko introduced me into the topic during my diploma thesis. I would like to thank him for many fruitful discussions. Some of the data he measured during his dissertation project have been reused in this thesis.

For proofreading the manuscript I would like to thank Charlotte Herbig, Ulrike Schröder, Sven Macko, Sven Müller, Stefan Brackertz, and Stefan Schumacher.

I would like to thank the members of Thomas Michely's workgroup. I enjoyed the time in the group. Special thanks go to Norbert Henn for his help with technical problems.

Without the work of mechanics and electronics workshops this work would not be possible.

I acknowledge the financial support from the DFG through Forschergruppe 845.

Publications

Parts of the results of this thesis have been published in the following articles:

- M. Engler, F. Frost, S. Müller, S. Macko, M. Will, R. Feder, D. Spemann, R. Hübner, S. Facsko, and T. Michely: “Silicide induced ion beam patterning of Si(001)”. *Nanotechnology* **25.11** (2014), 115303. DOI: 10.1088/0957-4484/25/11/115303.
- M. Engler, S. Macko, F. Frost, and T. Michely: “Evolution of ion beam Induced patterns on Si(001)”. *Phys. Rev. B* **89** (2014), 245412. DOI: 10.1103/PhysRevB.89.245412.

During the research project leading to this thesis, I also contributed to the following articles:

- S. Macko, J. Grenzer, F. Frost, M. Engler, D. Hirsch, M. Fritzsche, A. Mücklich, and T. Michely: “Iron-assisted ion beam patterning of Si(001) in the crystalline regime”. *New. J. Phys.* **14.7** (2012), 073003. DOI: 10.1088/1367-2630/14/7/073003.
- S. Macko, F. Frost, M. Engler, D. Hirsch, T. Höche, J. Grenzer, and T. Michely: “Phenomenology of iron-assisted ion beam pattern formation on Si(001)”. *New. J. Phys.* **13.7** (2011), 073017. DOI: 10.1088/1367-2630/13/7/073017.
- E. Vivo, M. Nicoli, M. Engler, T. Michely, L. Vázquez, and R. Cuerno: “Strong anisotropy in surface kinetic roughening: Analysis and experiments”. *Phys. Rev. B* **86** (2012), 245427. DOI: 10.1103/PhysRevB.86.245427.

Erklärung

Ich versichere, dass ich die von mir vorgelegte Dissertation selbständig angefertigt, die benutzten Quellen und Hilfsmittel vollständig angegeben und die Stellen der Arbeit – einschließlich Tabellen, Karten und Abbildungen –, die anderen Werken im Wortlaut oder dem Sinn nach entnommen sind, in jedem Einzelfall als Entlehnung kenntlich gemacht habe; dass diese Dissertation noch keiner anderen Fakultät oder Universität zur Prüfung vorgelegen hat; dass sie – abgesehen von den auf S. 115 angegebenen Teilpublikationen – noch nicht veröffentlicht worden ist sowie, dass ich eine solche Veröffentlichung vor Abschluss des Promotionsverfahrens nicht vornehmen werde. Die Bestimmungen der Promotionsordnung sind mir bekannt. Die von mir vorgelegte Dissertation ist von Prof. Dr. Thomas Michely betreut worden.

Curriculum Vitae

Martin Engler

Geboren 22. 6. 1985 in Bergisch Gladbach

Staatsangehörigkeit deutsch

Werdegang

seit 12/2010 Promotionsstudium, II. Physikalisches Institut, Universität zu Köln, Arbeitsgruppe Michely

12/2010–05/2014 Wissenschaftlicher Mitarbeiter, II. Physikalisches Institut, Universität zu Köln

09/2010–11/2010 Neuseelandaufenthalt

08/2010 Diplom Physik

08/2009–08/2010 Diplomarbeit „Nanostrukturierung von Si(001) mittels Ionenstrahlerosion“, II. Physikalisches Institut, Universität zu Köln, Arbeitsgruppe Michely

08/2009–08/2010 Studentische Hilfskraft, II. Physikalisches Institut, Universität zu Köln

04/2007–10/2008 Studentische Hilfskraft, Zentrum für angewandte Informatik/Regionales Rechenzentrum ZAIK/RRZK, Universität zu Köln

10/2004–08/2010 Studium der Physik an der Universität zu Köln, Nebenfach: Mathematik

06/2004 Abitur, Leistungskurse: Physik und Biologie

08/1995–06/2004 Stadtgymnasium Köln-Porz

08/1993–07/1995 Gemeinschaftsgrundschule Irisweg, Köln

08/1991–07/1993 Grundschule Kupfergasse, Köln